

FORM AND FUNCTIONALITY OF ADDITIVELY MANUFACTURED PARTS WITH
INTERNAL STRUCTURE

A Dissertation
Submitted to the Graduate Faculty
of the
North Dakota State University
of Agriculture and Applied Science

By

AMM Nazmul Ahsan

In Partial Fulfillment of the Requirements
for the Degree of
DOCTOR OF PHILOSOPHY

Major Department:
Industrial and Manufacturing Engineering

June 2019

Fargo, North Dakota

North Dakota State University
Graduate School

Title

FORM AND FUNCTIONALITY OF ADDITIVELY MANUFACTURED
PARTS WITH INTERNAL STRUCTURE

By

AMM Nazmul Ahsan

The Supervisory Committee certifies that this *disquisition* complies with North Dakota
State University's regulations and meets the accepted standards for the degree of

DOCTOR OF PHILOSOPHY

SUPERVISORY COMMITTEE:

Dr. Bashir Khoda

Chair

Dr. Val Marinov

Dr. Chad Ulven

Dr. Zhibin Lin

Approved:

07/03/2019

Date

Dr. David Grewell

Department Chair

ABSTRACT

The tool-less additive manufacturing (AM) or 3D printing processes (3DP) use incremental consolidation of feed-stock materials to construct part. The layer by layer AM processes can achieve spatial material distribution and desired microstructure pattern with high resolution. This unique characteristics of AM can bring custom-made form and tailored functionality within the same object. However, incorporating form and functionality has their own challenge in both design and manufacturing domain. This research focuses on designing manufacturable topology by marrying form and functionality in additively manufactured part using infill structure. To realize the goal, this thesis presents a systematic design framework that focuses on reducing the gap between design and manufacturing of complex architecture. The objective is to develop a design methodology of lattice infill and thin shell structure suitable for additive manufacturing processes. Particularly, custom algorithmic approaches have been developed to adapt the existing porous structural patterns for both interior and exterior of objects considering application specific functionality requirements. The object segmentation and shell perforation methodology proposed in this work ensures manufacturability of large scale thin shell or hollowed objects and incorporates tailored part functionality. Furthermore, a computational design framework developed for tissue scaffold structures incorporates the actual structural heterogeneity of natural bones obtained from their medical images to facilitate the tissue regeneration process. The manufacturability is considered in the design process and the performances are measured after their fabrication. Thus, the present thesis demonstrates how the form of porous structures can be adapted to mingle with functionality requirements of the application as well as fabrication constraints. Also, this work bridges the design framework

(virtual) and the manufacturing platform (realization) through intelligent data management which facilitates smooth transition of information between the two ends.

ACKNOWLEDGEMENTS

I would like to express my sincere gratitude to my advisor Dr. Bashir Khoda for the invaluable guidance, support, and training he provided throughout this research. It's been a privilege for me to work in his lab under his guidance. I appreciate the opportunity he offered me to earn my Ph.D.

I am very grateful to Dr. Val Marinov for providing invaluable insights and instructions, being my committee member, and reviewing this thesis.

I would like to specially thank Dr. Chad Ulven for providing me with the opportunity of research collaboration, valuable insights, and finally being my committee member. I enjoyed working with the members of his research group.

I want to sincerely thank Dr. Zhibin Lin for being my committee member, and providing valuable advice, insights, access to research collaboration, and reviewing this thesis.

I am grateful to the Chair, the Graduate Coordinator, and all the staff of IME Department for their support and assistance throughout my graduate education at NDSU.

I am indebted to my wife for her love, sacrifice, and support. I want to give her special thanks for holding my hand and providing me with encouragement all the time. I truly appreciate her continual patience even though this seemingly endless endeavor kept us far apart.

Finally, I express my deepest gratitude to my mother and father for continual support, love, encouragement, sacrifice, and all the opportunities one can desire for. They have eagerly awaited long the end of my doctoral studies. They gave me the solid foundation of education and showed me how to push beyond the expectations of life. They are the greatest teachers of mine.

DEDICATION

To my parents, Md Abdul Mottaleb and Nazneen Begum

and

wife, Sharmin Majumder

TABLE OF CONTENTS

ABSTRACT.....	iii
ACKNOWLEDGEMENTS.....	v
DEDICATION.....	vi
LIST OF TABLES.....	x
LIST OF FIGURES.....	xii
1. INTRODUCTION.....	1
1.1. Objectives.....	4
1.2. Overview of the Research.....	5
2. LITERATURE REVIEW.....	6
2.1. Porous Infill Structures in Additive Manufacturing.....	6
2.2. Cellular/Lattice Structures.....	8
2.2.1. Closed Cell Lattice.....	9
2.2.2. Open Cell Lattice.....	12
2.3. Thin Wall Hollowed Parts in Additive Manufacturing.....	16
2.4. Porous Infill Structures for Biomedical Applications.....	22
3. NOVEL HONEYCOMB INFILL PATTERN FOR ADDITIVE MANUFACTURING.....	29
3.1. Introduction.....	29
3.2. Definition of Unit Cell for Novel Honeycomb Pattern.....	30
3.3. Infill Space Voxelization.....	38
3.4. Continuous Honeycomb Toolpath Scheme.....	40
3.5. Sample Parts Fabrication.....	40
3.6. Mechanical Tests.....	43
3.7. Results and Discussion.....	44
3.8. Conclusion.....	53

4. SHELL-INFILL CONTACT INTERFACE DESIGN WITH VARIATIONAL HONEYCOMB PATTERN	55
4.1. Introduction	55
4.2. Gradient Honeycomb Lattice Infill	56
4.2.1. Object Feature Identification for Adaptive Infill.....	56
4.2.2. Continuous Honeycomb Toolpath.....	58
4.2.3. Intra-Layer Density Variation and Continuous Heterogeneous Infill Generation	59
4.2.4. Maximization of Skin-Infill Contact Points	61
4.3. Results and Discussion.....	62
4.3.1. Adaptive Density Honeycomb Infill	62
4.3.2. Boundary Contact Points Increase through Intra-Layer Density Variation	64
4.4. Conclusion.....	66
5. HETEROGENEOUS TOPOLOGY DESIGN FOR ENGINEERED TISSUE SCAFFOLDS	68
5.1. Introduction	68
5.2. Methodology	69
5.2.1. Pre-processing stage	69
5.2.2. Medical Image Data Digitization	71
5.2.3. Topology Reconstruction with Parametric Function.....	72
5.2.4. Material Mapping with Generated Functions.....	75
5.3. Processing/Bio-printing.....	78
5.4. Implementation.....	79
5.5. Conclusion.....	87
6. 3D PRINTABLE GRAIN BASED MODEL SEGMENTATION	88
6.1. Introduction	88

6.2. Methodology	91
6.2.1. Surface Property Extraction	91
6.2.2. Point Clustering and Homogeneous Grain Generation	92
6.2.3. Grain Boundary Smoothing.....	97
6.2.4. Process Plan for Grain Printing	99
6.2.5. Shape Conforming Honeycomb Lattice Wall Generation.....	102
6.3. Implementation.....	103
6.4. Conclusion.....	111
7. CONCLUSION AND FUTURE WORK	113
7.1. Conclusion.....	113
7.2. Novelty and Contributions	114
7.3. Future Works.....	115
REFERENCES	117

LIST OF TABLES

<u>Table</u>	<u>Page</u>
1. Different types of honeycomb unit cells [48].	10
2. Different types of open cells.	12
3. Existing object segmentation techniques for 3D printing.	20
4. Plateau stress, plateau strain, and elastic modulus PLA honeycomb lattices.	48
5. Plateau stress, plateau strain, and elastic modulus of TPU honeycomb lattices.....	52
6. Densification strains and total specific energies absorbed at densification of PLA honeycombs.	52
7. Densification strains and energies absorbed per unit volume at densification of TPU honeycombs.....	52
8. Comparison among the proposed variational and existing uniform honeycomb infills	64
9. Percentage increase in the number of boundary contact points for different voxelization orientation of the square block.....	65
10. Percentage increase in the number of boundary contact points for different voxelization orientation of the bison model layer given in Figure 30.	65
11. Comparison between the proposed method and the uniform porosity design.	82
12. Parameter comparison between the fabricated and the designed pore.	84
13. Grain wise optimal build orientation for vase model.....	104
14. Grain wise optimal build orientation for Bison model.	106
15. Comparison between segmented and full models of flower vase and Bison (scaled down version) with respect to total build time and support volume on different commercial machines.....	106
16. Comparison between segmented and full models of flower vase and Bison (actual scale) with respect to total build time and support volume in different commercial machines.	107
17. Grain wise optimal build orientation for Helmet model.....	109
18. Grain wise optimal build orientation for Helmet model.....	110

19.	Comparison between segmented and full models of helmet and hand cast with respect to total build time (BT) and support volume (SV) on different commercial machines.	111
-----	---	-----

LIST OF FIGURES

<u>Figure</u>	<u>Page</u>
1. Classification of additively manufactured parts.	2
2. (a) Part skin and infill. (b) Different type of existing porous infill structures and (c) infill structures with different relative density [30].	7
3. Classification of cellular/lattice structures.	9
4. (a) Hexagonal and (b) square cell honeycomb structures [47].	10
5. Expansion manufacturing process for metallic hexagonal honeycomb structures [47].	11
6. Corrugation-manufacturing process for metallic hexagonal honeycomb structures [47].	12
7. (a) Perforated metal sheet folding process for pyramidal lattice structure fabrication, (b) multilayer assembly, (c) a multilayer pyramidal lattice sandwich cut into cylindrical shape [77].	13
8. Titanium matrix composite (TMC) collinear filament lattice fabrication with wire lay-up process: (a) assembly (lay down) sequence for collinear filaments, (b) vacuum diffusion bonding of the filament layers, (c) Assembling face sheets to make sandwich panel, and (d) brazing of face sheets to the cores [70].	14
9. (a-b) Rhombic dodecahedron lattices fabricated with electron beam melting AM process [74] and (c-d) Gyroid lattices fabricated with selective laser melting AM process [75].	15
10. Part inconsistencies and defects in powder-based laser AM process [82].	16
11. Support entrapment into thin-wall/shell object.	17
12. Model segmentation without considering geometry.	19
13. (a) Top view, (b) three layers stack, and (c) unit cell configuration with formation sequence 2-1-1, 1-2-1, and 1-1-2 of the traditional honeycomb infill tool-path.	31
14. Proposed honeycomb unit cell using 1/6 division design parameter for continuous toolpath: (a) voxel definition, (b) hexagonal honeycomb cell definition, (c) 2D unit cell representation, (d) sublayer toolpath segments constituting a unit cell, and (e) the resulting 3D unit cell with 1-0-1, 1-1-0, and 0-1-1 formation sequence.	33

15.	Traditional honeycomb unit cell: (a) voxel definition, (b) hexagonal honeycomb cell definition, (c) 2D unit cell representation, (d) sublayer toolpath segments constituting a unit cell, and (e) the resulting 3D unit cell.	35
16.	(a) Proposed and traditional unit cells with different size and density and (b) Relationship between unit cell size parameters and relative density for proposed and traditional honeycomb cells with 1/6 design parameter.	36
17.	Proposed honeycomb unit cell designed using 1/8 division design parameter for a square voxel: (a) voxel definition, (b) hexagonal honeycomb cell definition, (c) 2D unit cell representation, (d) sublayer toolpath segments constituting a unit cell, and (e) the resulting 3D unit cell.	37
18.	Relationship between Cell packing and relative density for three types of honeycomb cells.	38
19.	Infill layer discretization into representative voxel units of different sizes (<u>$L_x = L_y$</u> , <u>$L_x > L_y$</u> , and <u>$L_x < L_y$</u>) and honeycomb cell fitting.	39
20.	Honeycomb lattice form layer by layer continuous toolpath.	40
21.	Function based variational density distribution of a layer (80x80mm): (a) spatial distribution of longitudinal and transverse densities, (b) color map representing resultant density gradient in the layer, (c) non-uniform voxelization, and (d) resulting variational honeycomb cell fitting and toolpath generation.	42
22.	Proposed and traditional honeycomb toolpaths with equivalent mean relative density (23%; 40x40 mm layers).	42
23.	Fabricated samples: (a) traditional PLA honeycomb, (b) proposed variational PLA honeycomb, (c) proposed uniform PLA honeycomb, (d) traditional TPU honeycomb, and (e) proposed variational TPU honeycomb.	43
24.	Compression behavior of the proposed and traditional PLA honeycombs along X-direction.	45
25.	Compression behavior of the proposed and traditional PLA honeycombs along Y-direction.	46
26.	Lattice stress vs lattice strain curves of (a) PLA and (b) TPU honeycombs.	48
27.	Compression behavior of the proposed and traditional TPU honeycombs along X-direction.	50
28.	Specific energies absorbed by (a) PLA and (b) TPU honeycombs.	51

29.	Variational voxelization and continuous honeycomb toolpath generated from the given density map for a layer of bison model (printed model=24 layers).....	53
30.	(a) Surface model, (b) points sampled on object surface layer boundaries and surface normal vectors, and (c) infill support required region (red).....	57
31.	Layer by layer gradient infill density distribution along the build direction based on surface normal angles.	58
32.	Function based variational density distribution of a layer: (a) spatial distribution of longitudinal and transverse variational densities, (b) non-uniform voxelization, (c) variational honeycomb cell fitting, (d) spatial distribution of longitudinal and transverse uniform densities, (e) uniform voxelization, and (f) uniform honeycomb cell fitting.	60
33.	Changing boundary contact points through rotating the boundary contour for variational voxelization.....	62
34.	(a) Proposed adaptive density variational honeycomb infill, (b) parts of the overhanging skin printed on the proposed infill, (c) uniform honeycomb infill with low density, (d) parts of the overhanging skin printed on the uniform honeycomb infill with low density, (e) uniform honeycomb infill with high density, and (d) parts of the overhanging skin printed on the uniform honeycomb infill with high density.	63
35.	Proposed direct bio-printing process roadmap	69
36.	(a) Proximal femur (midcoronal plane) CT image and (b) bone volume fraction (BV/TV) [171]	70
37.	(a) High resolution peripheral QCT (HR-pQCT) image of human distal tibia [172] and (b) corresponding quantized image I'	72
38.	Normalized average pixel value as a function of pixel location along (a) longitudinal direction and (b) transverse direction and corresponding segmented Bézier curve fitting.	72
39.	Parametric curve fitting algorithm (Algorithm 1).....	75
40.	Unit cell representation: (a) a segment of a bi-layer and (b) a unit cell.....	76
41.	Variational tool-path generation algorithm (Algorithm 2).	77
42.	(a) Hierarchical data structure and (b) tool movement data storage file format (bio-Motion) for direct bio-printing.....	78
43.	Micro-nozzle bio-additive material deposition system.....	79

44.	(a) First and (c) fourth images among the stack of four CT images of human vertebra and (b, d) corresponding quantized images, respectively, at $l = 8$	80
45.	Two corresponding orthogonal parametric topology functions generated from first (a-d) and fourth (e-h) vertebra images (The image and functions are represented in the same scale).	80
46.	(a) Proposed variational porosity toolpath, (b) corresponding variational porosity distribution map, (c) uniform porosity toolpath, and (d) corresponding uniform porosity map for the first vertebra slice.	82
47.	Heterogeneous porosity design from the proposed methodology for the first vertebra slice (a) generated zigzag toolpath, (b) bio-printed with hybrid hydrogel (alginate + cellulose) two layers, and (c) bio-printed 10 layers, (d) enlarged view of a section showing the variational porosity in scaffold topology.	83
48.	(a) CT image of human distal femur and (b) corresponding quantized image at $l = 16$	84
49.	Two corresponding orthogonal parametric topology functions generated from femur CT image (The images and functions are represented in the same scale).....	85
50.	Heterogeneous porosity design from the proposed methodology for femur slice: (a) Zigzag toolpath for femur slice, (b) corresponding variational porosity distribution map, and (c) printed femur slice with ABS material.	85
51.	Heterogeneous porosity design and bio-printing for femur slice: (a) generated toolpath and (b) two layers bio-printed with hybrid hydrogel (alginate + cellulose).	86
52.	Framework of the proposed methodology.	91
53.	Facet characteristics and relation between seed and non-seed facets. The facets in yellow color are the initial random seeds.	93
54.	(a) Initial random seeds and (b) generated grains from the initial seeds.	95
55.	Seed update procedure: (a) kth grain with its centroid g_k , (b) angle determination between the facet normal and imaginary vector connecting the facet centroid to grain centroid, and (c) updated seed.	96
56.	Facet clustering and object grain formation: (a) object mesh surface, (b) initial random seeds, (c) grain formation using the initial seeds, (d) seed updating, (e) grain formation using updated seeds, (f) final grains.	97
57.	Grain Boundary smoothing process: (a) Grains with jagged boundary curve, (b) smoothing a jagged boundary curve, and (c) grains with smoothed boundary.....	98

58.	Build orientation for segmented object grains: (a) segmented object and (b) exploded view in the global coordinate system, (c) reorientation of a grain at optimal angles, and (d) all grains optimally oriented and placed on the build plate.	99
59.	Support needed facets and support generation.....	100
60.	(a) Boundary contour projection of an optimally oriented grain, (b) Hexagonal honeycomb cell tessellation, (c) mapping back honeycomb cells and offsets and constructing 3D cell contours on grain surface, and (d) resulting hollowed shape conforming honeycomb lattice grain.	103
61.	(a) Flower vase model, (b) Segmentation following proposed methodology, (c) Optimally oriented grain with slicing along build direction.....	104
62.	(a-b) Fabricated grains and assembling them together, and (c) final flower vase after assembly.	105
63.	(a) Bison model, (b) Segmentation following proposed methodology, (c) Optimally oriented grain with slicing along build direction.	106
64.	Build time and support volume comparison between full and segmented models on Dimension 1200es (Dim), Replicator 2 (Rep), and Ultimaker3 (Ult).	107
65.	(a) Mesh surface with color map of helmet, (b) segmentation following proposed methodology, (c) two optimally oriented grains with varying honeycomb cutouts.	108
66.	(a) Fabricated grains, (b) Assembling grains together, and (c–d) Final thin lattice wall helmet object after assembly.....	109
67.	(a) Mesh surface with color map of hand cast, (b) segmentation following proposed methodology, (c) two optimally oriented grains with honeycomb cutouts.	110
68.	(a) Fabricated grains with some assembled, (b) assembling grains together, and (c) final thin lattice wall hand cast in use for demonstration.....	110

1. INTRODUCTION

Additive Manufacturing (AM) process, which is also commonly known as 3D printing, converts a digital model into a 3D physical object by printing and stacking layers one upon another. The digital model is generated either by a CAD modeler or through a reverse engineering technique. The layers geometries are obtained by slicing the digital model and material is printed inside these layers and stacked along the build direction. Thus, the current layer provides support plane to the succeeding layers during fabrication. Depending upon the object geometry, type of AM process, and the process plan, the object may require additional sacrificial support material to fabricate the overhangs.

Depending upon the form of the objects, additively manufactured parts can be broadly categorized into three groups: (i) primitive based solid objects, (ii) non-primitive topology optimized porous or freeform objects, and (iii) thin wall/shell hollowed object (see Figure 1 for further illustration). Primitive based solid objects are composed of basic primitives such as cube, sphere, cylinder etc. in solid form. However, to incorporate functionality into the part, the internal region of a part can be modified to porous architecture resulting in an object having porous infill with or without shell. Based on the application such as mechanical, thermal, phononic, biological, and aesthetics, the part functionality may refer to light weighting [1], ventilation/air pass [2], nutrient and gas transport in tissue engineered scaffolds [3], tissue ingrowth and integration in implants [4, 5], impact or energy absorption [6], part quality enhancement [1], heat transfer [7], sound transfer [8], manufacturability and uncured material removal [2], decoration/aesthetics and so on.

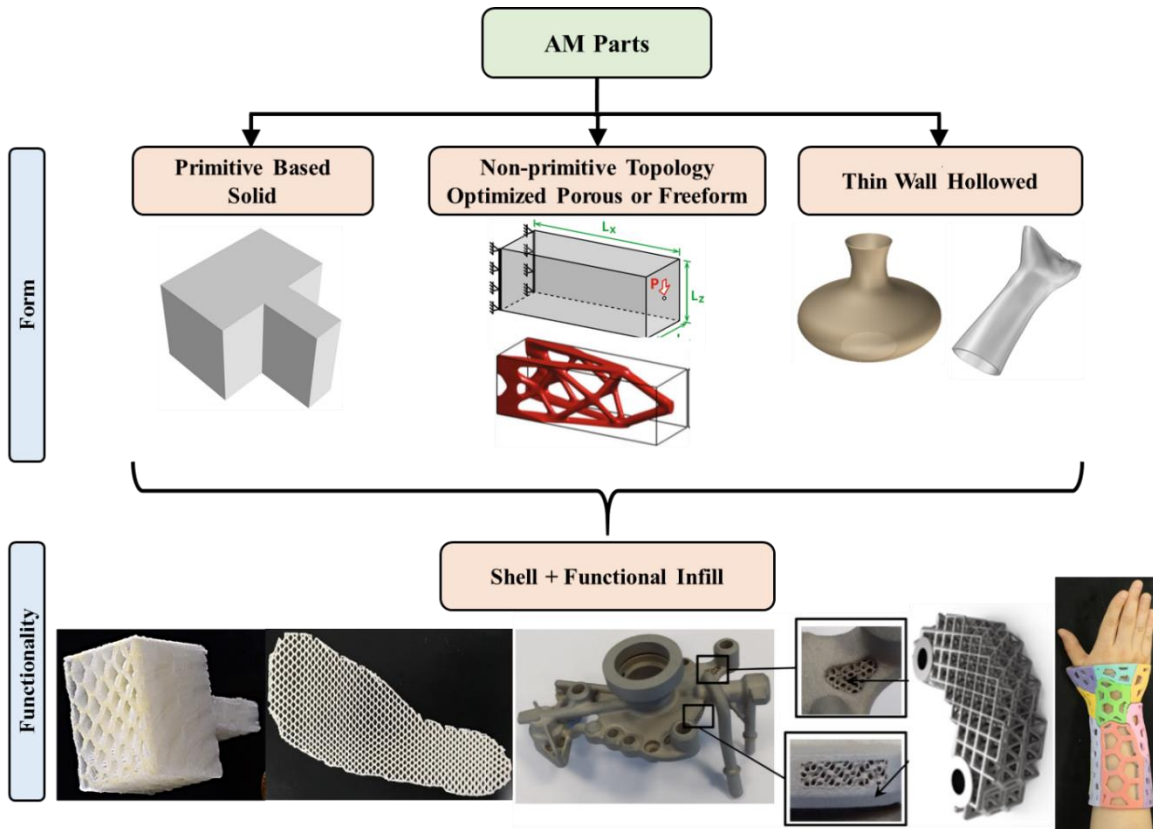


Figure 1. Classification of additively manufactured parts.

The topology optimized objects are not composed of the basic primitives, rather they are porous at macro level and freeform shaped. The macro level porous and freeform geometry may be derived from the design considerations and application requirements such as mechanical stiffness/compliance. Thin wall hollowed objects are usually composed of solid shell and hollowed functional space, for instance flower vase, hand cast, helmet etc. However, the solid shell itself can be designed as porous at macro level (shell perforated with cutout patterns) or at micro level (shell infill) to enhance functionality such as ventilation and/or easy removal of uncured material [2], decoration/aesthetics [9] etc.

Recent advancements in physical and biological fields demand new multifunctional materials and structures possessing light weight, superior performance, and versatility. Porous

cellular or lattice structures have been receiving considerable attention as an alternative solution/culture of lightweight design and new materiality. Cellular structures can be designed to have mechanical, thermal, phononic, and biological functionalities, for instance, structural materials [10], energy absorbing foams [11, 12], heat exchangers [13], phononic band gap structures [14], and bone and other tissue scaffolds and implants [15-17]. The exceptional properties of cellular materials such as low relative density, high specific strength, large area moment of inertia, and relatively high thermal conductivity enables them a suitable candidate for these applications [18]. Moreover, heterogeneous cellular structures are developed to selectively enhance localized properties in custom designs. These structures have varying material distribution based on the application thereby making it functionally graded.

Because of their unique capabilities including light weight, higher specific strength, and increased surface area, porous cellular structures are widely used in orthopedic biomedical applications such as prostheses and implants [19-21]. The porous internal structure of prostheses and implants facilitates tissue ingrowth, liquid and mass transfer, and better implant fixation [22]. Furthermore, for patient specific customized prostheses and implants, the porous internal architecture can be tailored to meet the application requirements for better functionality.

Thus, structural properties of porous cellular materials can be tailored enhance desired performance. However, modelling functional porous structures in the traditional CAD environment is difficult and often time inaccurate. Besides, the *de facto* STL conversion of bio-models introduces loss of information and piles up more errors in each subsequent step (build orientation, slicing, tool-path planning) of AM process. Furthermore, the geometry and internal architecture of porous structures are also restricted by the manufacturing process. In particular, traditional manufacturing processes experience difficulties in fabricating uniform as well as

functionally graded heterogeneous cellular/lattice structures. Additive manufacturing (AM) however has the potential but demonstrated significant disparity between the designed and manufactured cellular structures thus far. Because of the inherent complexity in the geometry of cellular structures, the generated layers contain multiple discrete and complex contours, e.g., internal hollow features and concave sections. This may cause significant interruption in machine movement increasing non-value added activities. Therefore, the inherent limits of the existing AM technologies put restriction on the modeling of both uniform and heterogeneous cellular structures.

1.1. Objectives

The goal of this thesis is to design manufacturable topology by marrying form and functionality in additively manufactured part using infill structure. To realize the goal, this thesis presents a systematic design framework that focuses on reducing the gap between design and manufacturing of complex architecture. The objective is to develop a design methodology of lattice infill and thin shell structure suitable for additive manufacturing processes. The manufacturability is considered in the design process and the performances are measured after their fabrication. The specific tasks performed in this research are as follows:

1. Design and manufacture of continuous toolpath for uniform and variational honeycomb lattice suitable for infill applications.
2. Design and optimize variational honeycomb lattice infill topology to enhance skin-infill contact.
3. Design for porous scaffold structure topology for biomedical applications.
4. Design a grain based object segmentation technique and develop a functionality based shell perforation approach for thin wall/shell objects.

5. Seamlessly integrate topology design with additive manufacturing using the information generated in topology design phase.

1.2. Overview of the Research

This thesis is organized as follows: Section 2 presents the background and review of literature on the porous infill structures as well as skin/shell in AM parts with respect to their form and functionality. Section 3 illustrates the proposed approach to designing and manufacturing uniform and variational honeycomb lattice with continuous toolpath for AM part infills. Section 4 further proposes an adaptive density honeycomb lattice infill topology design approach to enhance skin-infill contact interface for improved part surface quality. A functionality based porous tissue scaffold infill design approach facilitating tissue regeneration is proposed and presented in Section 5.

The focus of Section 6 is twofold: (a) developing a grain based object segmentation technique to partition the shell of hollowed objects requiring substantially increased resources in terms of large scale machine and build time and (b) introducing shell perforation approach thin-shell hollowed objects to enhance part functionality and avoid material entrapment. Finally, Section 7 concludes this thesis and presents some future directions of this research.

2. LITERATURE REVIEW

2.1. Porous Infill Structures in Additive Manufacturing

In additive manufacturing processes, infills are considered as the interior of a part surrounded by its skin/shell as shown in Figure 2(a). The primary function of infill is to provide structural integrity to the part from collapsing inside and to work as a print platform for the skin hanging over the interior of the part. Hollowing object can impair the structural integrity of the object. Therefore infills sometimes become inevitable in AM processes. However, infills increase the usage of material and eventually the part weight. Hence, porous/lattice infill structures are frequently employed to minimize part weight as well as to preserve reasonable amount of structural integrity of the part. Some examples of existing porous infills with different relative densities are demonstrated in Figure 2(b-c). The most common infill patterns available to slicing and 3D printing software is 0° - 90° zigzag (grid/recti) and honeycomb which are uniform in density. As far as porous structures are concerned, deposition patterns play a significant role for build time, structural performance, etc. Thus, deposition patterns are optimized for individual parts. For instance, the angular (0° - 90°) pattern has been optimized with other angle combinations based on object geometries [23-25].

Domínguez-Rodríguez et al. [26] studied the effect of printing orientation and relative density on compressive properties including stiffness of the 3D printed samples with honeycomb and rectangular infill patterns. They found honeycomb infill patterns to be stiffer and stronger compared to rectangular infill. However, the honeycomb infill took almost twice the printing time of rectangular infill. Bartolai et al. [27] also demonstrated that the honeycomb infill outperformed the rectilinear infill in terms of strength, but increased number of toolpath direction change and tool air travel resulted in longer build time. Additionally, Ramkumar [28]

demonstrated that honeycomb infill pattern led to increased impact strength compared to rectilinear infill pattern. Using response surface method, Moradi et al. [29] found that the infill relative density is one of the major parameters influencing the mechanical performance of the structure. With the experimental results, it was claimed that honeycomb was adequate as the infill structure for light weight parts. Thus the authors ruled out solid parts as their optimized honeycomb part possessed superior characteristics in terms of mechanical properties, weight, and build time.

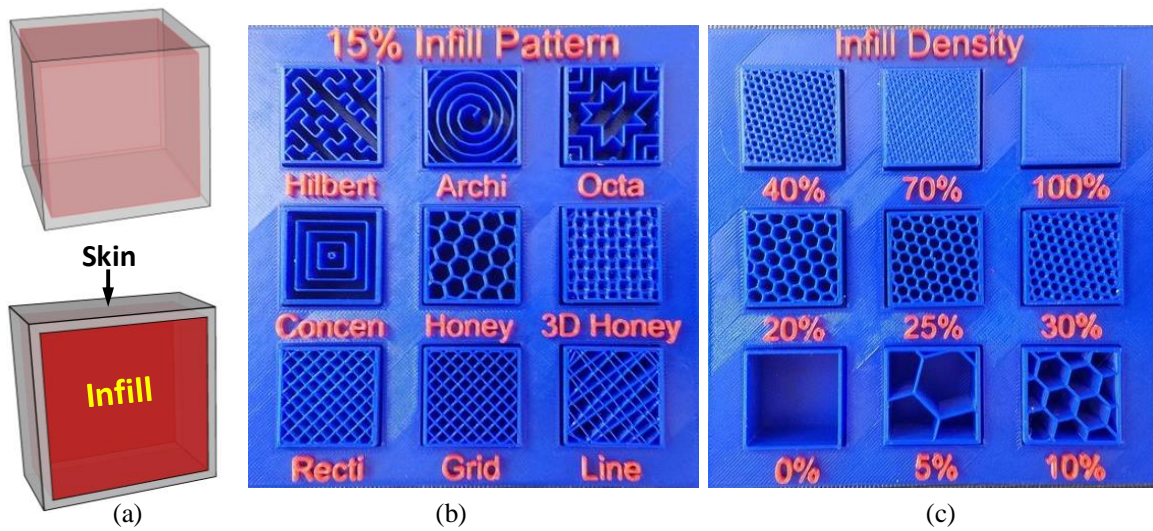


Figure 2. (a) Part skin and infill. (b) Different type of existing porous infill structures and (c) infill structures with different relative density [30].

Iovenitti et al. [31] 3D-printed polymeric uniform honeycomb structures with different cell wall thicknesses and studied their in-plane compressive behavior and energy absorbing capability. The printing toolpath was obtained using a commercially available slicing software and no variational density was incorporated in the structures. Conversely, Bates et al. [32] printed flexible polymer honeycomb structures with graded density in one direction to study energy absorbing characteristics. The graded density was incorporated through varying wall thickness of the honeycomb cells. However, such thicker cell walls requiring multiple pass of

material deposition along cell walls introduces discrete toolpath segments with increased amount of interruptions and chances of fabrication defects. The variation in wall thickness between cells further increases deposition discontinuity which in turn can lead to increased build time. A Voronoi based irregular honeycomb-like porous infill proposed by Lu et al. [33] considered part strength-to-weight optimization taking into account the stress working across the part interior. This structure incorporated varying cell size as well as varying cell wall thickness, which again introduced discrete toolpath segments with increased amount of interruptions resulting thin features, and fabrication defects. Similarly, the self-supporting rhombic cell lattice infill structures developed by Wu et al. [34] is the macro scale segmentation of the infill volume. Although minimum printable wall thickness was taken into design consideration, their manufacturability could be a challenge.

Recently, Vogiatzis et al. [35] demonstrated conformal mapping method to generate 3D periodic lattice mesh for free-form surfaces of part skin. Since the lattice mesh conforms to the object surface, it introduces varying density and distortion of unit cell caused by the object shape and surface curvature. Some non-conventional infill patterns such as skin-frame structures [36, 37] have been proposed for AM processes. Most of the time, the lattice or frame structures results in tiny layer contour geometries and increased tool start-stops and air travel, which eventually lead to fabrication complexity.

2.2. Cellular/Lattice Structures

Porous cellular or lattice materials possess some exceptional characteristics for instance, light weight, low density, high gas permeability, and large specific surface area making them attractive structural and functional materials for both physical and biomedical applications [38]. These materials are formed by assembling the building blocks called unit cells. The unit cells are

constituted with solid edges/struts or faces. Such porous materials are widely found in nature such as sponge, wood and coral, etc. [39]. Man-made cellular or lattice materials are also widely utilized in many applications including high stiffness structures [40], thermal insulation [41], energy absorption [42], and biomedical structures [43].

Porous structures can have open cells, or closed cells, or a combination of both. Closed cells are surrounded by cell walls and thus disconnected from other cells, whereas open cells are connected to the surrounding cells and thus permeable [44]. Again, cellular/lattice structures can be uniform or nonuniform (heterogeneous) depending on the arrangement of the unit cells. In uniform periodic cellular materials, the identical/uniform cells are repeated in a periodic manner [45]. The heterogeneous and functionally graded cellular materials consist of heterogeneous cells arranged in a predefined manner to meet the required performance [46]. The detailed classification of the cellular structures are given in Figure 3.

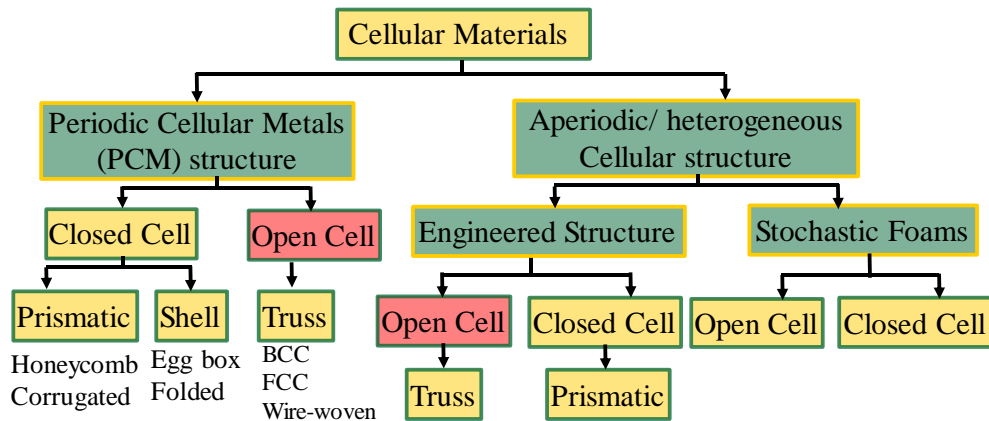


Figure 3. Classification of cellular/lattice structures.

2.2.1. Closed Cell Lattice

Honeycomb structures are the most common closed cell porous structures used as the core of sandwich, floating, packaging etc. materials. Honeycombs structures can have different types of unit cell geometry. For example, Figure 4 demonstrates hexagonal and square cell

honeycomb core of sandwich structures. Table 1 lists some honeycomb unit cells with their cross-sectional geometries.

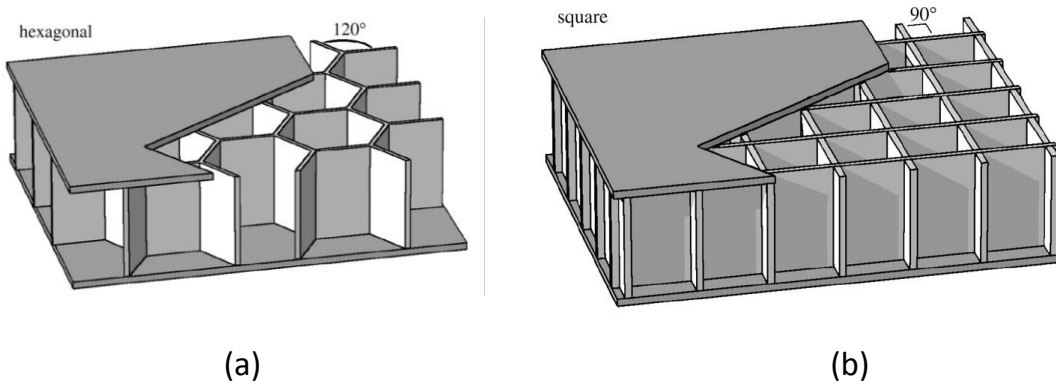
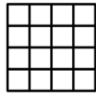

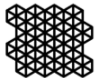
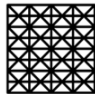
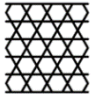
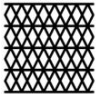
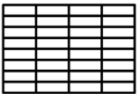









Figure 4. (a) Hexagonal and (b) square cell honeycomb structures [47].

Table 1. Different types of honeycomb unit cells [48].

							
Unit Cell							
Cell Type	Square	Hexagonal	triangular	Square supercell with mix of squares and triangles	Kagome	Diamond	Rectangular

Metallic hexagonal honeycomb structures can be fabricated by expansion manufacturing process or corrugation-manufacturing process [49]. In expansion manufacturing process, thin metal sheets are cut into panels which are then bent according to the cell geometry. The bent panels are stacked and bonded by laser or adhesive along the stripes resulting in HOBE block as shown in Figure 5. The HOBE block is stretched to form the honeycomb structure. This process is suitable for low relative density structures (thinner sheets) since the force required to stretch thicker sheet may exceed the bond strength. In corrugation-manufacturing process, metal sheets

are first corrugated. Then corrugated sheets are cut, stacked, and welded adhesively bonded as shown in Figure 6. Since no stretching force is involved after bonding, higher relative density structures (thicker sheet) can be fabricated by this process.

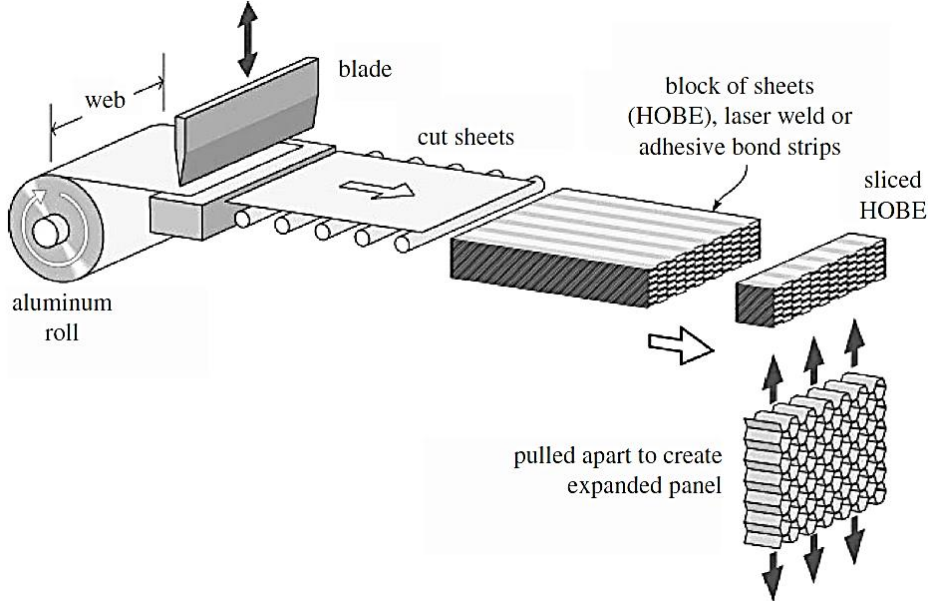


Figure 5. Expansion manufacturing process for metallic hexagonal honeycomb structures [47].

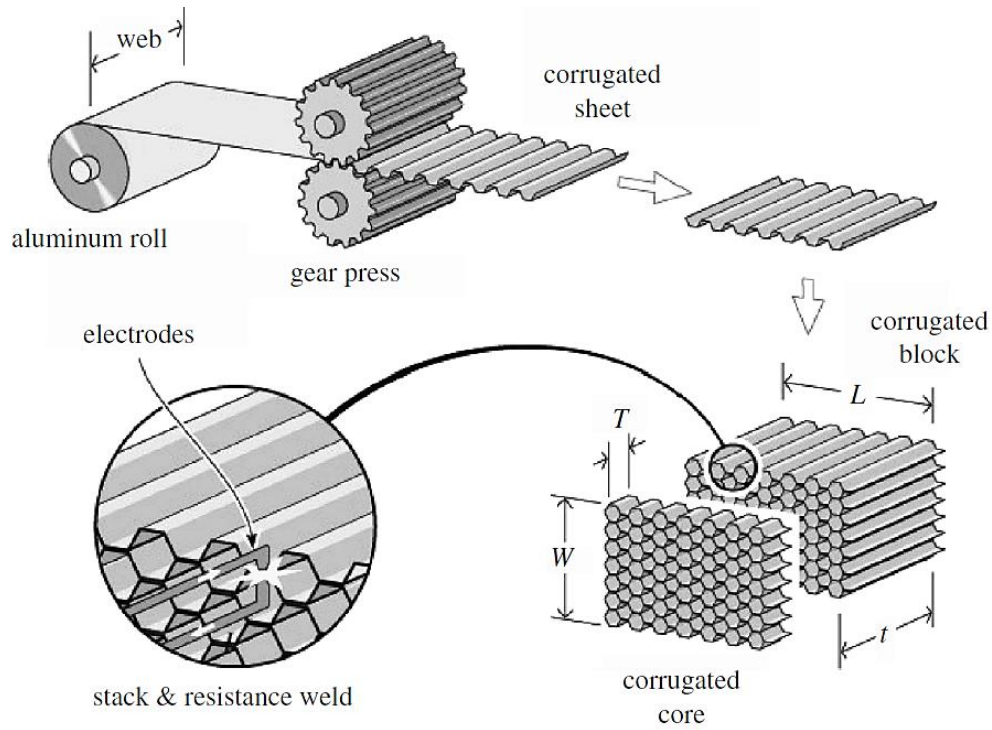


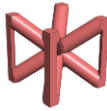

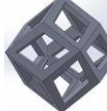




Figure 6. Corrugation-manufacturing process for metallic hexagonal honeycomb structures [47].

2.2.2. Open Cell Lattice

Open cell lattice structures can also have different types of unit cell geometry. For example, octet-truss, BCC, BCC-Z, cubic, rhombic dodecahedron pyramidal etc. are some common open type unit cells which are listed in Table 2.

Table 2. Different types of open cells.

Unit Cell							
Cell Type	Octet-truss	BCC	BCC-Z	Cubic	Rhombic dodecahedron	Pyramidal	Gyroid
Ref.	[50-52]	[53-55]	[53, 55]	[56-58]	[58]	[59]	[60, 61]

Metallic open cell lattice structures can be fabricated by investment casting [62-65], perforated or expanded metal sheet folding [66-69], metallic wire weaving and braiding [70-72], or metal additive manufacturing [73-76] processes. In investment casting process, wax or polymer lattice structure is used as pattern. For complex structures with small diameter struts (low relative density), casting porosity or other defects may affect the structural integrity of the structure. Hence, this process is also limited to high fluidity casting alloys. In perforated or expanded metal sheet folding process, sheets are perforated by cutting patterns into the sheets with die stamping, laser, water jet cutting methods etc., or expanded by slitting with perforating scissors. Then the perforated sheets are folded into desired shape with die-punch to form the lattice core as shown in Figure 7(a). To make multilayer lattice core, the folded layers are stacked and joined with Transient Liquid Phase (TLP) bonding process (see Figure 7(b-c)).

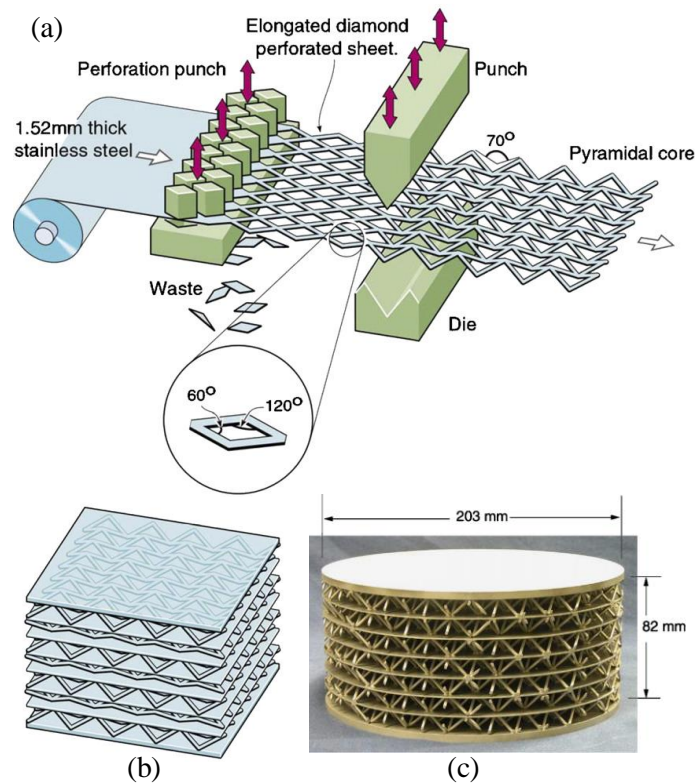


Figure 7. (a) Perforated metal sheet folding process for pyramidal lattice structure fabrication, (b) multilayer assembly, (c) a multilayer pyramidal lattice sandwich cut into cylindrical shape [77].

In metallic wire weaving and braiding process, lattice structures are fabricated from metal woven fabrics/textiles by stacking and bonding fabric layers. The unit cell shape is determined by the weaving pattern of the wire fabrics. Instead of using woven fabrics, wire lay-up process can be used, where collinear wires are laid down layer by layer using slotted tool to control wire spacing and orientation as shown in Figure 8(a). Diffusion or Transient Liquid Phase (TLP) bonding process is used to join the nodes of adjacent layers in these structures (see Figure 8(b)).

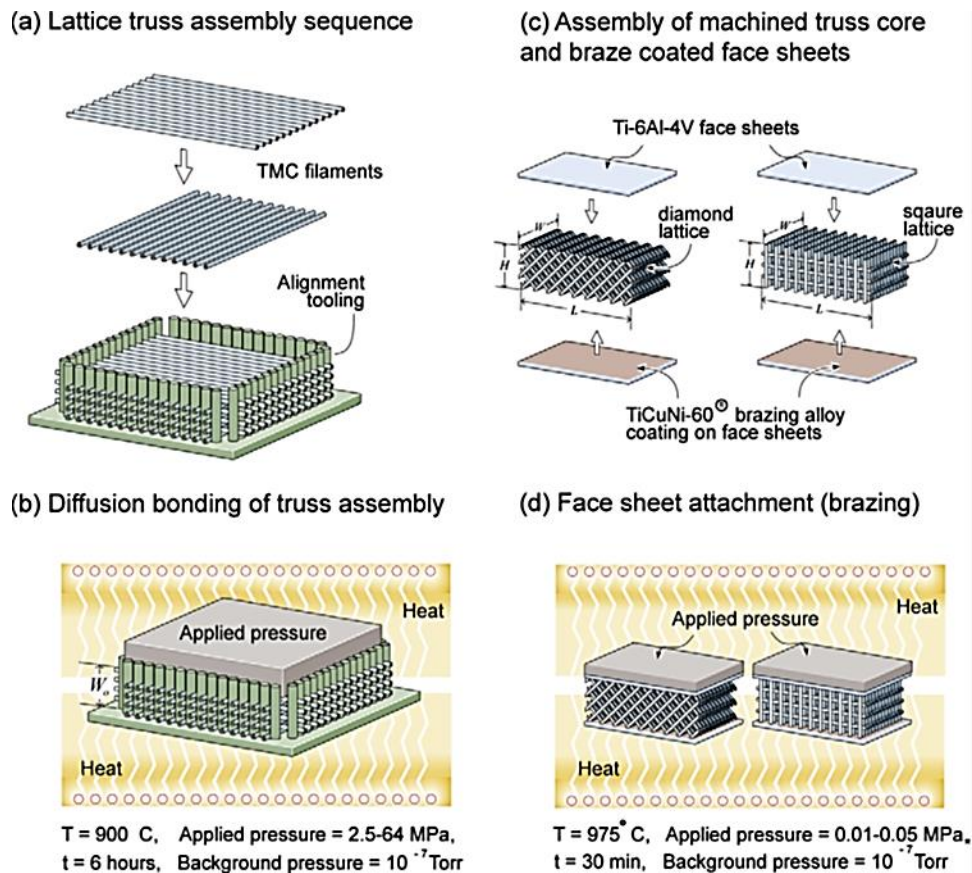


Figure 8. Titanium matrix composite (TMC) collinear filament lattice fabrication with wire lay-up process: (a) assembly (lay down) sequence for collinear filaments, (b) vacuum diffusion bonding of the filament layers, (c) Assembling face sheets to make sandwich panel, and (d) brazing of face sheets to the cores [70].

Transient liquid phase (TLP) [78, 79] bonding, also known as diffusion brazing is an attractive flux-less, high strength joining technique for its relatively low pressure requirement

and can join a range of base metals (i.e. Al alloys, carbon steels, stainless steels, Ni alloys, and Ti alloys). An interlayer alloy is generally applied as coating between the flat and closely packed joining surfaces in the form of thin foil, powders, paste, electroplate, sputter etc. The material from interlayer alloy diffuses into the base metal and seal the bond through isothermal solidification which happens below the solidus temperature of the base metal.

Even though, the porous structures are widely used in many applications, the traditional fabrication processes have restrictions and suffers from repeatability issue [38]. Metal additive manufacturing processes such as electron beam melting (EBM) [73, 74] or selective laser melting (SLM) [75, 76] can produce lattice structures, as shown in Figure 9, through selectively melting metal powders layer by layer with electron or laser beam, respectively. AM techniques offer exceptional capabilities of producing complex lattice structures. However, there are over 50 different process parameters and variables in powder-based AM processes that determine the part consistency and quality [80, 81]. Some examples of uncertainty in part properties and defects resulting from a powder-based laser AM process are demonstrated in Figure 10. Such inconsistency and variation in the fabrication process often limits the application of AM techniques to rapid prototyping ventures [82].

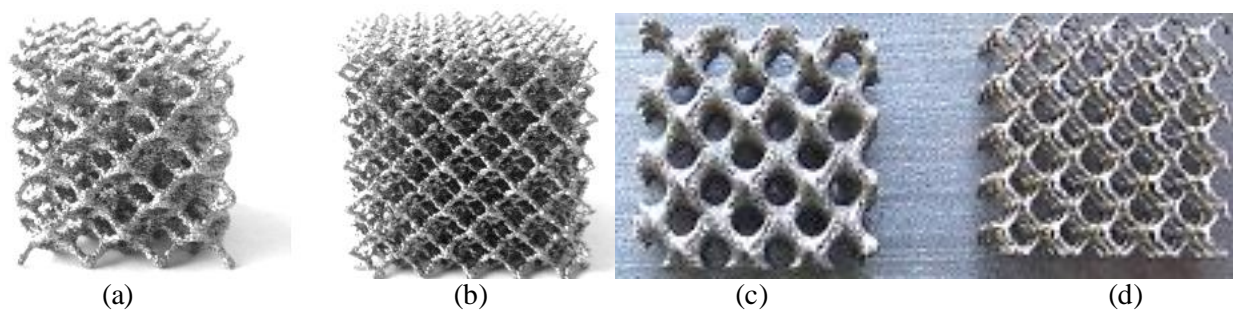


Figure 9. (a-b) Rhombic dodecahedron lattices fabricated with electron beam melting AM process [74] and (c-d) Gyroid lattices fabricated with selective laser melting AM process [75].

For parts having porous infill, a skin can be wrapped around the infill generating a skin-infill object. On the other hand, hollowed object with thin shell does not require infill in the functional cavity inside the part. The following section reviews the hollowed parts in additive manufacturing.

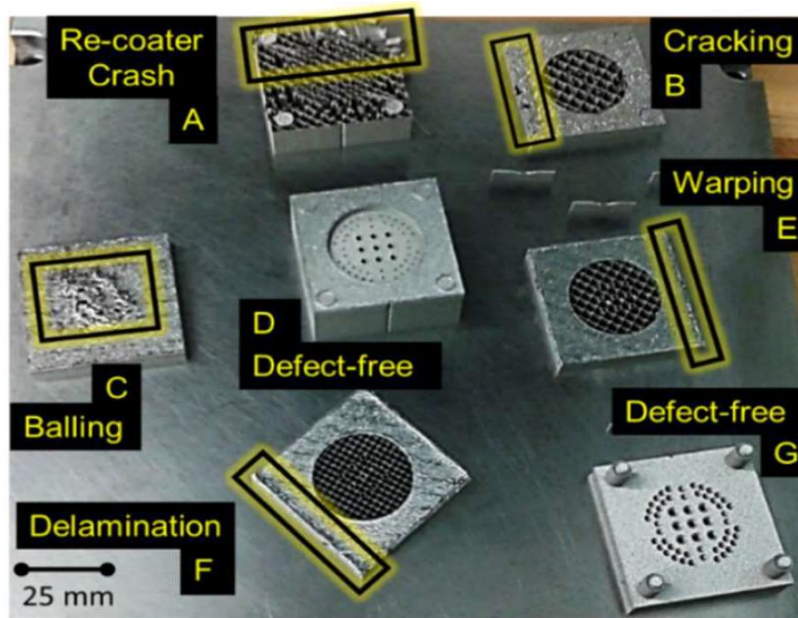


Figure 10. Part inconsistencies and defects in powder-based laser AM process [82].

2.3. Thin Wall Hollowed Parts in Additive Manufacturing

Although new product/prototype development cycle time has reduced significantly with the help of AM technology, however it consumes a significant amount of time to fabricate individual parts [23] due to low speed and material delivery rate. As a result, the viability of AM processes is limited towards mass customized low quantity small size [83] product. To speed up the additive manufacturing processes, researchers are proposing novel structure design methods and techniques lately. One common approach is to reduce the deposition volume by hollowing the object and creating a scaled-down version in its inside [84]. A skin-frame structure design [37] is another way of reducing material wastage with enhanced structural stability where frame

structure is placed underneath the skin. Similarly, it is also found that the interior was filled with porous voronoi honeycomb structure [33]. In this way, each layer will contain two categories of material deposition pattern (i) value added high resolution external contour and (ii) sparse internal porous architecture. By stacking the bi-modal layers pattern, the complete object can be printed with relatively faster speed in the machine build plate at once.

However, this shell/skin and frame structure technique [37] will introduce uncured trapped material inside the object in processes like powder bed fusion, sheet lamination, vat polymerization, binder jetting etc. or trapped support material in extrusion based process (see Figure 11). Removing the uncured material from the internal space of hollow objects can be tedious, time consuming, and sometimes not possible. This often require part design modification (e.g. putting holes in liquid base AM system or modular design for solid material) and/or complex post-processing to remove trapped volume.

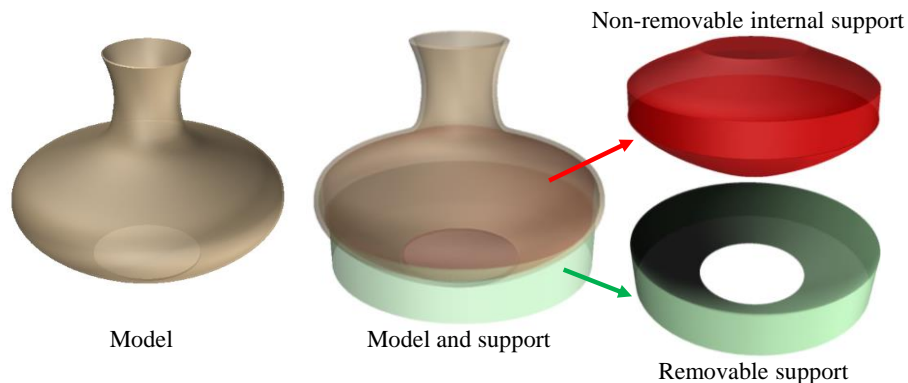


Figure 11. Support entrapment into thin-wall/shell object.

There are several other factors associated with the objects that demand increased amount of resources in 3D printing processes. For example, the existing 3D printing machines often suffer from their limited printing volume when larger objects do not fit into the printing envelop of a given printer. The build time for larger objects with higher build height significantly

increases due to the increased number of layers. Layer geometries also play a prominent role in the manufacturability of an object. Contour plurality and non-uniform layer geometries [23, 25] resulting from curved free form shaped objects dramatically increase fabrication complexity in additive manufacturing processes. The curved free-form shaped objects sometimes demand sacrificial support material as well depending on the object geometry.

Splitting objects into discrete segments can solve the problem of limited print area. Also, a careful discretization of curved free-form shaped object into segments may result in uniform layer geometries of the object segments. For larger objects, Luo *et al.* [85] proposed an object partitioning approach where objects larger than the working volume of a 3D printer were partitioned into smaller parts so that each of the parts fit into the printing volume. Several partitioning criteria such as assemblability, joining interface, areas of high mechanical stress, object symmetry etc. were taken into account in the segmentation process. Vanek *et al.* [86] developed a mesh segmentation and packing approach where the 3D objects were first converted into shells and then segmented into smaller parts. It was shown that the overall support material and build time were reduced due to partitioning and packing the segments in the print envelop. Recently, Jiang *et al.* [87] has demonstrated a skeleton based partitioning technique for large objects considering the integrity of meaningful parts. However, the object geometry and fabrication complexity have not been considered while partitioning the object model. Therefore, object segments obtained using these techniques may have inhomogeneous surface characteristics due to sharp change in curvature. The dissimilarity in the segment surface characteristics can contribute towards the amount of support volume and complex layer geometry with concave areas (see Figure 12), which eventually can lead to increased build time, resources, and cost [23]. Some other 3D mesh segmentation techniques [88-91] proposed in

literature segments the object intuitively into meaningful features which are not fully intended for 3D printing process. Table 3 demonstrates a summary on the recently proposed object segmentation techniques for 3D printing, and their strengths and limitations.

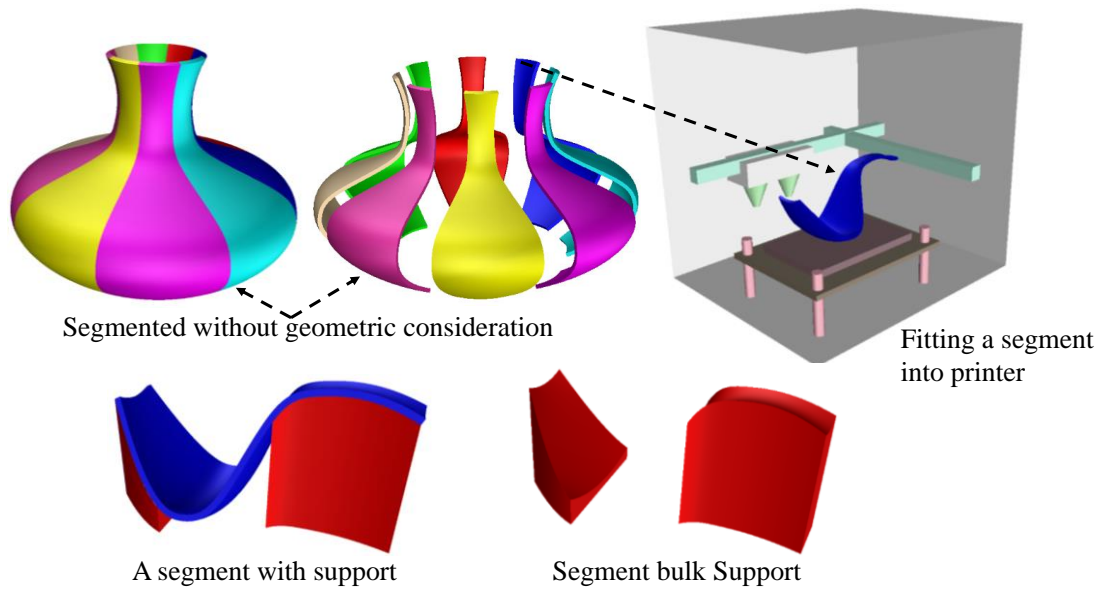


Figure 12. Model segmentation without considering geometry.

Table 3. Existing object segmentation techniques for 3D printing.

Techniques	Pros	Cones
Chopper [85]	Considers assemblability, large joining interface, areas of high mechanical stress, and symmetry.	Introduces planer cuts for segmentation, which may always not suitable for freeform shaped objects.
Models partition using skeleton [87]	Based on meaningful features, symmetry, and assemblability.	Not intended for shell model or shell of hollowed solid objects. Object geometry was not considered.
PackMerger [86]	Partitions shell into equal volume segments to pack in the print envelop.	Focused on packing and object geometry was not considered.
Level-Set-Based Partitioning [92]	Considers stress load, surface details, interface area, packed size, printability, and assembling.	Geometry and Support structure material were not considered.
Dapper [93]	Primarily focused on packing in the print envelop.	Works for solid models and does not consider object geometry.
Pyramidal Shape Decomposition [94]	Segments into approximate pyramidal shape for FDM process.	Not beneficial for shell model or shell of hollowed solid objects.
RoboFDM [95]	Each segment is printed one upon another along different directions by rotating the platform such that support material can be avoided.	Not always applicable for printing free form shaped shell of a hollowed object. Object size is restricted by the capacity of the robotic arm.
RevoMaker [96]	Prints partitioned geometries around revolving cube. Every object is partitioned into six segments.	Since the whole object is printed on a cuboid base, object size is limited to print envelop. Not suitable for hollowed solid objects.
CofiFab [97]	Similar to RevoMaker, but utilizes convex polyhedron as the internal base.	Same as RevoMaker

Hollowing the curved free form shaped thin wall objects can further be done by putting repetitive patterns on the part wall and cutting out the interior of the patterns. These repetitive cutout patterns on thin wall objects are used for decorative purpose, easy uncured material removal, light weighting, or other functionality such as ventilation/air pass. The by-example pattern synthesis algorithm demonstrated by Dumas et al. [98] generates patterns as surface texture based on a given example pattern considering both appearance and structural properties of the object. Zehnder et al. [99] proposed a decorative surface patterning technique formulated as energy minimization which creates ornamental curve networks on the object surface based on

user-defined spline curves as the design primitives. Schumacher et al. [100] also presented an example pattern based cutout pattern/stencil generation technique taking aesthetics, stability, and material efficiency into account. The distribution and scaling of the patterns on object shell were determined solving an energy minimization problem. A stochastic search and a boosting algorithm proposed by Chen et al. [9] were used to cover an object surface with thin patterns termed as filigree. This filigree synthesis was posed as a packing problem with a focus on appearance. Besides providing some advantages, the thin wall objects with cutout patterns, however, suffers from fabrication complexity. For example, the overhang sections of the hollow cutout patterns frequently require increased amount of support structure from both outside and inside of the object. Again, support removal becomes another challenge because of the thin hollow sections of the object wall.

Several methods reported in literature focus on determining the optimal AM pre-process plan (build orientation and toolpath direction) considering factors such as support volume [101-103], surface quality [23, 101, 102, 104-108], build time [23, 24, 101, 104-106, 108, 109], the number of tool turns [110], and tool start-stops [23, 24, 111]. However, optimal process plan for the whole object may sometimes be unable to substantially reduce the fabrication complexity and support material requirement due to the nature of the object geometry. For instance, changing the build orientation of the object shown in Figure 11 can manipulate the amount of external support but cannot avoid the internal support material. Furthermore, the fabrication complexity arising from the presence of excessive tool start-stops and direction change, and thin features in the layers of concave shaped objects cannot always be fully eliminated by changing the toolpath direction [23, 25]. Again, slanted or curved surfaces with respect to the build vector may result in poor surface quality [23], and may need higher amount of support structure and build time.

Consequently, objects partitioning without considering segment geometry could also transfer the existing fabrication complexity and support volume of the object to its individual segments.

Thus, partitioning methodology for 3D printing of objects needs to consider the geometry of the object segments in order to simultaneously reduce the fabrication complexity, support material, and build time. Besides, in case of printing hollow thin wall objects with cutout patterns, support material can be trapped inside the object and hollow patterns and it is often difficult to remove. Therefore, segmentation of both curved and hollow objects and then creating lattice shell segments by cutout patterns would reduce support material and accommodate the intended functionality.

In the earlier sections of this Chapter it is also seen that different forms of porous structures can be used to improve the functionality in various applications such as structural materials, energy absorbing foams, heat exchangers, phononic band gap structures and biomedical applications. Among them the use of porous structures in biomedical applications such as bone and other tissue scaffolds and implants can facilitate tissue regeneration process. The following section reviews the porous infills used in biomedical applications.

2.4. Porous Infill Structures for Biomedical Applications

Porous structures have been frequently used for biomedical applications [112]. Porous cellular materials can be tailored by changing the structural parameters for different functionalities in applications such as prostheses and orthoses, implants, and tissue scaffolds. Prostheses are the biomedical devices typically used to substitute a lost or damaged limb and orthoses are the devices or braces used to improve the functionality or correct the alignment/disorder of injured limbs. Traditional prosthetics and orthotics are solid and the fabrication techniques are labor intensive and require longer build time. However, light weight

custom prosthetics and orthotics can be designed with cellular structures for enhanced performance and can be fabricated with additive manufacturing techniques with better control on the design. Jin et al. [113] has summarized the additive manufacturing along with traditional method for custom prosthetics and orthotics.

Because of the unique features of porous cellular/lattice structures, such structures can be utilized to design implants making them lightweight and structurally stable for longer duration of time [114]. The interconnected pores of cellular structures promote better nutrient flow, osteoblastic proliferation, and stronger bone ingrowth and osteointegration [115]. In addition, porous implant structure stiffness can be tailored to reduce the effect of stress shielding [116-119]. Stress shielding is caused by the stiffness difference between the implant the surrounding tissue. When the implant is stiffer than the surrounding bone tissue, loading is carried by the implant. As a result, the surrounding bone tissue grows weaker due to experiencing less loading and ultimately fails [119].

In tissue engineering and regenerative medicine, porous scaffolds with cellular structure have great potential to be used as a guiding substrate for three-dimensional (3D) tissue repair and regeneration process. The microstructures of tissues and organs are heterogeneous which provides multi-functionality such as mechanical, chemical, and biological. Therefore, tissue scaffolds and implants need to be designed to match the target tissue's mechanical and chemical properties such as strength, stiffness, biodegradability, surface chemistry etc. while mimicking its interconnected pore network for cell ingrowth and migration, and nutrient transport [16, 120-122]. For example, bone tissue engineering requires porous open cellular structures creating mechanical environment of bone, promoting bone cell ingrowth, vasculature development, and

facilitating nutrient and gas transport [15, 123, 124]. Moreover, in biological systems, the pore size and structural porosity vary with tissue type, location, and function [125].

Therefore, higher level of porosity and interconnectivity allows increased cell-to-cell interaction, cell migration, and nutrient and gas permeability throughout the scaffold structure, which can lead to more cell attachment, extracellular matrix production, and tissue growth [120, 126-132]. However, increased porosity can impair the mechanical properties of the scaffold since the strength and stiffness of a scaffold is directly related to its internal architecture [120, 133-135]. This indicated that a good compromise between porosity and mechanical properties is necessary for a functional scaffold.

Several efforts have been reported in literature to determine appropriate scaffold porosity and pore size for tissue regeneration. The appropriate porosity distribution and pore size were experimentally determined through culturing cell in a set of scaffolds with different porosity distribution and pore size. In most cases, there was no spatial control on the porosity distribution across the structure; and the porosity as well as the pore size were stochastic and dependent on fabrication process. For instance, collagen scaffolds with different pore size were experimented for cartilage tissue regeneration and it was found that scaffolds with pore size of 150–250 μm best promoted the formation of cartilage and improved its mechanical properties [136]. Again in some studies with similar experiments, pore sizes above 300 μm [128, 137, 138], 140 μm [139], and 92 μm [130] were recommended for formation of bone, vascularization, and ECM. In a similar fashion, the effect of porosity on tissue ingrowth has been investigated to determine appropriate porosity. Ji et al. [130] observed that increased porosity in chitosan scaffold resulted in higher cell viability over 7 days cell culture. In another study, porosity above 75% was recommended for better cell proliferation [140]. However, Danilevicius et al. [17] demonstrated

that polylactide scaffolds with 86% porosity promoted more cell proliferation for bone regeneration than those with 82% and 90% porosity. Thus, there exists significant disparity in results obtained from different experimental settings.

Therefore, determining the appropriate scaffold porosity distribution for the regeneration of a target tissue through experiment is laborious and time consuming. Moreover, the porosity/permeability requirement varies for different implant sites and tissues/organs. As a result, the information about the porosity requirement for an implant site cannot be used for other sites. Furthermore, the internal architecture of organs/tissues are heterogeneous and vary from patient to patient. Thus, it is not practically viable to experimentally determine the porosity distribution for patient specific custom scaffold/implant.

The internal architecture of tissues and organs are heterogeneous which provides multi-functionality such as mechanical, chemical, and biological. The pore size and structural porosity in biological systems vary with tissue type, location, and function [125]. Thus, scaffolds designed with homogenous property and material distribution without considering the internal architecture do not adequately represent bio-mimicry [141-143]. Consequently, instead of using scaffolds with random porosity distribution, individual patient specific tissue repair and regeneration requires bioinspired scaffolds and implants that need to be designed to mimic the structural and biological characteristics of the target tissue [122, 144]. However, both modeling and fabrication of intricate internal architecture of the biomimetic scaffolds and implants are challenging.

Several scaffold fabrication techniques are available and can be classified into two broad categories: i) non-Additive Manufacturing (AM), and ii) bio-AM technique. Recently bio-additive manufacturing systems have become an attractive tool for developing porous scaffolds

because of the improved spatial resolutions [145, 146] and the ability to control the variational architecture and free form geometry of scaffolds and other porous biomedical devices [135, 145, 146]. The current bio-additive manufacturing process is the surrogate of status quo AM process where STL being the *de facto* file format. The desired shape is constructed with CAD or extracted by reverse engineering process and is converted to STL-surface model. The STL model is then sliced by a set of parallel planes to determine the layer contours. All the contours are planar closed curves and have the same (positive) orientation. When materials are deposited in each of these layers and stacked consecutively, a 3D scaffold structure is obtained.

In tissue regeneration process, the scaffold topology needs to be similar to the natural tissue to promote cellular functions [147]. However, often time the scaffold CAD model is generated as the boundary representation (B-rep) of the targeted shape and does not capture the internal architectural information of tissues. Moreover, the internal heterogeneous architecture is simplified with ‘homogenization’ methods. In biological systems, the pore size and structural porosity vary with tissue type, location, and function [125]. Thus, scaffolds designed with homogenous property and material distribution without considering the internal architecture do not adequately represent bio-mimicry [141-143]. Besides, the STL conversion is a surface approximation technique, which introduces loss of information in the form of chordal error, truncation error, dangling face or puncture gap in the model, and erratic nature of the model surface due to incomplete or inconsistent facet normal. Using the model with these errors will pile-up more errors in each subsequent step (build orientation, slicing, tool-path planning) of process plan. Thus there is a clear gap in the design representation of bio-scaffold models that translate to downstream inaccuracy of the bio-AM process.

In CAD-based scaffold design approach, unit cells were formed and characterized from primitive geometries and a library for scaffold structure was developed with the unit cells. An automatic assembly process was demonstrated to periodically arrange the unit cell selected from the library and match the anatomical shape of the scaffold structure [148-150]. Bucklen et al. [151] also presented a library of unit cells composed of bio-inspired features where the unit cells were selected based on the density map of the scaffold structure. In order to fabricate patient specific implants, Salmi et al. [152] and Fantini et al. [153] used medical images to reconstruct the anatomical shape and CAD model of defective bones.

Several works have been done on topology optimization techniques to design the internal architecture of porous scaffolds and implants [16, 154]. Challis et al. [155] optimized scaffold topology on the basis of scaffold stiffness and diffusive transport. In the topology optimization process, suitable scaffold porosity was chosen to match the scaffold stiffness to bone stiffness. Dias et al. [156] also proposed a scaffold topology optimization algorithm for given mechanical conditions and permeability. The topology optimization was performed on a unit cell considering the scaffold as homogeneous periodic structure. An asymptotic homogenization method was used to compute the permeability and elastic property of the scaffolds. Periodic porous scaffold structures were also designed with triply periodic minimal surfaces (TPMS) represented with trigonometric functions [157-159]. However, most of these design techniques create complex scaffold architecture with little or no consideration of continuity and connectivity between neighboring unit cell. Furthermore, most of the topology design techniques create the scaffold architectures that do not mimic the physical properties of original microstructure of the target tissue. These methods do not also consider the manufacturability of the designed scaffold structure assuming AM's capability of building any complex geometry and structure.

Additionally, seamless data corridor between design (virtual) and manufacturing (physical) is often ignored which is necessary for the manufacturability of the constructed heterogeneous architecture.

3. NOVEL HONEYCOMB INFILL PATTERN FOR ADDITIVE MANUFACTURING

3.1. Introduction

In additively manufactured parts, infills are primarily used to support the shell/skin of the part from collapsing and to provide a print base for the skin hanging over the interior of the part. Infill are also used to reduce the material volume by hollowing the interior of the object [23]. AM offers the capability of making prismatic lattice infills without the use of any special tooling, resulting in light weight objects with higher strength to weight ratio. Hollowing out the object can impair the structural integrity of the object. Also, sometimes the use of infill becomes inevitable because the object skin requires interior support for printing. Conversely, as it is a common assumption that the infill does not add value to the final part, thus infill deposition often gets less attraction from the AM user community and is considered a proprietary pattern for the process software. The most common infill patterns available on slicing and 3D printing software is 0° - 90° zigzag and honeycomb with uniform density. As having a carefully designed deposition pattern can help reduce the build time, the 0° - 90° zigzag pattern has been optimized with other angle combinations for different object geometries [23-25].

The infill meso-structure, which is sometimes designed considering factors such as build time, surface finish and support material, has a strong correlation with the physical properties of the object [83]. Both intrinsic and extrinsic properties of the object can be controlled through the infill meso-structure. For instance, the material layout patterns are investigated for structural integrity [160] and other physical attributes including pore size and geometry [161]. Adaptive layout patterns [162] have been utilized to achieve desired infill porosity.

Conventional uniform honeycomb structures with different relative density have been designed through varying the cell wall thicknesses [31]. Likewise, non-uniform honeycomb

structures with graded designed have been designed through varying the cell wall thicknesses in the selected regions of the structures [32]. The thicker cell walls in such structures requiring multiple pass introduces discrete toolpath segments with increased amount of fabrication interruptions and chances of fabrication defects. Some non-conventional infill patterns such as skin-frame structures [36, 37] have been pronounced in literature as well. However the strut-node frame nature of such structures creates challenges in printing due to tiny layer contour geometries and the resulting increased tool start-stops and air travel.

In this research, a new fabrication pattern for honeycomb infill is proposed for additive manufacturing application. The proposed pattern will uniformly distribute the material and can accommodate controllable variational honeycomb infill while maintaining continuity with relative ease. First, the honeycomb unit cells geometry is defined for uniform and non-uniform voxel size. A continuous tool-path scheme is then designed to achieve the honeycomb structure with uniform wall thickness. The tool-path is characterized and compared with the traditional 3D printing honeycomb tool-path for which the wall thickness is not uniform. The infill structures are fabricated with both uniform and variational pattern which are then compared with the traditional tool-path pattern with compression testing. The results show that the proposed design demonstrate uniform densification under compression and performs better while absorbing more energy.

3.2. Definition of Unit Cell for Novel Honeycomb Pattern

The existing or traditional uniform hexagonal honeycomb infill patterns usually employ duplications of filaments by running two filaments side by side creating non-uniform wall thickness as shown in Figure 13. This pattern is generated by the open source Slic3r application [163] embedded in Repetier-Host software package [164] widely used for the open source 3D

Printers. In this pattern, three consecutive layers together make a complete honeycomb cell layer where the filaments along the cell walls among the three layers follow $0^\circ-60^\circ-120^\circ$ layout pattern. The unit cell construction given in Figure 13(c) demonstrates that each cell wall consists of two adjacent filaments in only one layer and one filament in the other two layers. This results in 2-1-1, 1-2-1, and 1-1-2 formation sequence of filaments making each side of honeycomb unit cell. However, filaments in two sides of the cell are shared with adjacent cells resulting in 1-.5-.5 sequence of filaments making these two sides as shown in Figure 13(c).

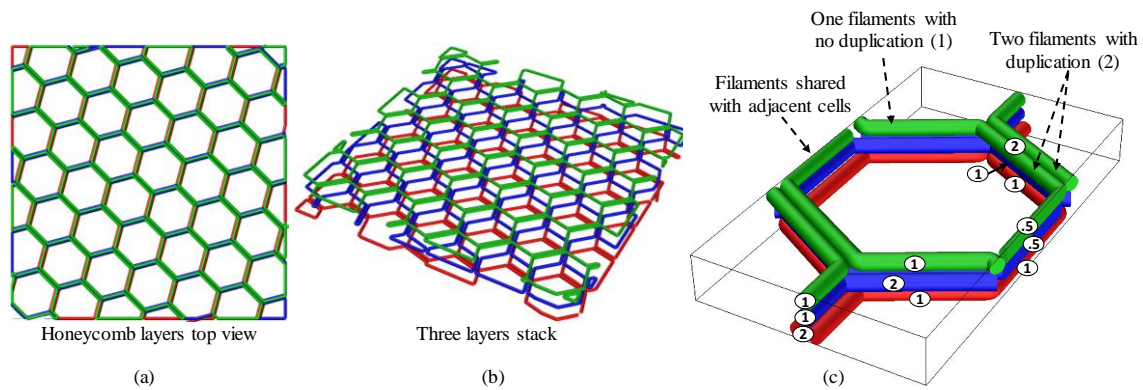


Figure 13. (a) Top view, (b) three layers stack, and (c) unit cell configuration with formation sequence 2-1-1, 1-2-1, and 1-1-2 of the traditional honeycomb infill tool-path.

In order to generate gradient as well as uniform density infill and reduce the toolpath overlaps and tool air travel, a continuous toolpath scheme is proposed for hexagonal honeycomb infill. To model a generic hexagonal honeycomb unit cell, a rectilinear representative unit deemed as a voxel is first defined with parameters L_x and L_y in the standard Cartesian coordinate system, where L_x and L_y are length and width of the voxel along X and Y axes, respectively as shown in Figure 14. (a) Now, this voxel is discretized along L_x and L_y and the honeycomb cell parameters a , b , and c , where $c = 2a$ are derived as shown in Figure 14(a,b). This unit cell is composed with three layers to make continuous toolpath resulting a 3D unit cell as shown in

Figure 14(d,e). The total filament length inside one 3D unit cell will be $4a + 8b + 4(c/2)$. Here, all the c struts of the unit cell are shared by the adjacent cells and hence halves of the c struts belong to the unit cell which can be seen in Figure 14(e). Now, if the voxel is discretized into 1/6 units

of L_x and L_y , the unit cell parameters can be derived as $a = \frac{1}{6}L_y$, $b = \sqrt{\frac{1}{4}L_x^2 + \frac{1}{36}L_y^2}$, and

$c = 2a = \frac{1}{3}L_y$. When the filament diameter is d , the total material volume, $V_{lattice}$, inside the 3D unit cell can be calculated using Equation (1).

$$\begin{aligned} V_{lattice} &= \frac{\pi}{4}d^2(4a + 8b + 2c) \\ &= \frac{\pi}{3}d^2(L_y + \sqrt{9L_x^2 + L_y^2}) \end{aligned} \quad (1)$$

The voxel parameters L_x and L_y may have any of following relations: $L_x = L_y$, $L_x > L_y$, or $L_x < L_y$. If a non-square bounding voxel is considered such that $L_x = \frac{1}{\sqrt{3}}L_y$, the resulting honeycomb cell becomes the regular hexagon with all equal sides and 120° interior angles between sides as shown in Figure 14(b). Thus, the relative density of the cell ρ^* , which is the ratio of lattice cell material volume $V_{lattice}$ to solid cell (voxel) material volume V_{solid} , can be represented in terms of L_y by Equation (2).

$$\rho^* = \frac{V_{lattice}}{V_{solid}} = \frac{\pi d}{\sqrt{3}L_y} \quad (2)$$

Therefore, for a given infill density ρ^* of a layer, the voxel parameters for the regular hexagonal honeycomb cell can be determined using Equations (3–4). Then, the infill layer can be voxelized and honeycomb cells can be fitted to generate the layer by layer continuous toolpaths as represented in the next Section.

$$L_x = \frac{\pi d}{3\rho^*} \quad (3)$$

$$L_y = \frac{\pi d}{\sqrt{3}\rho^*} \quad (4)$$

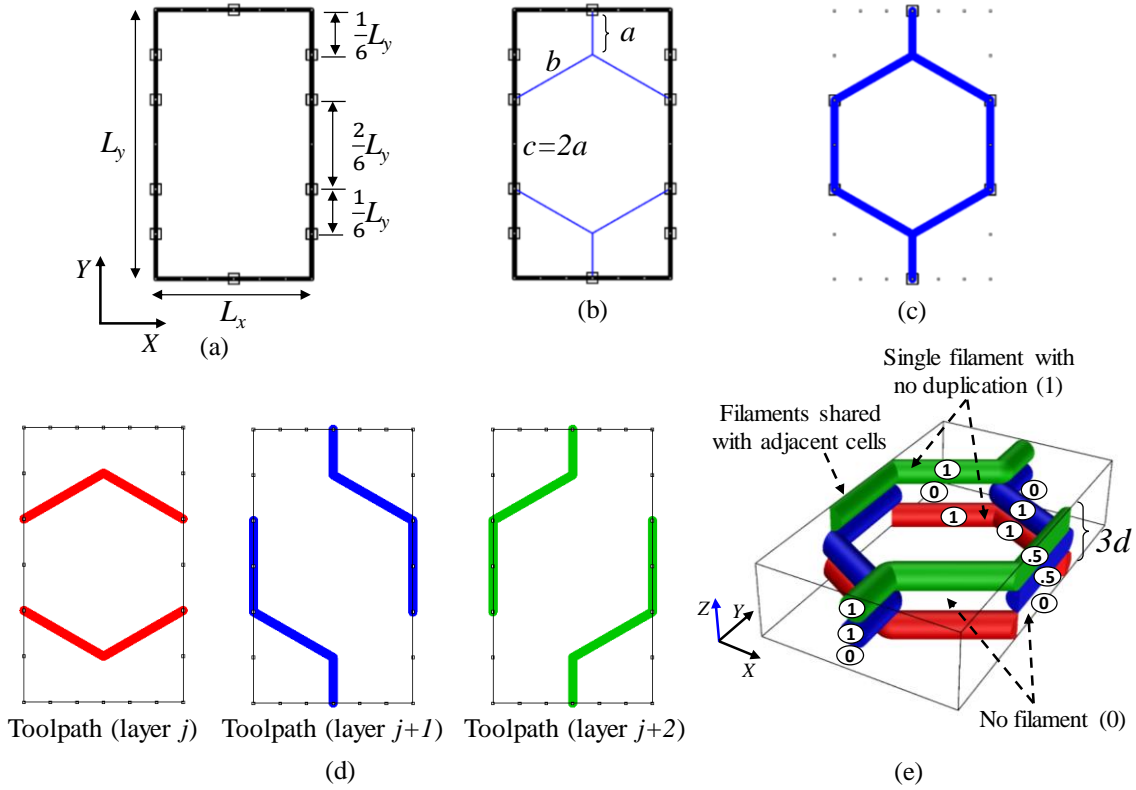


Figure 14. Proposed honeycomb unit cell using 1/6 division design parameter for continuous toolpath: (a) voxel definition, (b) hexagonal honeycomb cell definition, (c) 2D unit cell representation, (d) sublayer toolpath segments constituting a unit cell, and (e) the resulting 3D unit cell with 1–0–1, 1–1–0, and 0–1–1 formation sequence.

In the proposed honeycomb cells, two filament segments appear along each unit cell wall in the three layer arrangement (see Figure 14). The unit cell construction shown in Figure 14(e) demonstrates 1–0–1, 1–1–0, and 0–1–1 formation sequence of filaments making the sides of honeycomb unit cell in the three layer arrangement.

In contrast, the traditional 3D printed honeycomb cells are regular hexagon with all equal sides and 120° interior angles between sides. Thus, analogous to the proposed honeycomb cell

definition, the traditional honeycomb infill can also be represented with voxels parameterized by

$L_x = \frac{1}{\sqrt{3}}L_y$, $a = \frac{1}{6}L_y$, and $b = c = \frac{1}{3}L_y$ as shown in Figure 15. The 3D unit cell can again be easily decomposed into three layers as shown in Figure 15(d,e). The total filament length inside one 3D unit cell will be $8a+16b+4(c/2)+2c$. Here, the c struts in the top two layers (blue and green colored layers in Figure 15(d,e) of the unit cell are shared by the adjacent cells. Thus, a half of each c strut in top two layers and a whole of each c strut in the bottom layer belong to the unit cell. Considering the filament diameter as d , the total material volume, $V_{lattice}$, inside the 3D unit cell can be calculated using Equation (5).

$$\begin{aligned} V_{lattice} &= \frac{\pi}{4}d^2(8a+16b+4c) \\ &= 2\pi d^2L_y \end{aligned} \quad (5)$$

Thus, the relative density of the cell ρ^* can be expressed in terms of L_y by Equation (6).

$$\rho^* = \frac{V_{lattice}}{V_{solid}} = \frac{2\pi d}{\sqrt{3}L_y} \quad (6)$$

Therefore, for a given infill density ρ^* of a layer, the voxel parameters for the traditional regular hexagonal honeycomb cell can be determined using Equations (7–8).

$$L_y = \frac{2\pi d}{\sqrt{3}\rho^*} \quad (7)$$

$$L_x = \frac{2\pi d}{3\rho^*} \quad (8)$$

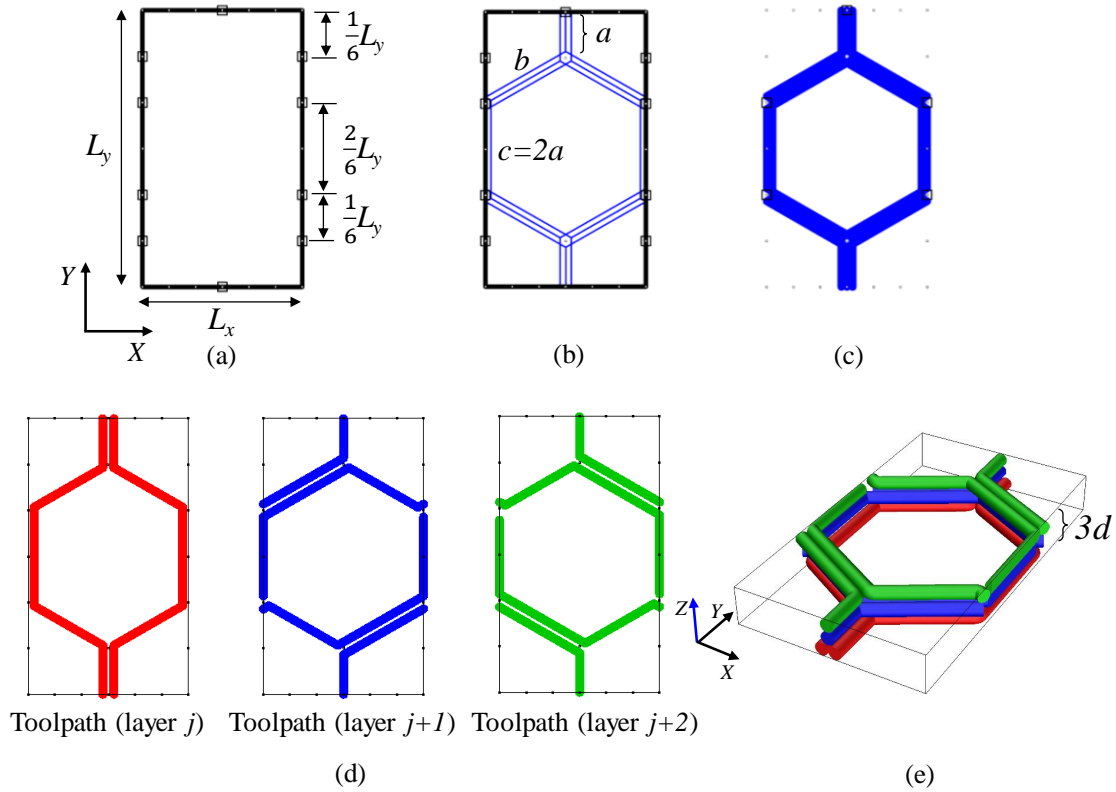


Figure 15. Traditional honeycomb unit cell: (a) voxel definition, (b) hexagonal honeycomb cell definition, (c) 2D unit cell representation, (d) sublayer toolpath segments constituting a unit cell, and (e) the resulting 3D unit cell.

Therefore, Equations (2) and (6) indicate that the relative density of traditional honeycomb unit cell is twice the relative density of proposed honeycomb unit cell with $1/6$ division design parameter for the same size of a voxel. Consequently, for a given relative density ρ^* , the proposed cell size parameters (L_x and L_y) will be half the size of the traditional cell parameters. This unit cell size and density relationship for both proposed and traditional honeycomb cells is further illustrated with Figure 16. Thus, the proposed honeycomb infill design accommodates smaller cells (half of its counterpart) compared to the existing regular hexagonal honeycomb infills for the same relative density. This feature of the infill can provide better support to the object skin resulting in enhanced surface quality and wall strength.

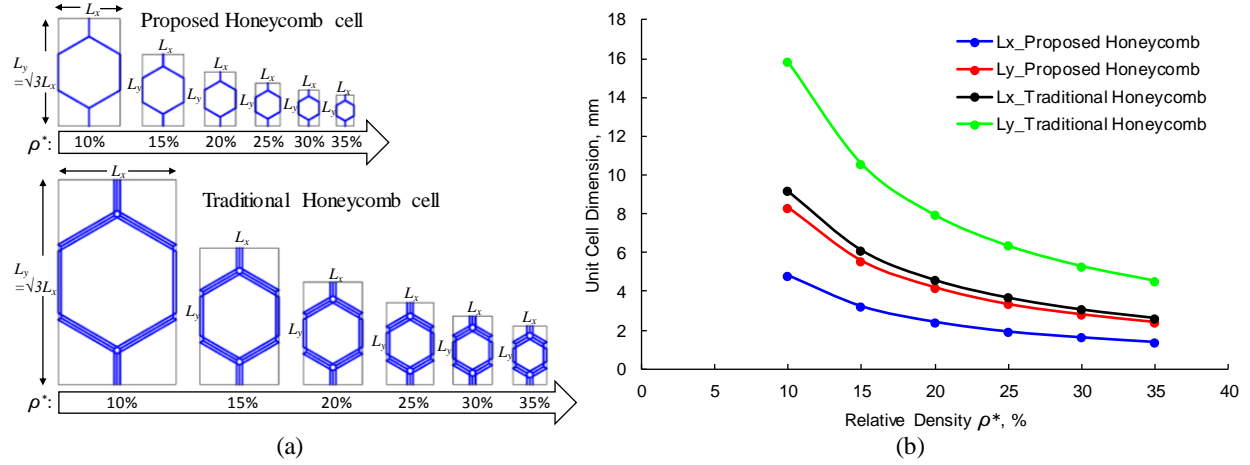


Figure 16. (a) Proposed and traditional unit cells with different size and density and (b) Relationship between unit cell size parameters and relative density for proposed and traditional honeycomb cells with 1/6 design parameter.

For a square voxel ($L_x = L_y = L$) discretized into 1/8 units of L_x and L_y , if the cell parameters are considered as $a = \frac{1}{8}L_y$, $b = \frac{1}{4}\sqrt{4L_x^2 + L_y^2}$, and $c = 2a = \frac{1}{4}L_y$ (see Figure 17), the total material volume ($V_{lattice}$) inside the 3D unit cell can be obtained from Equation (9).

$$V_{lattice} = \frac{\pi}{4}(1 + 2\sqrt{5})d^2L \quad (9)$$

In a similar fashion, the relative density of the cell, ρ^* can be represented by Equation (10). Consequently, the voxel parameters can be determined using Equations (11).

$$\rho^* = \frac{(1 + 2\sqrt{5})\pi d}{12L} \quad (10)$$

$$L = \frac{(1 + 2\sqrt{5})\pi d}{12\rho^*} \quad (11)$$

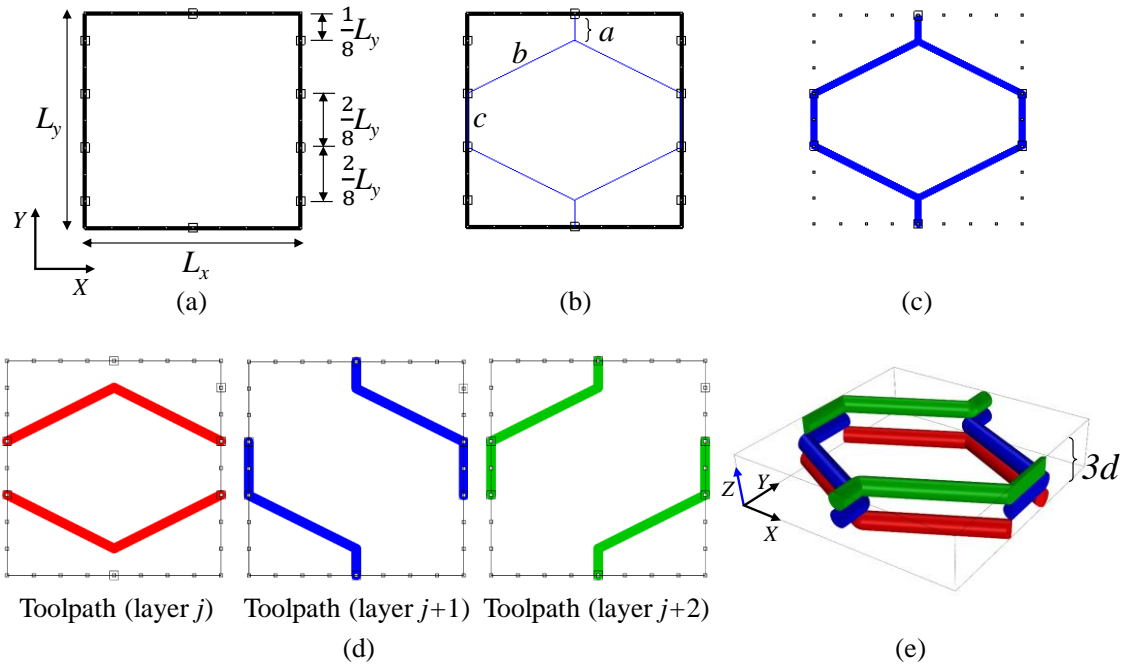


Figure 17. Proposed honeycomb unit cell designed using 1/8 division design parameter for a square voxel: (a) voxel definition, (b) hexagonal honeycomb cell definition, (c) 2D unit cell representation, (d) sublayer toolpath segments constituting a unit cell, and (e) the resulting 3D unit cell.

In Figure 18 the proposed and traditional cell patterns can be compared based on how many cells can be fitted in a given space. Compared to the traditional honeycomb cell, four times of the number proposed cells (both 1/6 and 1/8 division types) can be fitted in a given space for a given relative density. Furthermore, while packing cells in a given space, the proposed cell types researches 100% relative density (solid) with moderate gradient resulting in increased number of cell packing as show in Figure 18.

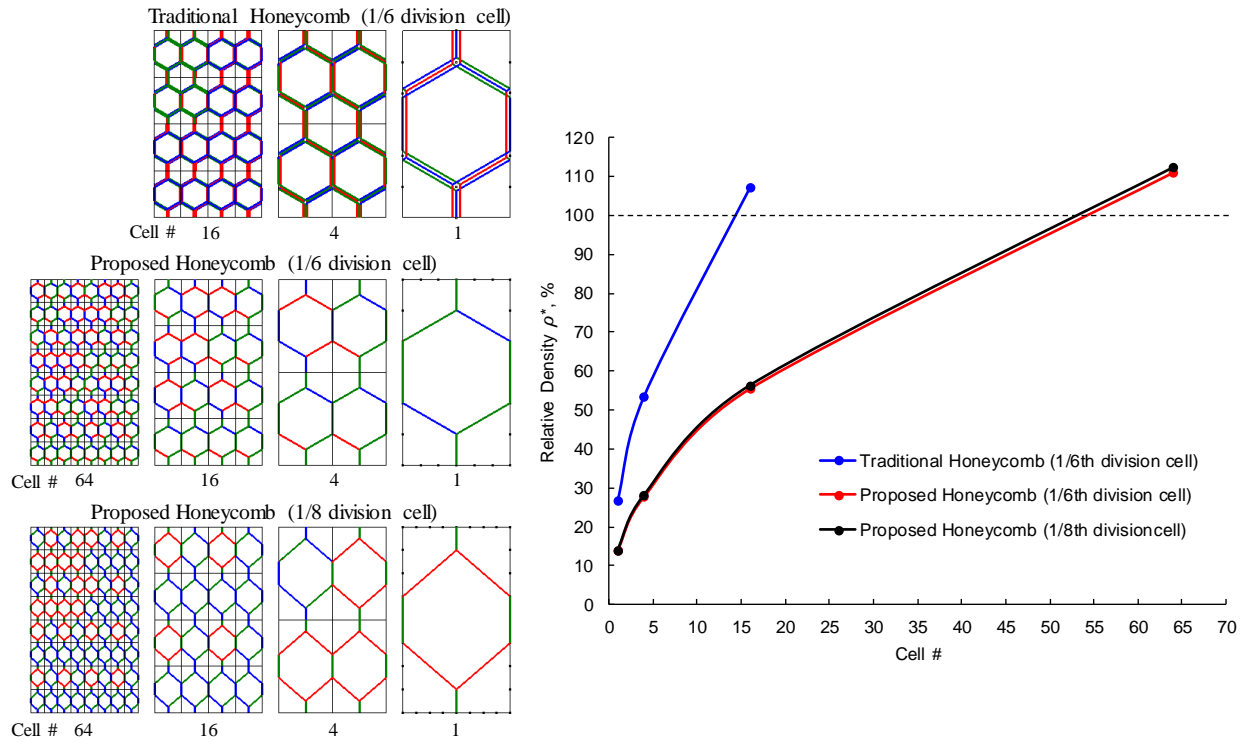


Figure 18. Relationship between Cell packing and relative density for three types of honeycomb cells.

3.3. Infill Space Voxelization

For a given relative density of each infill layer/slice, the voxel parameters (size) L_x and L_y can be derived from either Equations (3–4) or Equations (10–11). Then the infill layer can be voxelized using the calculated voxel parameters as shown in Figure 19. Voxelization is performed with parallel grid lines of spacing L_x and L_y along X and Y -directions, respectively, in the standard coordinate system. The start points along both directions are the lower extreme values of X and Y . The intersection points of the grid lines determine the voxels. After voxelization, honeycomb parameters a , b , and c are determined and honeycomb cells are fitted inside the voxels as represented in Figure 19. For honeycomb structures with variational density distribution, the relation between L_x and L_y will vary throughout the structure in accordance with

the density distribution. Therefore, elongated/flattened hexagonal cells and resulting irregular interstitial hexagonal cells will appear as depicted in Figure 19.

For vibrational infill, the relative density may follow continuous distributions ρ_x^* and ρ_y^* along X and Y -directions, respectively. In this case, the parallel grid lines along both X and Y -directions are determined by plugging the locations of the immediate previous X and Y grid lines, respectively, into the continuous density functions. Hence, like other unit cell based cellular structures, this voxelization represents a discrete approximation of the continuous density distributions. Furthermore, the resultant density along the structure is determined with L_x and L_y grid lines that are controlled independently. Therefore, although the voxelization may influence the density of the neighboring cells/voxels due to the rectilinear nature of the grid lines, this process can minimize overall density approximation error.

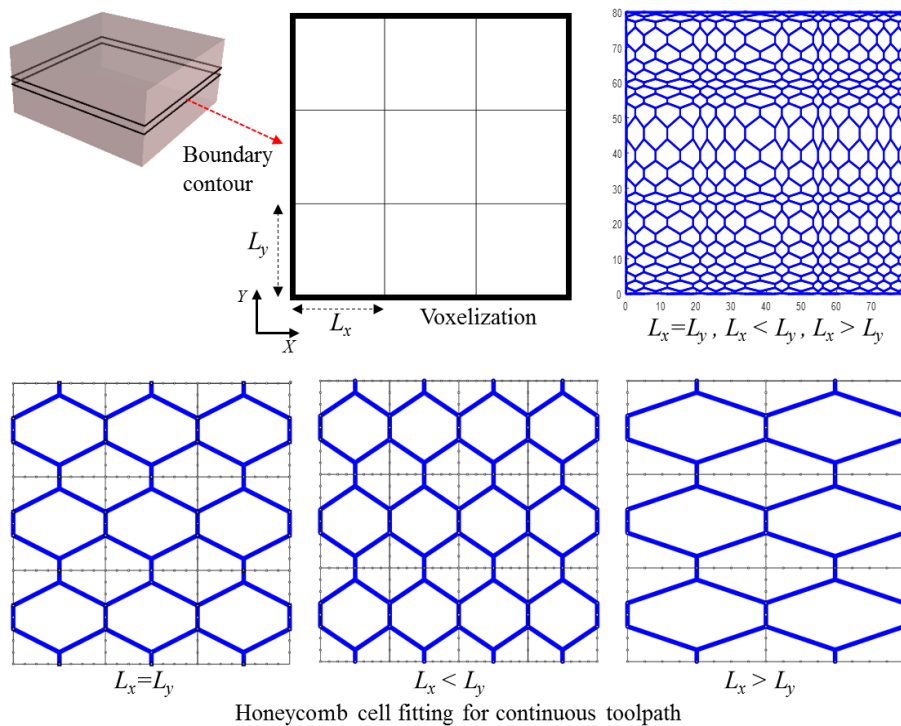


Figure 19. Infill layer discretization into representative voxel units of different sizes ($L_x = L_y$, $L_x > L_y$, and $L_x < L_y$) and honeycomb cell fitting.

3.4. Continuous Honeycomb Toolpath Scheme

The proposed honeycomb cells can be decomposed into three distinct layers of parallel kinked lines as shown in Figure 20. The parallel lines in each of the three layers are kinked in a certain pattern following the honeycomb cell geometry. Each layer's parallel kinked lines can be connected in a continuous zigzag pattern. Stacking these three sublayers, eventually results in complete honeycomb cells as shown in Figure 20. Repetitively putting this tri-layer one upon another will generate 3D honeycomb lattice. Thus each individual layer in this lattice renders continuous toolpath for 3D printing.

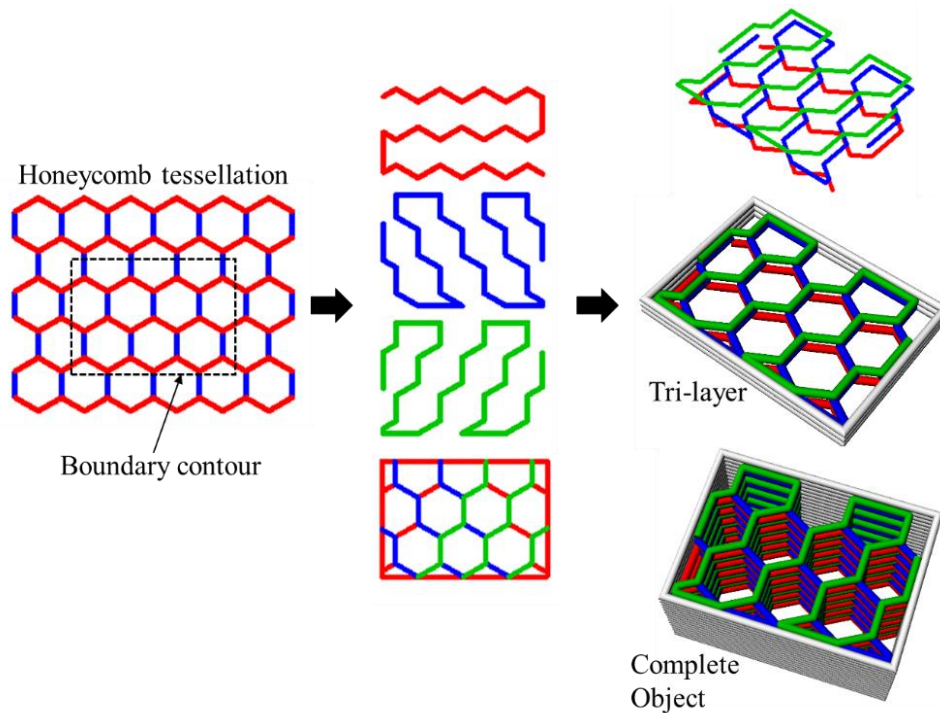


Figure 20. Honeycomb lattice form layer by layer continuous toolpath

3.5. Sample Parts Fabrication

The proposed methodology was implemented with visual basic based scripting language. The algorithm runs were performed on an Intel Core i7 @3.4 GHz CPU equipped with 12 GB RAM. In order to perform mechanical tests, variational and uniform toolpaths of a series of

sample parts with dimensions of $40 \times 40 \times 12.6 \text{ mm}^3$ were designed and fabricated. The physical relative density of both variational and uniform parts were matched to 0.23. The generated continuous honeycomb toolpaths were printed with an extrusion based AM process (Maker Select 3D Printer v2, Monoprice, Inc.) using PLA as well as TPU materials. Additionally, uniform honeycomb toolpaths generated by the open source Slic3r software [163] were fabricated. All the uniform density samples were modeled to match the mean relative density of the variational honeycomb parts. All fabricated test samples were printed with no skin, therefore they all had rough sides where the honeycomb was cut off. A sine function

$(\rho_{x,y}^*(\varphi) = 1 - \sin \varphi, 0.25\pi \leq \varphi \leq 0.75\pi)$ was used to generate the density gradient along the sample structures as shown in Figure 21. Equation (7) was used to determine the parallel grid lines for voxelization. Figure 22 depicts the proposed and traditional honeycomb toolpaths. For all the fabricated samples, the layer thickness used was 0.2 mm. Pictures of the fabricated samples are shown in Figure 23.

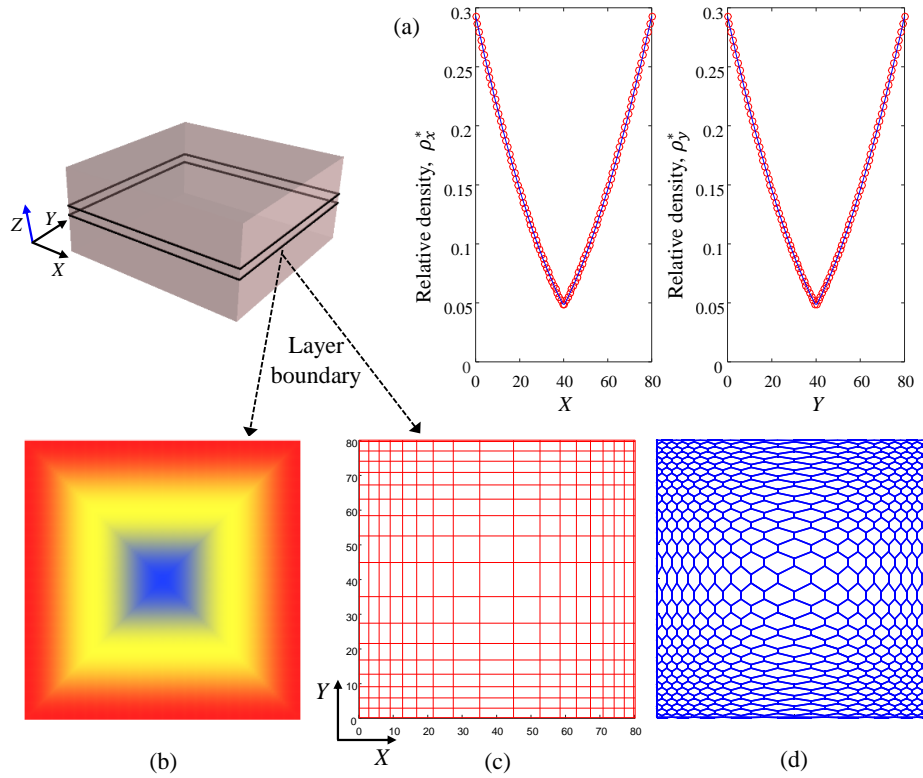


Figure 21. Function based variational density distribution of a layer (80x80mm): (a) spatial distribution of longitudinal and transverse densities, (b) color map representing resultant density gradient in the layer, (c) non-uniform voxelization, and (d) resulting variational honeycomb cell fitting and toolpath generation.

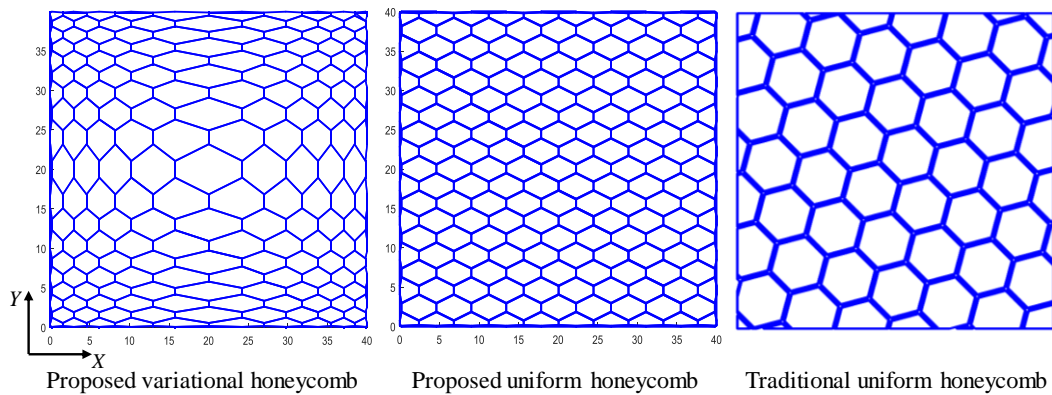


Figure 22. Proposed and traditional honeycomb toolpaths with equivalent mean relative density (23%; 40x40 mm layers).

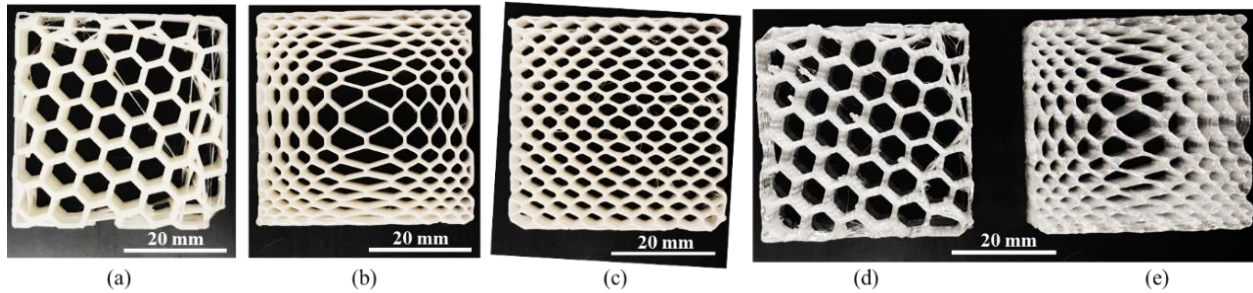


Figure 23. Fabricated samples: (a) traditional PLA honeycomb, (b) proposed variational PLA honeycomb, (c) proposed uniform PLA honeycomb, (d) traditional TPU honeycomb, and (e) proposed variational TPU honeycomb.

3.6. Mechanical Tests

The purpose of mechanical testing of the honeycomb structures was to establish their stress-strain behavior and the resulting energy absorbing capabilities under in-plane compression loading. Furthermore, the compression behavior of the designed honeycomb structures was investigated for a rigid thermoplastic (PLA) material as well as a flexible thermoplastic (TPU) material.

The in-plane compression tests were performed on the fabricated honeycomb structures with an Instron 5567 universal testing machine utilizing 30 kN load cell. The crosshead speeds applied for PLA and TPU samples were 4 mm/min and 13 mm/min, respectively. The tests were controlled and the data were recorded using Bluehill software for Instron. All the tests were recorded with a high speed camera and pictures at different strain levels were snapped from the video to illustrate the deformation and progressive failure mechanism of the lattice structures. In all cases, the Z -direction indicates the build direction for the designed and fabricated structures. Therefore, in-plane compression loads were applied to the proposed honeycomb structures along X and Y -directions to capture the mechanical anisotropy. The traditional uniform honeycombs generated by Slic3r are traditional hexagon and thus expected to have in-plane isotropic

properties [39]. Hence, they were tested along one in-plane direction. For each sample structure type, i.e., uniform, variation, and traditional, three specimens were tested along each of the two in-plane directions (X and Y).

The nominal stress ($\sigma_{lattice}$) of the lattice structures were measured by dividing the applied load by the initial cross-sectional area of the structures perpendicular to the in-plane load. The nominal lattice strains ($\varepsilon_{lattice}$) were measured from the deflection of interface between the structures and the compression platens. The stress-strain curves obtained from the measured data were used to study the compression behavior and energy absorbing capability of the sample structures.

3.7. Results and Discussion

Pictures in Figure 24 demonstrate the failure process of the proposed tool-path pattern (vairational and uniform) as well as traditional PLA honeycomb samples, which are subject to compression loading along the X -direction, at the overall lattice strains ($\varepsilon_{lattice}$) of 0%, 20%, 40%, and 60%. The failure of regular hexagonal honeycomb cells subject to a similar in-plane X -directional loading typically propagates through deformation localization along two opposite oblique (diagonal) bands intersecting each other [31]. At $\varepsilon_{lattice} = 20\%$, it can also be observed for the proposed vairational honeycomb that its deformation occurred through the failure of the diagonal cells forming two opposite bands resembling an “X” shape. Additionally, the deformation further localized through the plastic collapse of larger cells in the mid region where the two opposite bands intersected. As the load is increased ($\varepsilon_{lattice} = 40\%$), cells in the mid region start collapsing along the Y -direction. The lower density mid region with larger cells was basically responsible for this failure. The deformation of the proposed uniform honeycomb (middle row in Figure 24) started evenly through the collapse of mostly diagonal cells forming

almost perfect “X” shaped bands like the regular hexagonal honeycomb cells. However, at $\varepsilon_{\text{lattice}} = 40\%$, the failure is more prominent in the bottom half of the structure. This can be attributed to a relatively rough bottom edge of that structure which occurred during its fabrication. The traditional uniform honeycomb started collapsing asymmetrically and randomly from the bottom side and then progressively collapsed through the neighboring cells with shearing mode of deformation.

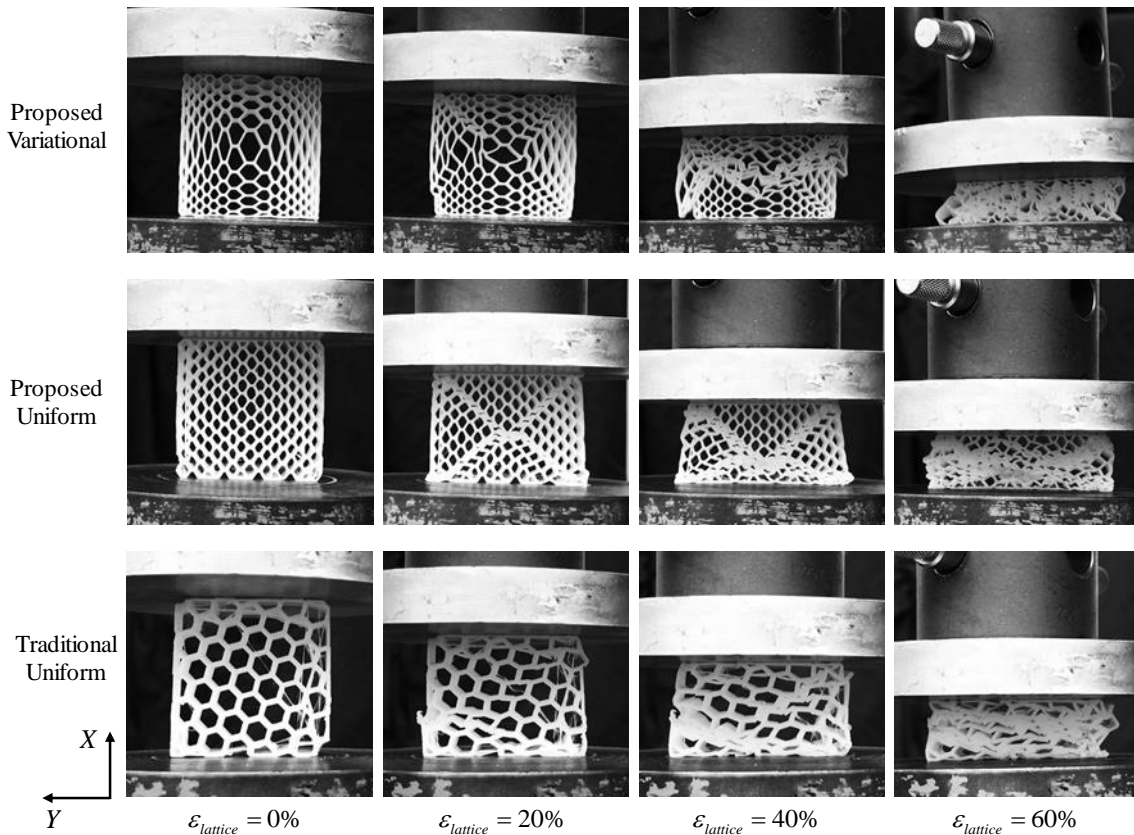


Figure 24. Compression behavior of the proposed and traditional PLA honeycombs along X-direction.

Figure 25 shows the failure processes of the PLA honeycomb samples identical to those discussed above, which are now subject to compression loading along the Y-direction. In case of proposed variational honeycomb structure, cells in the mid region were primarily deformed along the X-direction which dominated the entire failure of the proposed variational honeycomb.

The larger cells in the mid region guided the failure process. For the proposed uniform honeycomb, although yielding started through diagonal cells the structure progressively failed through an asymmetric shearing mode of deformation in horizontal rows of cells along the mid region. In both proposed structures, deformations of the cells away from the mid region were quite symmetric and homogeneous like regular hexagonal honeycombs [39, 165].

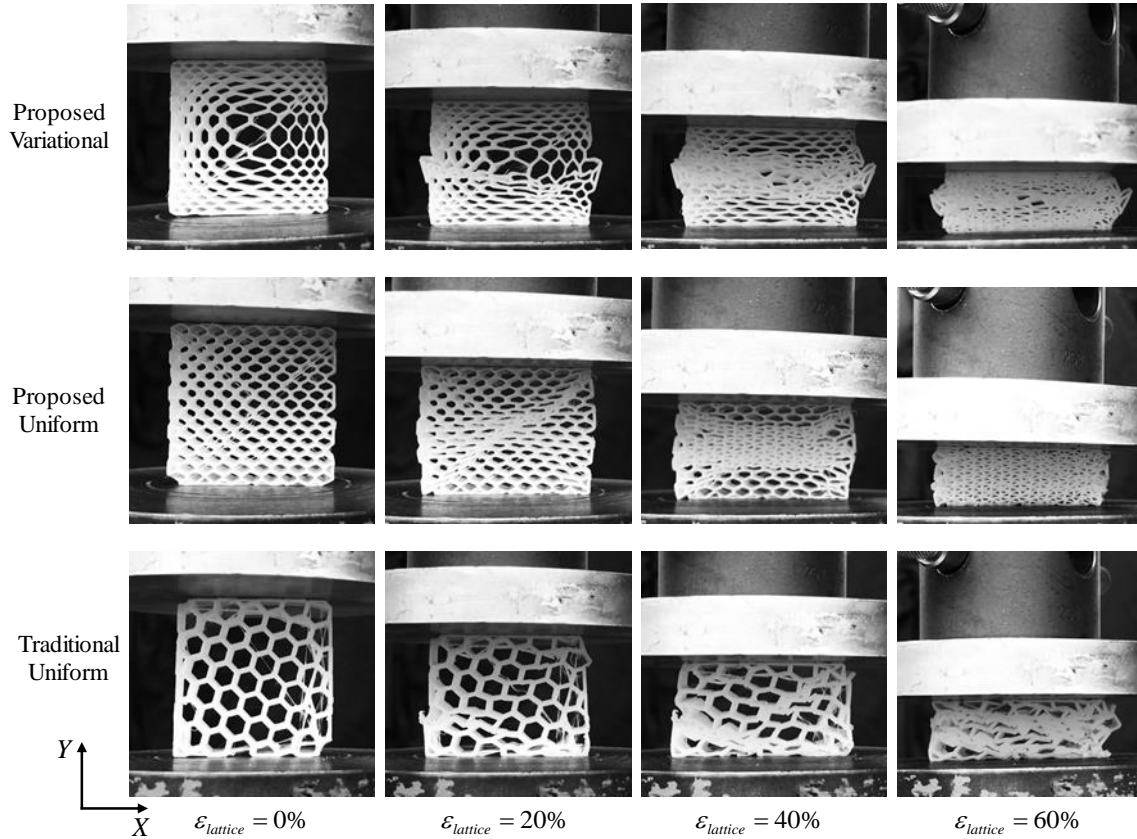


Figure 25. Compression behavior of the proposed and traditional PLA honeycombs along Y -direction.

Despite being regular hexagon, the failure of traditional honeycomb samples did not predominantly occur through either diagonal cells failure or localized deformation along mid region in both X and Y -direction loading conditions, respectively. Instead, the deformation began with buckling of cell walls and then localized with asymmetric shearing mode in more than one places throughout the structure. This happened due to the orientation of the hexagon cells in the

structure, where the cells are not aligned with the loading directions (X and Y) as shown in Figure 24 and Figure 25. Furthermore, uniform densification can be observed ($\varepsilon_{lattice} = 60\%$) in all the proposed tool-path samples compare to the traditional tool-path model. This can be attributed to the non-uniform wall thickness of the traditional honeycomb at their design phase. The thicker part of the wall segment act as reinforcement causing random densification.

The stress ($\sigma_{lattice}$) – strain ($\varepsilon_{lattice}$) behavior of the PLA honeycombs can be observed in Figure 26(a). The linear elasticity of all the samples spans over a very small strain range. The lattice elastic moduli $E_{lattice}$ are determined from this strain range and are shown in Table 4. The linear elasticity ends through plastic failure at the plastic strain $\varepsilon_{lattice}^{pl}$ giving the plastic collapse strength $\sigma_{lattice}^{pl}$. After plastic failure starts, the honeycombs show long plastic plateau regions until densification starts at the densification strain $\varepsilon_{lattice}^D$. Table 4 lists the values of the plastic collapse strengths, plastic strains, and elastic moduli of the PLA samples. It can be observed that, the proposed variational structures have the largest modulus and collapse strength along X -direction and start collapsing at the lowest strain. Also, both proposed variational and uniform structures have similar collapse strength and strain along the Y -direction. Overall, both proposed design structures (variational and uniform) demonstrate superiority in terms of strength and modulus compared to the traditional pattern structure.

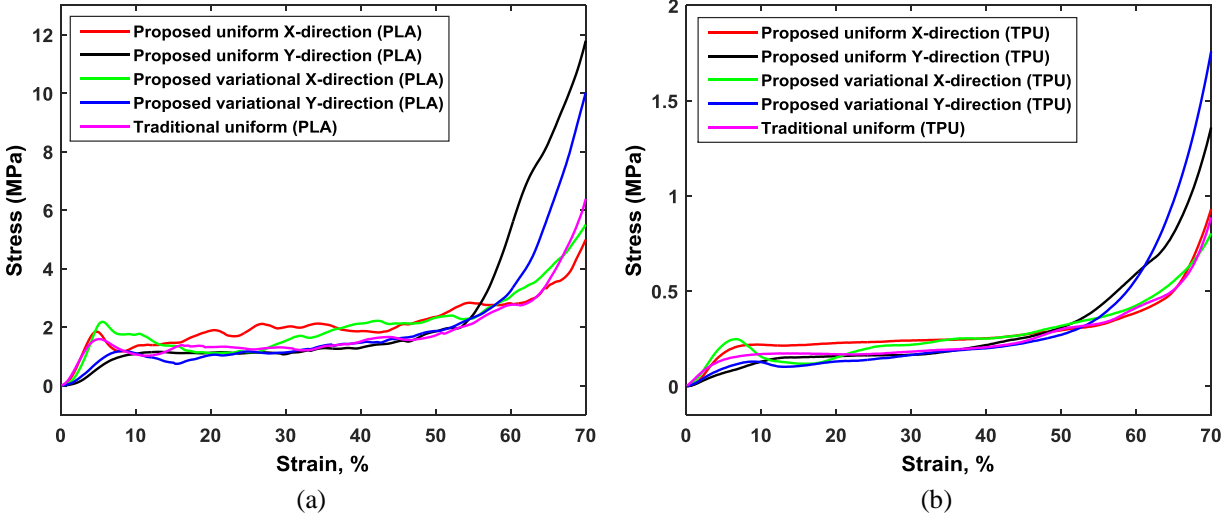


Figure 26. Lattice stress vs lattice strain curves of (a) PLA and (b) TPU honeycombs.

Table 4. Plateau stress, plateau strain, and elastic modulus PLA honeycomb lattices.

	Proposed variational		Proposed uniform		Traditional uniform
	X-direction	Y-direction	X-direction	Y-direction	
$\sigma_{lattice}^{pl}$ (MPa)	2.182	1.181	1.842	1.151	1.588
$\epsilon_{lattice}^{pl}$ (%)	5.588	8.168	4.822	13.110	5.075
$E_{lattice}$ (MPa)	0.673	0.238	0.587	0.194	0.432

It is also noticeable in Figure 26 and Table 4 that the mechanical properties of the proposed variational and uniform structures along X-direction differ from those along Y-direction. Although an identical density distribution is followed along both directions for these structures, this mechanical property variation can be attributed to the elongation of honeycomb cells along X-direction in the design (see Figure 21(d) and Figure 22(a,b)). More specifically, the elongated cells contributed to an increase in both strength and modulus along X-direction and a reduction in plastic strain. This in-plane anisotropy in the proposed structures also results in dissimilar failure processes for X and Y-direction loadings as observed in Figure 24 and Figure 25, respectively.

The compression behavior along X and Y -directions of the proposed variational and traditional honeycombs made with TPU material were also observed. Figure 27 is only showing the compression behavior of variational and traditional TPU structures under X -direction loading. Again, the failure of both variational and traditional structures predominantly occurred in the mid region of the samples. The stress ($\sigma_{lattice}$) – strain ($\varepsilon_{lattice}$) curves of the TPU honeycombs given in Figure 26(b) demonstrate that they also have low strain elastic regions followed by long plastic plateau up to the densification strain. Uniform densification is also observed in the proposed honeycomb patterns.

Table 5 lists the values of the plastic collapse strengths, plastic strains, and elastic moduli of the TPU samples. Compared to traditional honeycomb samples, the proposed variational as well as uniform TPU honeycombs have slightly higher plastic strength and elastic modulus and starts collapsing at almost similar strain level under X -direction loading. The plastic collapse strengths of variational and uniform structures are also comparable with that of traditional one along the Y -direction. Thus for TPU materials, both proposed design structures (variational and uniform) also demonstrate superiority in terms of strength and modulus compared to the traditional pattern structure.

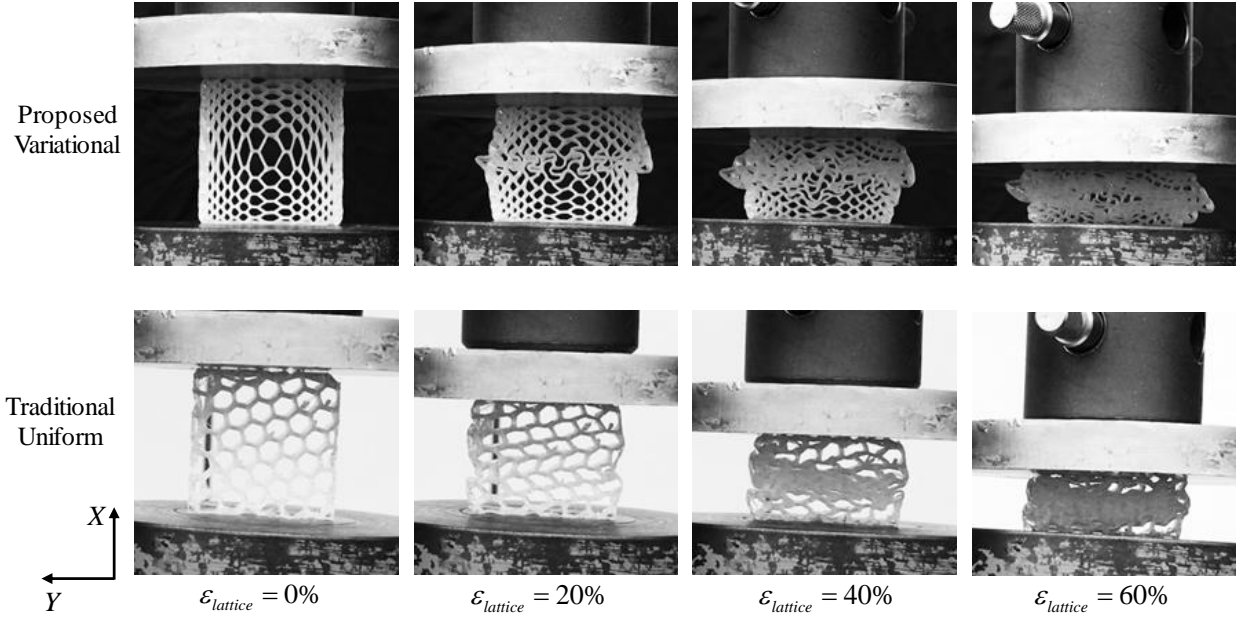


Figure 27. Compression behavior of the proposed and traditional TPU honeycombs along X-direction.

The energy absorbing capabilities of the honeycomb structures were determined through the numerical integration of the area under the stress ($\sigma_{lattice}$) – strain ($\epsilon_{lattice}$) curves. This can also be called specific energy absorbed or the cumulative energies absorbed per unit volume (E_V).

Figure 28 demonstrates the specific energies absorbed by PLA and TPU honeycombs. The strains ($\epsilon_{lattice}^D$) where densification starts and the total energies absorbed per unit volume (E_V^D) of the PLA and TPU structures were determined and are listed in Table 6 and Table 7, respectively.

The linear portions of the curves starting from the plastic strain ($\epsilon_{lattice}^{pl}$) moving to densification strain ($\epsilon_{lattice}^D$) where the specific energy is proportional to the lattice strain refers to the long plastic plateau of the honeycombs. The densification of the proposed variational and uniform honeycombs, and the traditional honeycombs started in the range of 50% ~ 60%.

At densification strain, the proposed variational and uniform PLA honeycombs absorbed approximately 34% and 69%, respectively, more energy per unit volume (E_V^D) along the X-

direction compared to that of the traditional samples. On the other hand, densifications of the proposed variational and uniform honeycombs along the Y -direction started nearly at the same strain level, but they have relatively lower (less than 14%) total specific energy absorbed (E_V^D) compared to the traditional honeycomb samples. Additionally, for both directions, uniform densification happened throughout the proposed structures at around 51% strain and above, which also led to higher strength and energy absorption capability of the proposed structures.

At densification strain, the proposed variational and uniform TPU honeycombs absorbed approximately 19% more energy per unit volume (E_V^D) along the X -direction compared to that of the traditional samples. However, densifications of the proposed variational and uniform honeycombs along the Y -direction started earlier and they have around 21% lower total specific energy absorbed (E_V^D) compared to the traditional honeycomb samples.

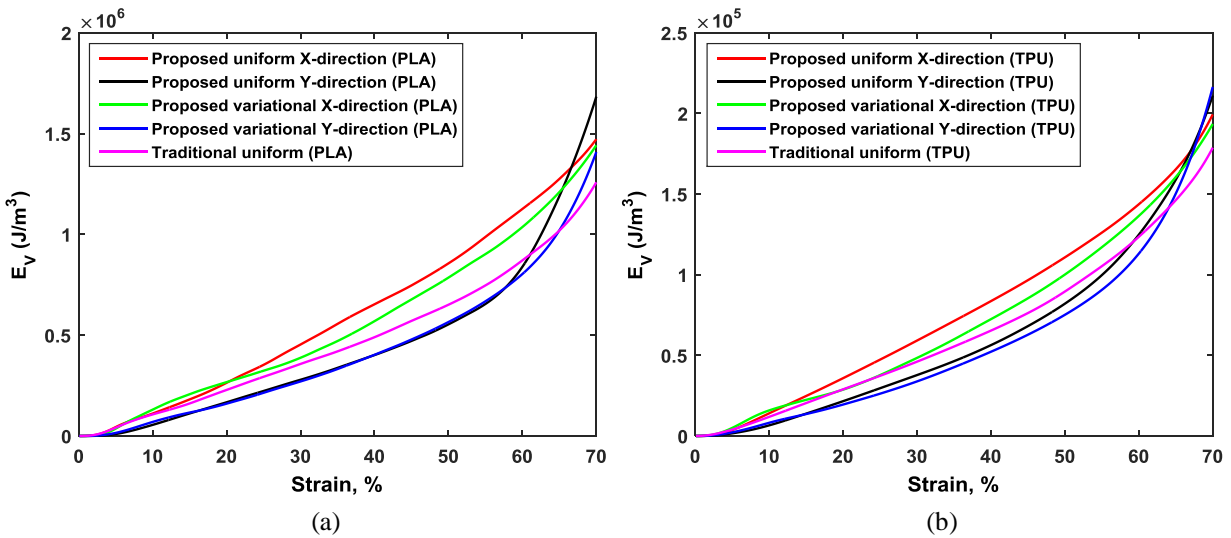


Figure 28. Specific energies absorbed by (a) PLA and (b) TPU honeycombs.

Table 5. Plateau stress, plateau strain, and elastic modulus of TPU honeycomb lattices

	Proposed variational		Proposed uniform		Traditional uniform
	X-direction	Y-direction	X-direction	Y-direction	
$\sigma_{lattice}^{pl}$ (MPa)	0.247	0.129	0.216	0.152	0.157
$\varepsilon_{lattice}^{pl}$ (%)	6.633	8.682	7.961	13.880	7.062
$E_{lattice}$ (MPa)	0.059	0.020	0.049	0.013	0.036

Table 6. Densification strains and total specific energies absorbed at densification of PLA honeycombs.

	Proposed variational		Proposed uniform		Traditional uniform
	X-direction	Y-direction	X-direction	Y-direction	
$\varepsilon_{lattice}^D$ (%)	55.00	50.68	60.31	52.94	51.1
E_V^D (J/m ³)	0.902×10 ⁶	0.578×10 ⁶	1.135×10 ⁶	0.611×10 ⁶	0.671×10 ⁶

Table 7. Densification strains and energies absorbed per unit volume at densification of TPU honeycombs.

	Proposed variational		Proposed uniform		Traditional uniform
	X-direction	Y-direction	X-direction	Y-direction	
$\varepsilon_{lattice}^D$ (%)	59.32	54.15	57.46	51.98	57.16
E_V^D (J/m ³)	1.336×10 ⁵	0.876×10 ⁵	1.343×10 ⁵	0.884×10 ⁵	1.126×10 ⁵

The proposed methodology was also applied to a free form shaped Bison model shown in Figure 29 for demonstration. The boundary contours were first obtained through slicing the model with a given slice thickness. Then following the method discussed in previous sections, the layers were voxelized and variational infill was generated. For the demonstration purpose, a tri-layer continuous toolpath generation process for a Bison layer is shown in Figure 29.

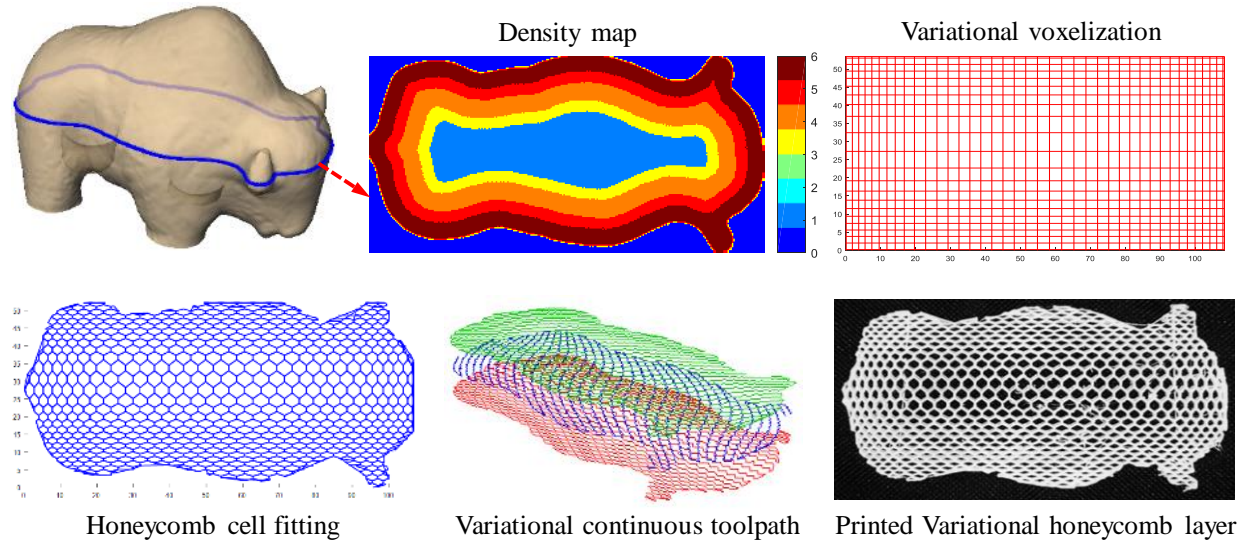


Figure 29. Variational voxelization and continuous honeycomb toolpath generated from the given density map for a layer of bison model (printed model=24 layers).

3.8. Conclusion

Continuity based toolpaths for both variational and uniform honeycomb infill structures of 3D printed objects is proposed and characterized. The proposed and traditional honeycomb infill fabrication patterns were fabricated using a commercially available 3D printer. Mechanical tests were conducted to investigate the in-plane compressive deformation behavior. The study of the deformation process reveals that the proposed honeycomb patterns possess relatively higher strength, stiffness, and total specific energy absorbed at densification along the one (X) of the two orthogonal directions on the build (XY) plane compared to the traditional equivalent relative density honeycomb infills. Overall, the mechanical properties and deformation behavior of the proposed honeycomb infills closely follow those of the traditional honeycomb infills.

Furthermore, the proposed honeycomb infill design accommodates smaller cells compared to the traditional regular hexagonal honeycomb infills for the same relative density. This feature of the infill can provide better support to the object skin resulting in enhanced surface quality. The variational honeycomb pattern introduced quite unique failure mechanism

with uniform densification which could be studied further. Thus, the controlled variational nature of the honeycomb can be utilized for very specific applications such as guided and localized energy absorption, heat transfer, acoustic wave propagation etc.

4. SHELL-INFILL CONTACT INTERFACE DESIGN WITH VARIATIONAL HONEYCOMB PATTERN

4.1. Introduction

Besides providing support to the shell/skin of the part from collapsing, infill can impact the skin surface quality. To ensure the printability and surface quality of part, the uniform density infill patterns are commonly used with higher infill density resulting in increased material usage and weight. This section proposes another design perspective for porous honeycomb infill with adaptive density gradient is proposed, where the design approach intends to provide enhanced shell-infill contact interface resulting in improved part surface quality. The gradient infill pattern can provide better skin quality yet with substantially reduced infill density. This approach can be utilized to design and manufacture light weight molds with additive manufacturing technologies where mold surface quality is deemed as a critical functional aspect.

First, the hanging skin regions that require a printing base are identified through analyzing the surface geometry. Then an adaptive density variational honeycomb infill is generated in which the infill layers that are in direct contact with the hanging skins requiring infill support are densified. The porosity of the rest of the infill layers are increased following a density gradient along the build direction in order to reduce material usage and build time. Furthermore, a novel continuity based toolpath generation scheme is proposed to minimize toolpath overlaps and increased tool air travel. The proposed adaptive density variational honeycomb infill ensures adequate support to the skin of the object while minimizing the material requirement.

4.2. Gradient Honeycomb Lattice Infill

A digital model of a part is the input for the AM processes. This model can be generated either in a computer aided design platform or through reverse engineering. In most AM systems, the *de facto* STL file format, which is a triangular mesh approximation of the object, is commonly used to digitally represent object. The surface of the object is first analyzed in order to determine the infill needed regions and then the adaptive infill is generated following the proposed methodology. This section details the algorithmic steps of the proposed methodology.

4.2.1. Object Feature Identification for Adaptive Infill

Since the foremost function of infill is to provide support to the skin/shell of the object from inside, it is necessary to identify the regions of the skin that require internal support while printing provided the object is already placed at a given build orientation. For instance, the upper part (red color) of the object skin shown in Figure 30(c) needs internal support from infill depending on the AM system. This infill support requiring region can be identified from the surface normal vectors of the object. The angle θ between the surface normal vector π and the build vector \mathbf{b} , and the resulting layer shifting distance Δ can indicate if that region of object skin need any internal support. The layer shifting distance Δ is determined by the layer staircase effect coming from slope of the surface and given layer thickness.

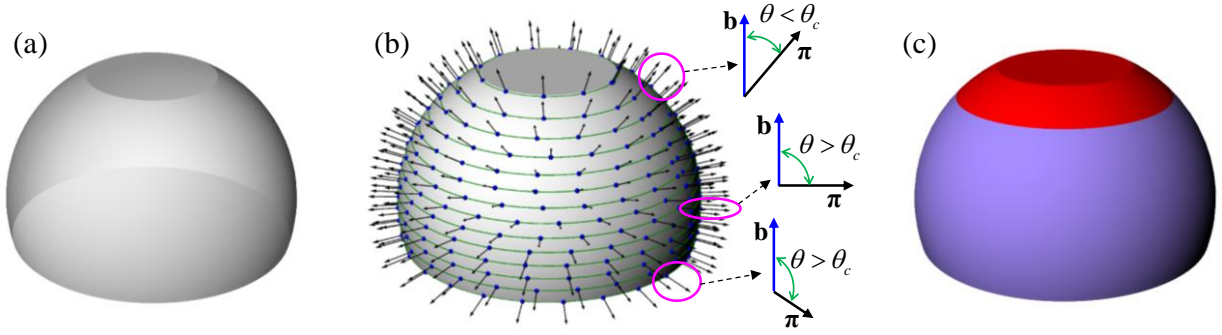


Figure 30. (a) Surface model, (b) points sampled on object surface layer boundaries and surface normal vectors, and (c) infill support required region (red).

Ideally the entire skin of the object will be supported by the infill. However, for a given build orientation, a surface point requires direct support from infill in order to be printed if the normal vector angle θ at that point is below a critical value θ_c (see Figure 30(b)). θ_c can be determined from the threshold value of shifting distance Δ_{thr} as follows: $\theta_c = \tan^{-1}(h/\Delta_{thr})$. Δ_{thr} depends on the type of AM process, material type, resolution and layer thickness, object shell thickness, and filament diameter. Thus, a dense infill needs to be generated along this region to provide printing base for the skin layers. On the other hand, the surface region in the lower part (purple color) of the object shown in Figure 30(c) with θ below the critical value does not require direct support from infill to be printed as the preceding layers will support the succeeding layers. Hence, the sparseness of infill will be maximized along this region in order to reduce the material usage and weight. Therefore, segmentizing the object skin following the above fact leads to the proposed adaptive density variational honeycomb infill.

In order to identify the object layers requiring infill support, at each layer each layer n , a finite number (M) of points $P_n = \{p_m\}_{m=1,2,\dots,M}$ are sampled on the parametric surface $S(u, v)$ of the object, where $u, v \in [0, a]$, $a \in \mathbb{R}^+$ as shown in Figure 30(b). Now each of the total N number of layers is visited from bottom to top and the surface normal vector angles, which can also be

called as slope angles, $\{\theta_m\}_{m=1,2,\dots,M}$ are determined at the sampled points $\{p_m\}_{m=1,2,\dots,M}$. θ_m at a point p_m can be calculated as $\theta_m = \cos^{-1}(\pi_m \cdot \mathbf{b}_m)$, where π_m is the unit normal vector at point p_m and \mathbf{b}_m is the build vector. Thus, visiting from bottom ($n=1$) through top layer ($n=N$), infill support needed layers are identified. For instance, if at $(n+1)^{\text{th}}$ layer, any θ_m is below θ_c , the relative density ρ_n^* of infill at n^{th} layer is set at a predefined maximum value ρ_{max}^* . This maximum density layer can be termed as a critical layer. The relative infill density of the preceding layers below the n^{th} layer gradually decreases by a gradient factor ω downward from layer to layer up to the bottom of the object, i.e., $\rho_{n-1}^* = \omega\rho_n^*$, $\rho_{n-2}^* = \omega\rho_{n-1}^*$, and so on as shown in Figure 31. The magnitude of this gradient factor ω can be changed from layer to layer along the build vector depending on the AM system and thus results in non-uniform adaptive density variation among layers.

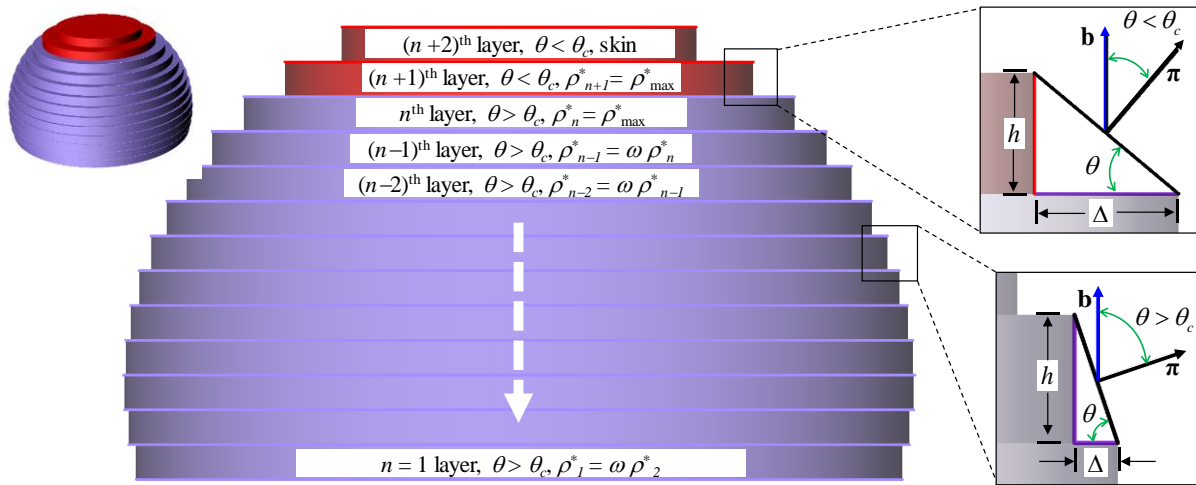


Figure 31. Layer by layer gradient infill density distribution along the build direction based on surface normal angles.

4.2.2. Continuous Honeycomb Toolpath

To generate conventional uniform density honeycomb infill, the design space can be honeycomb tessellated and extruded through the object. However, in order to generate gradient

density variational infill and reduce the toolpath overlaps and tool air travel, the continuous toolpath scheme proposed in Section 3 is used for the adaptive hexagonal honeycomb infill.

4.2.3. Intra-Layer Density Variation and Continuous Heterogeneous Infill Generation

Instead of uniform density, spatially varying infill density, which was introduced in Section 3.5, can be incorporated in each individual layers. In this process, the variational layer density can be distributed into two components along two orthogonal directions i.e., longitudinal (X -axis) and transverse (Y -axis) directions. Therefore, the longitudinal component of the spatial distribution of infill density is a continuous function of location x along X -axis such that $f_x : x \rightarrow \rho_x^*$. Similarly, the transverse component of infill density can be represented as a function of location y along Y -axis such that $f_y : y \rightarrow \rho_y^*$. For instance, the variational density in a layer can be expressed in terms of a sine function ($\sin \varphi$, where $\varphi_{\min} \leq \varphi \leq \varphi_{\max}$) with the corresponding maps, $f_x : x \rightarrow \varphi \rightarrow \rho_x^*$ and $f_y : y \rightarrow \varphi \rightarrow \rho_y^*$ along the longitudinal and transverse directions, respectively. Thus, by using the explicit function f_x and f_y , the location for individual grid can be determined across the layers along X and Y directions, respectively.. Applying these two maps, Equations (12) and (13) provide the variational density distributions along X and Y directions, respectively.

$$\rho_x^*(\varphi) = 1 - \sin \varphi, \text{ where } \varphi(x) = \varphi_{\min} + \left(\frac{x - x_{lb}}{x_{ub} - x_{lb}} \right) (\varphi_{\max} - \varphi_{\min}) \quad (12)$$

$$\rho_y^*(\varphi) = 1 - \sin \varphi, \text{ where } \varphi(y) = \varphi_{\min} + \left(\frac{y - y_{lb}}{y_{ub} - y_{lb}} \right) (\varphi_{\max} - \varphi_{\min}) \quad (13)$$

Here, x_{lb} and y_{lb} are the lower extreme values and x_{ub} and y_{ub} are the upper extreme locations of the boundary contour along X and Y directions of the layer. The domain of the

density functions, $\varphi_{\min} \leq \varphi \leq \varphi_{\max}$, needs to be carefully chosen so that the densities ρ_x^* and ρ_y^* ranges between 0 and 1. Since ‘sine’ function is used in this work, φ lies between 0° and 90° .

Figure 32(a-c) depicts an example of variational voxelization and honeycomb cell fitting for the spatial distributions of the longitudinal and transverse components of relative density following a sine function for $0.25\pi \leq \varphi \leq 0.75\pi$.

Various pre-defined functions can also be used for the longitudinal and transverse components of relative density to generate desired variation in density across the layer. Furthermore, this methodology can also be used to generate uniform density when $\rho_x^*(\varphi)$ and $\rho_y^*(\varphi)$ assume a constant function. For instance, the voxelization and honeycomb toolpath shown in Figure 32(d-f) are generated using $\rho_x^*(\varphi) = 1 - \sin(\varphi)$ and $\rho_y^*(\varphi) = 1 - \sin(\varphi)$, where $\varphi = 0.306\pi$, which gives an equivalent mean relative density of the variational toolpath shown in Figure 32.

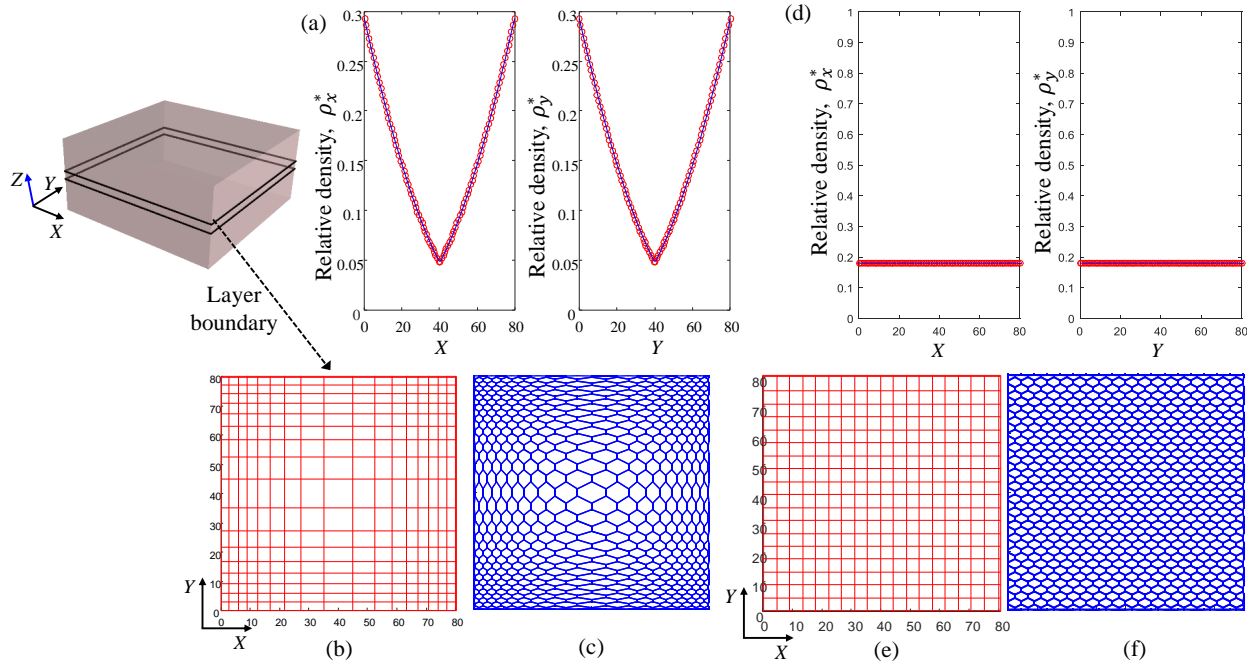


Figure 32. Function based variational density distribution of a layer: (a) spatial distribution of longitudinal and transverse variational densities, (b) non-uniform voxelization, (c) variational honeycomb cell fitting, (d) spatial distribution of longitudinal and transverse uniform densities, (e) uniform voxelization, and (f) uniform honeycomb cell fitting.

4.2.4. Maximization of Skin-Infill Contact Points

In case of the intra-layer variational voxelization, the amount of contact points between the infill and skin can be altered for the same density distribution through changing the orientation of the voxelization. For instance, Figure 33 demonstrates rotating the boundary contour for variational voxelization through $\alpha = 45^\circ$ around Z-axis (build direction) in the standard coordinate system results in a 97% increase in the number of boundary contact points compared to the uniform density honeycomb.

In this process, the boundary contour is first rotated at an angle α around the build direction (Z-axis). Then the rectilinear bounding box space of the rotated boundary contour is voxelized following the method discussed in Section 3.2 and 3.3. The bounding box of the boundary contours is represented with black broken lines in Figure 33. Once the voxelization is obtained based on the desired density map, honeycomb cells are fitted following the proposed continuous toolpath scheme discussed in Section 3.4. The honeycomb tessellation inside the bounding box space is trimmed with the boundary contour leaving the honeycomb infill with continuous toolpath. The rotation of the boundary contour is actually relative between the part and infill. Thus, infill can also be rotated and vice versa. However, a consistency in generating infill since the voxelization is performed along X and Y-axes for all cases.

A boundary contact point optimization problem is formulated by Equation (14) to determine the voxelization orientation angle α that will maximize the boundary contact points for intra-layer variational infill.

$$\begin{aligned} & \max \{ \mathbf{BContPoints} \} \\ & \text{s.t.} \\ & \alpha \in [0, \pi / 2] \end{aligned} \tag{14}$$

Here, $\{\mathbf{BContPoints}\}$ is the set of contact points between the boundary contour and voxels. These contact points are the intersecting points between the boundary contour and the voxels.

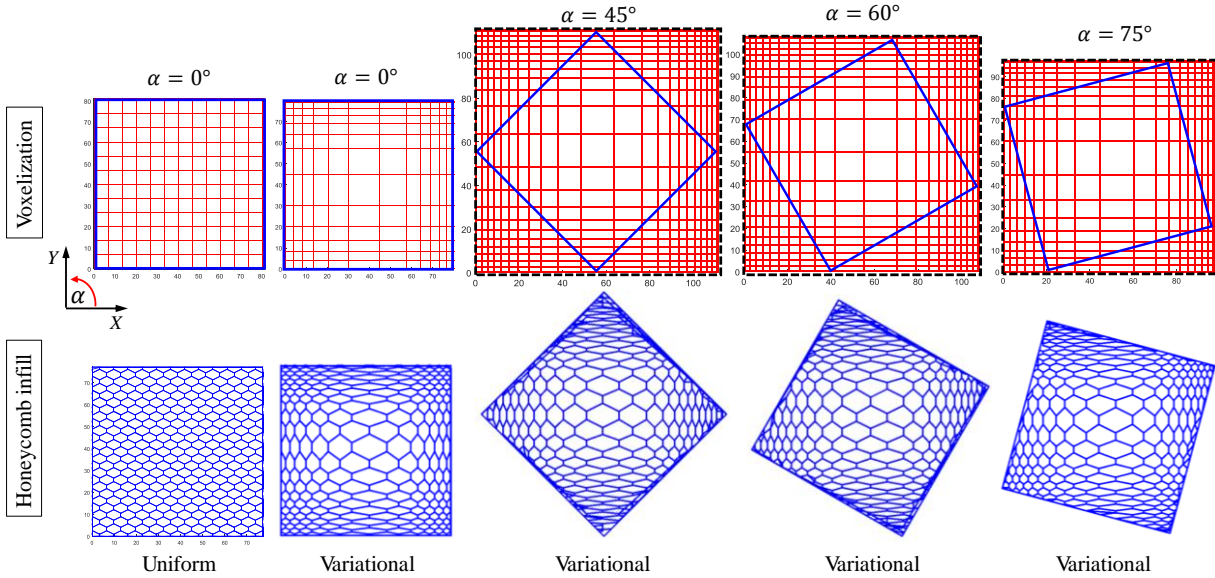


Figure 33. Changing boundary contact points through rotating the boundary contour for variational voxelization.

4.3. Results and Discussion

4.3.1. Adaptive Density Honeycomb Infill

The proposed methodology for Interlayer variational honeycomb infill was implemented with visual basic based scripting language. The algorithm runs were performed on an Intel Core i7 @3.4 GHz CPU equipped with 12 GB RAM. The methodology was evaluated on the example object in Figure 34. The generated continuous honeycomb toolpaths were printed with Monoprice Maker Select v2 3D-Printers using PLA material. The layer thickness was used as 0.2 mm.

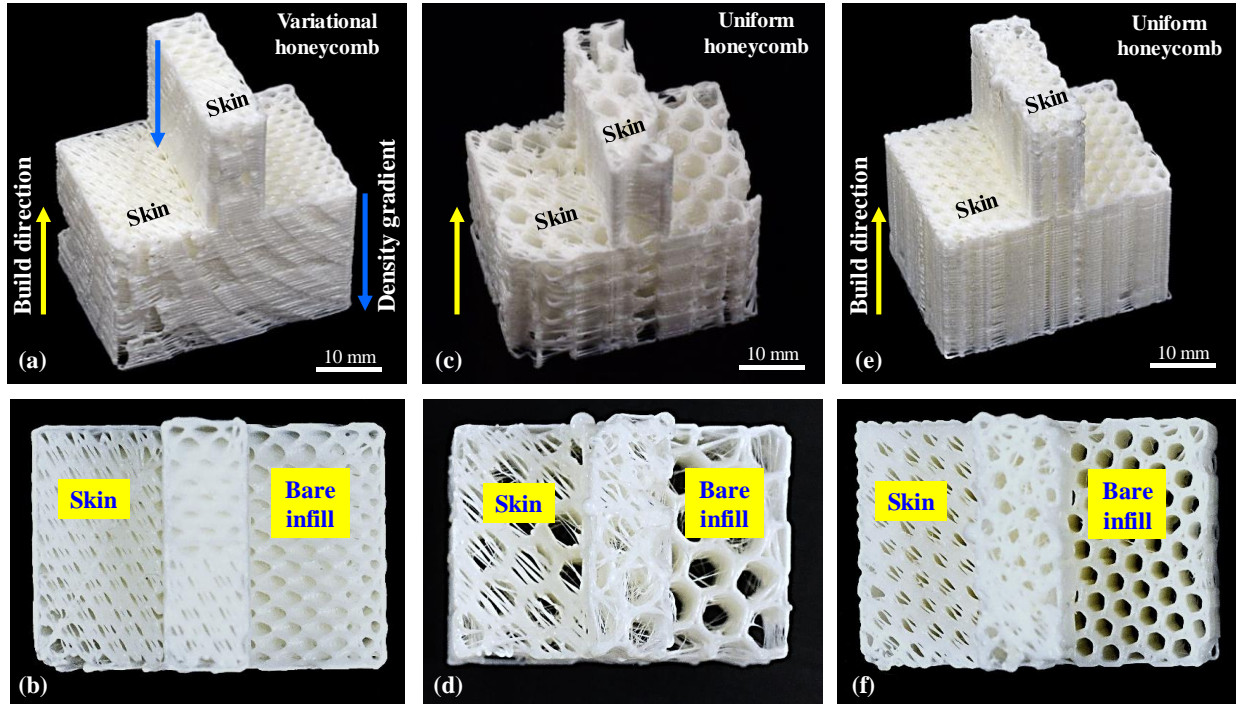


Figure 34. (a) Proposed adaptive density variational honeycomb infill, (b) parts of the overhanging skin printed on the proposed infill, (c) uniform honeycomb infill with low density, (d) parts of the overhanging skin printed on the uniform honeycomb infill with low density, (e) uniform honeycomb infill with high density, and (d) parts of the overhanging skin printed on the uniform honeycomb infill with high density.

The proposed adaptive density variational honeycomb infill is fabricated for an example part with volume of 27255 mm^3 as shown in Figure 34(a). The interlayer gradient density is generated along the build direction of the part. The overall relative density of this variational infill is 28%. The proposed infill is compared with the following two infills: Comparable-1 being a uniform honeycomb infill with low density (24%) shown in Figure 34(c) and Comparable-2 being a uniform honeycomb infill with high density (44%) shown in Figure 34(f).

Figure 34(b, d, f) demonstrate the top views of the partial overhanging skins printed on the proposed and the two comparable infills, respectively. It is clearly observed that the adaptive density variational honeycomb infill substantially improves the skin surface quality compared to the uniform honeycomb infill with both low (Comparable-1) and high density (Comparable-2).

Particularly, Comparable-1 infill results in an unacceptable surface quality of the skin for the relative density approximately equivalent to the proposed infill. On the other hand, when density is raised from 28% to 44% with smaller hexagon cell type, the Comparable-2 infill yields skin quality similar to that of the proposed infill. Therefore, the proposed methodology reduces approximately 38% material usage for a comparable or even better skin surface quality of the example part. Table 8 summarizes the comparative advantages of the adaptive density variational honeycomb infill.

Table 8. Comparison among the proposed variational and existing uniform honeycomb infills

Part Infill Type	Relative Density	Generated skin type	Material weight (gm)	Weight saving with respect to Comparable-2
Proposed adaptive density variational honeycomb infill	28%	Good	8.279	38%
Comparable-1: Uniform honeycomb infill with low density	24%	Bad	7.134	46%
Comparable-2: Uniform honeycomb infill with high density	44%	Fair	13.315	–

4.3.2. Boundary Contact Points Increase through Intra-Layer Density Variation

In order to maximize the boundary contact points, Equation (7) was solved through rotating the layer boundary contours at a uniform interval of 15° over the limits ($0 \sim \pi/2$) of voxelization orientation angle α . For each orientation, the layer is voxelized and the boundary contact points are determined from the intersections between the contour and voxels. For the square block part, it is found that the 45° orientation yields a significant increase (97%) in the boundary contact points compared to a uniform honeycomb (see Table 9). It should be mentioned that, there is slight deviation in material density between the uniform and variational model and the deviation was kept within $\pm 5\%$ in the following figures.

Table 9. Percentage increase in the number of boundary contact points for different voxelization orientation of the square block.

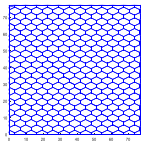
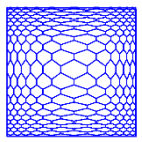
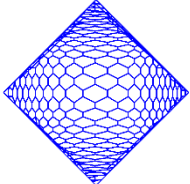
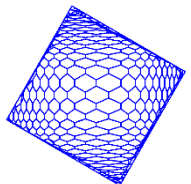
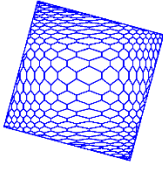
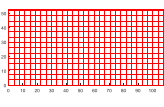
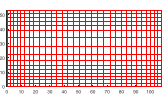
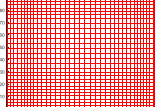
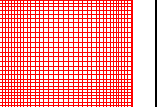
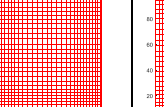
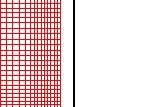

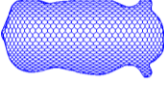


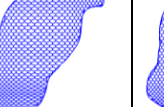
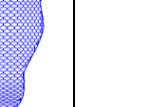
23% overall relative density					
Honeycomb infill					
α	0° (uniform)	0°	45°	60°	75°
% increase in contact points	–	0%	97%	79%	58%

Table 10. Percentage increase in the number of boundary contact points for different voxelization orientation of the bison model layer given in Figure 29.

39% overall relative density						
Voxelization						
Honeycomb infill						
α	0° (uniform)	0°	30°	45°	60°	75°
% increase in contact points	–	8%	13%	18%	22%	21%

However, the increase in boundary contact point also depends on the contour geometry. Hence, the proposed methodology is applied to a free form shaped Bison model shown in Figure 29 (Section 3.7). The boundary contours are first obtained through slicing the model with a given slice thickness. Then following the method discussed in Section 3.3, the layers are voxelized and both uniform and variational infills are generated. It is found that compared to a uniform

honeycomb, the maximum possible contact point increase for a layer of Bison model given in Figure 29 is 22% at 60° orientation (see Table 10).

4.4. Conclusion

In additive manufacturing, porous infills are sometimes used to reduce the material usage and part weight. However, increased porosity can impair surface quality of the part skins due to poor printing supports for the skins. An interlayer gradient density porous honeycomb infill structure is proposed to provide better printing support for the overhanging skins of parts. The infill layers which are in direct contact with the skins requiring printing support as infill. Those skin region are densified and the density of the preceding layers are gradually reduced to decrease the part weight. Furthermore, a continuous toolpath scheme for the gradient density porous honeycomb structure is proposed to reduce tool start-stops, and air travels.

Implementation results demonstrate that the proposed approach can significantly reduce the part weight compared to the conventional uniform honeycomb without compromising the surface quality of part skin. In addition to the interlayer density variation, incorporating intra-layer density gradient is expected to further reduce the part weight.

Furthermore, the proposed honeycomb pattern accommodates smaller cells compared to the existing regular hexagonal honeycomb infills for the same relative density. This feature of the infill can provide better support to the object skin resulting in enhanced surface quality. This proposed method does not eliminate the problem of trimmed unit cells at the boundaries (due to the voxels still being quadrilateral after the density is varied), but attempts to relieve the reduction in strength by varying the density. Overall, the proposed density controlled design and fabrication for porous structures is found promising for functionality driven applications such as

guided and localized energy absorption, varying mechanical strength, heat transfer, fluid transfer, acoustic wave propagation etc.

The gradient porosity across the object may shift the original center of gravity of the object, which may affect the stability or self-balance of the object. However, the proposed structural patterns are highly porous and thus light weight. Hence, the variational nature of such structures will not have significant contribution to shifting the center of gravity of the object.

5. HETEROGENEOUS TOPOLOGY DESIGN FOR ENGINEERED TISSUE SCAFFOLDS

5.1. Introduction

Porous scaffold structures have great potential to be used as a guiding substrate for three-dimensional (3D) tissue regeneration processes. The interaction between the cells and the scaffold constitutes a dynamic regulatory system for directing tissue formation as well as regeneration in response to injury [166]. A successful interaction must facilitate the cell survival rate by cell migration, proliferation and differentiation, waste removal, and vascularization while regulating bulk degradation, inflammatory response, pH level, denaturation of proteins, and carcinogenesis affect [143]. Inducing an amenable bio-reactor and stimulating the tissue regeneration processes while minimally upsetting the delicate equilibrium of the cellular microenvironment is the fundamental expectation of a functional tissue scaffold [167].

Achieving the conflicting multi-functinality through the scaffold structure will depend upon the *troika* factor, i.e., material, manufacturing processes, and its structure. However, most of these design techniques create complex scaffold architecture with little or no consideration of continuity and connectivity between neighboring unit cell. Moreover, seamless data corridor between design (virtual) and manufacturing (physical) is often ignored which is necessary for the manufacturability of the constructed heterogeneous architecture. The focus of this research is on designing the variational/heterogeneous scaffold structure mimicking the native tissue/organ architecture and direct fabricating the structure without the use of any CAD model.

In this Section, the bio-additive manufacturing process is divided into pre-processing, processing and post-processing stage as shown in Figure 35. The main contribution is emphasized on the pre-processing and processing stage that deals with the design representation

and the actual bio-printing. A topology based design methodology is proposed to accurately represent the heterogeneous internal architecture of tissues/organs. An image analysis technique is used that digitizes the data from bio-medical image. A weighted topology reconstruction algorithm is implemented to analyze the extrinsic property of the target area. The internal heterogeneity is then represented with parametric functions which will be used for mapping the spatial material distribution across the structure. The generated information is directly transferred to the bio-printer and STL-free heterogeneous porous scaffold structure is manufactured. The roadmap of the proposed bio-printing process is demonstrated in Figure 35.

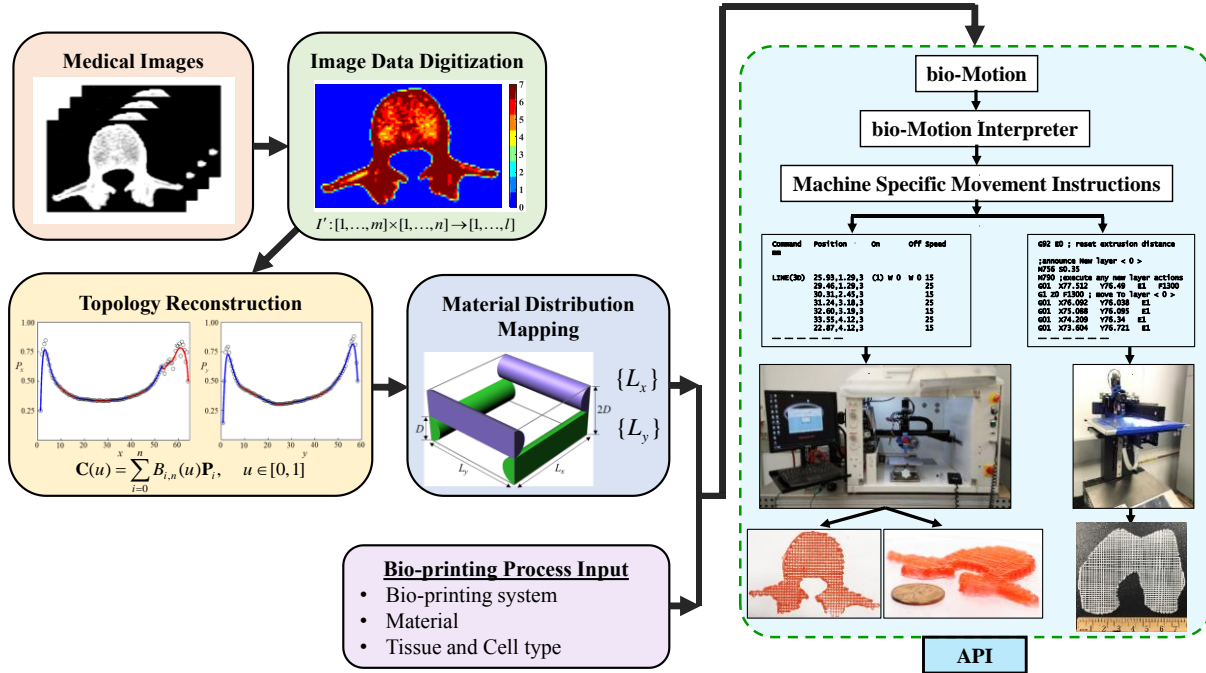


Figure 35. Proposed direct bio-printing process roadmap

5.2. Methodology

5.2.1. Pre-processing stage

The microstructures of tissues and organs are heterogeneous which provides multi-functionality such as mechanical, chemical, and biological. Medical images obtained from non-

invasive imaging techniques, such as Computed Tomography (CT)/micro-CT/high-resolution peripheral QCT, Magnetic Resonance Imaging (MRI), or Dual-Energy X-Ray Absorptiometry (DEXA) images, can be analyzed to model the internal microstructural heterogeneity of the tissue/organ. For example, Hazrati *et. al.* [168-171] determined bone volume fraction (BV/TV) and other bone microstructural parameters including trabecular thickness, trabecular number, trabecular spacing, structural model index, bone anisotropy etc. from bone medical images using a combination of mesh morphing and element mapping approaches. The bone volume fraction (BV/TV) map [171], which is a measure of bone material density distribution, obtained from a CT image of the proximal portion of a femur is shown in Figure 36(b). However, the output is not suitable for 3D bio-printing process. Hence, a novel framework developed where the internal heterogeneity information of a tissue/organ is captured in a set of parametric function from its medical images. The information is then stored in a hierarchical data structure and processed through an application program interface (API) for direct 3D bio-print mimicking tissue internal architecture.

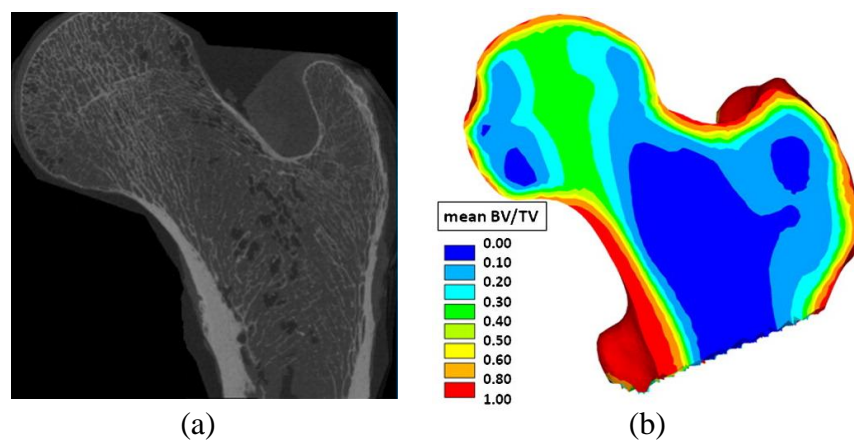


Figure 36. (a) Proximal femur (midcoronal plane) CT image and (b) bone volume fraction (BV/TV) [171]

5.2.2. Medical Image Data Digitization

Medical images of various modality (i.e., CT, MRI, DEXA, etc.) is the input in the proposed methodology. For the purpose of demonstration, a high resolution peripheral QCT image of human distal tibia [172] shown in Figure 37(a) was used. The medical image of tibia is, in fact, a rectangular array of pixels $\mathbf{P}_{x,y} = [P_{x,y}]$, where $P_{x,y}$ is the intensity value of a pixel at spatial location (x, y) . The pixel values $P_{x,y}$ may vary spatially and are mapped as a function of x and y values. Thus, the tibia image can be represented as a single valued function $I : [1, \dots, M] \times [1, \dots, N] \rightarrow \mathfrak{R}$, where M and N are the pixel numbers along X and Y directions, respectively.

The pixel intensity values of image I were discretized through image quantization. In this process, image I was transformed into $I' : [1, \dots, M] \times [1, \dots, N] \rightarrow [1, \dots, l]$ taking only a discrete finite set of pixel values defined as quantization levels (l). Image Quantization was performed to consolidate the continuous pixel values into finite discrete levels so that the pixels having intensity values closer to each other could be identified. This process resulted in a set of discrete iso-intensity value regions as shown in Figure 37. The iso-intensity pixel value region in an image is assumed to possess approximately same microstructural heterogeneity.

The 2D image domain is then decomposed along longitudinal (X-axis) and transverse (Y-axis) direction. Normalized average pixel values $\bar{P}_x = \frac{1}{N_y} \sum_y \left(\frac{P'_{x,y}}{l-1} \right)$ and $\bar{P}_y = \frac{1}{N_x} \sum_x \left(\frac{P'_{x,y}}{l-1} \right)$ of the quantized image I' were determined along both longitudinal (X) and transverse (Y) directions, which are plotted as shown in Figure 38. The normalized average pixel values \bar{P}_x and

\bar{P}_y are treated as the spatial relative material density. Hence the spatial porosity distribution will be $(1-\bar{P}_x)$ and $(1-\bar{P}_y)$ along longitudinal and transverse directions, respectively.

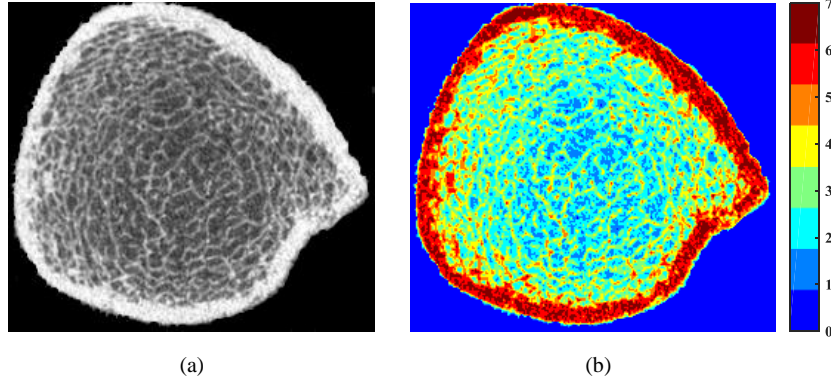


Figure 37. (a) High resolution peripheral QCT (HR-pQCT) image of human distal tibia [172] and (b) corresponding quantized image I'

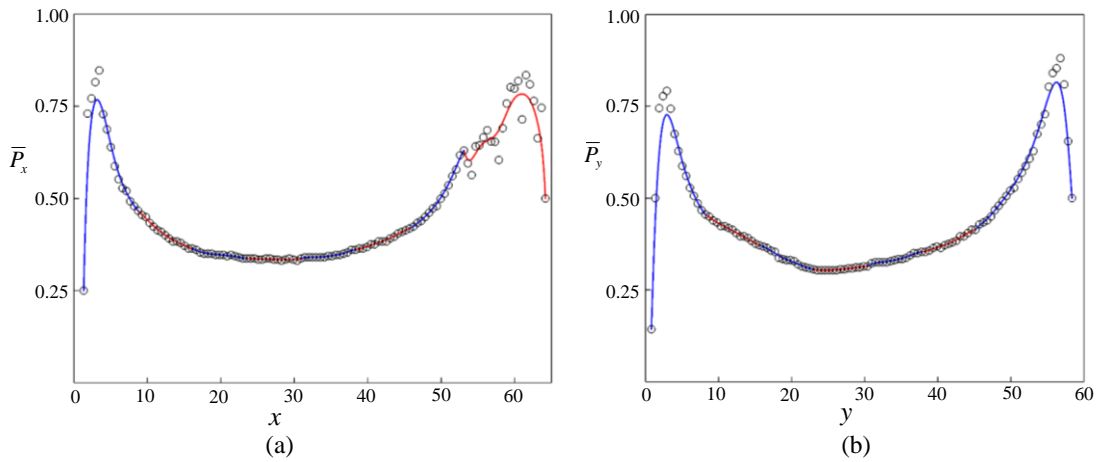


Figure 38. Normalized average pixel value as a function of pixel location along (a) longitudinal direction and (b) transverse direction and corresponding segmented Bézier curve fitting.

5.2.3. Topology Reconstruction with Parametric Function

The resulting plotted density $\bar{\mathbf{P}}_x = \{\bar{P}_x\}$ and $\bar{\mathbf{P}}_y = \{\bar{P}_y\}$ points will be used to fit parametric curves that will represent the topology of the domain. Adaptively segmented but connected parametric polynomial B-spline curves $\{C(u)\}$ are fitted to correlate the average pixel values

with spatial locations. The B-spline curve is a generalization of the Bézier curve, i.e., Bézier curve is a B-spline with no interior knots [173]. A Bézier curve of degree n is given by Equation (15) where $\{B_{i,n}(u)\}$ is the n^{th} degree Bernstein polynomials.

$$\mathbf{C}(u) = \sum_{i=0}^n B_{i,n}(u) \mathbf{P}_i, \quad u \in [0, 1] \quad (15)$$

where, $B_{i,n}(u) = \frac{n!}{i!(n-i)!} u^i (1-u)^{n-i}$

Here, $\{\mathbf{P}_i\}_{i=0,\dots,n}$ are the control points of the Bézier curve $\mathbf{C}(u)$. In this work, the control points of the Bézier curve are defined by the ordered pairs of pixel location and pixel value (density), $\{\mathbf{P}_i = (x, \bar{P}_x)_i\}$. In order to capture the correlation between the pixel values and pixel locations along X direction, the data points $\mathbf{XP} = \{(x, \bar{P}_x)_j : j=0,1,\dots,(N-1)\}$ are adaptively segmented. First, an initial control point segment is formed by taking a subset $\mathbf{SXP}_{g=0} \subseteq \mathbf{XP}$ having a given cardinality $s := n + 1$. Thus the initial segment can be defined as $\mathbf{XP} \supseteq \mathbf{SXP}_{g=0} = \{(x, \bar{P}_x)_j : (x, \bar{P}_x)_j \in \mathbf{XP}, j = ng, \dots, n(g+1)\}$. Then, an n^{th} -degree Bézier curve $\mathbf{C}(u)_g^x$ is fitted for this segment containing $n+1$ number of control points and the curve fitting error is evaluated using Equation (16).

$$E = \left(\frac{1}{n+1} \right) \sum_{i=0}^n \| (x, \bar{P}_x)_i - C(u_i) \|^2 \quad (16)$$

Equation (16) determines the average of the squared Euclidean distance between the control point and its corresponding point on the fitted curve. Thus, E measures the average of the total accumulation of squared distances in the segment.

Based on the value of E , the adaptive segmentation is performed. In the adaptive segmentation, the value of E is compared to a given threshold value E_{thr} . If E becomes greater than E_{thr} , the next segment of cardinality $n+1$ is formed as

$\mathbf{XP} \supseteq \mathbf{SXP}_{g=1} = \{(x, \bar{P}_x)_j : (x, \bar{P}_x)_j \in \mathbf{XP}, j = ng, \dots, n(g+1)\}$ and a n^{th} -degree Bézier curve $\mathbf{C}(u)_g^x$ is fitted. Note that the last point of g^{th} segment (\mathbf{SXP}_g) is the first point of $(g+1)^{\text{th}}$ segment (\mathbf{SXP}_{g+1}), thereby ensuring the connectivity between the Bézier curves.

However, if E is smaller than E_{thr} , instead of forming a new segment, the initial segment is updated by appending the immediate next t number of points from \mathbf{XP} to $\mathbf{SXP}_{g=0}$.

The updated segment becomes

$\mathbf{SXP}'_{g=0} = \mathbf{SXP}_{g=0} \cup \{(x, \bar{P}_x)_k : (x, \bar{P}_x)_k \in \mathbf{XP}, k = n(g+1)+1, \dots, n(g+1)+t, t \leq n+1\}$. Again a new $(n+t)^{\text{th}}$ -degree Bézier curve $\mathbf{C}(u)_g^x$ is fitted for updated initial segment containing $n+t$ number of control points and the curve fitting error is evaluated using Equation (16). This process is repeated until all the points in \mathbf{XP} are visited, resulting in a set of Bézier curves $\{\mathbf{C}(u)^x\}$. The pseudo-code for the entire process is given by Algorithm 1 shown in Figure 39.

Similarly, another set of Bézier curves $\{\mathbf{C}(u)^y\}$ is fitted through the control points $\mathbf{YP} = \{(y, \bar{P}_y)_k : k = 0, 1, \dots, (M-1)\}$ to capture the correlation between the pixel values and pixel locations along Y direction. Figure 38 demonstrates the \bar{P}_x vs. X and \bar{P}_y vs. Y scatter plot with Bézier curve fitting in two orthogonal directions, respectively, for the tibia. These segmented parametric functions represent the spatial topology information for the scaffold internal architecture.

Algorithm 1: FitParametricCurve

Input : Control points $\mathbf{XP} = \{(x, P_x)\}$, error threshold E_{thr} , initial segment size s .

Output: Set of fitted parametric curves $\mathbf{C} = \{\mathbf{C}(u)^x\}$.

```
1  $\mathbf{C} \leftarrow \emptyset$ ;  
2  $\mathbf{SXP} \leftarrow \emptyset$ ;  
3  $\mathbf{Q} \leftarrow \emptyset$ ;  
4  $\overline{\mathbf{Q}} \leftarrow \mathbf{XP}$ ;  
5  $u \in [0, 1]$ ;  
6 while  $|Q| < |XP|$  do  
7    $\mathbf{SXP} \leftarrow \{(x, P_x)_j : (x, P_x)_j \in \overline{\mathbf{Q}}, j = 1, \dots, s - 1\}$ ;  
8    $\mathbf{C}(u)^x \leftarrow \sum B(u)\mathbf{SXP}$ ;  
9    $E \leftarrow Error(\mathbf{SXP}, \mathbf{C}(u)^x)$ ;  
10   $\mathbf{Q} \leftarrow \mathbf{Q} \cup \mathbf{SXP}$ ;  
11   $\overline{\mathbf{Q}} \leftarrow \overline{\mathbf{Q}} \setminus \mathbf{SXP}$ ;  
12  while  $E < E_{thr}$  and  $|Q| < |XP|$  do  
13     $\mathbf{SXP} \leftarrow \mathbf{SXP} \cup \{(x, P_x)_j : (x, P_x)_j \in \overline{\mathbf{Q}}, j = 1, \dots, s - 1\}$ ;  
14     $\mathbf{C}(u)^x \leftarrow \sum B(u)\mathbf{SXP}$ ;  
15     $E \leftarrow Error(\mathbf{SXP}, \mathbf{C}(u)^x)$ ;  
16     $\mathbf{Q} \leftarrow \mathbf{Q} \cup \mathbf{SXP}$ ;  
17     $\overline{\mathbf{Q}} \leftarrow \overline{\mathbf{Q}} \setminus \mathbf{SXP}$ ;  
18  end  
19   $\mathbf{C} \leftarrow \mathbf{C} \cup \mathbf{C}(u)^x$ ;  
20 end  
21 return  $\mathbf{C}$ 
```

Figure 39. Parametric curve fitting algorithm (Algorithm 1).

5.2.4. Material Mapping with Generated Functions

The topology information extracted in the previous section needs to be converted into bio-printing process plan information. A layer-by-layer material deposition plan is implemented using the parametric functions derived in Section 5.2.3. In order to achieve the porous internal architecture, the scaffold internal structures are fabricated by depositing cylindrical micro-filaments parallel to each other in every layer using a certain lay-down pattern with orientation angle θ as shown in Figure 40. Here, the orientation angle θ defines the angle between the filaments of two consecutive layers.

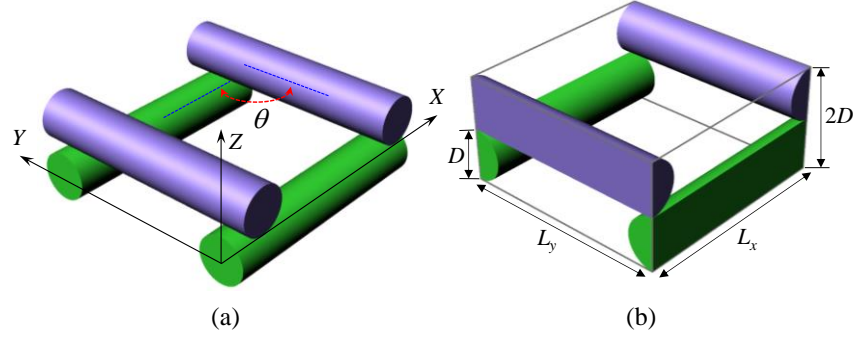


Figure 40. Unit cell representation: (a) a segment of a bi-layer and (b) a unit cell

The porosity of the internal architecture is computed using a unit cell representation [143] shown in Figure 40. The unit cell is the repetitive element across the entire structure. It is assumed that the height of the unit cell is twice the layer thickness resulting in a bi-layer representation. Thus, in the unit cell, the filaments of one layer make an angle θ with the filaments of the other layer. The porosity of a unit cell can be defined based on the ratio of void space volume to the total volume of the unit cell. Considering a given zigzag laying pattern and a filament diameter D , the filament spacing can be determined using Equation (17).

$$L = \frac{\pi D \left(1 + \frac{1}{\sin \theta}\right)}{8(1-p)} \quad (17)$$

Here, L is the space between filaments and θ is the consecutive layer filament orientation angle. For 0° – 90° zigzag filament laying pattern, θ will be 90° . Since the normalized average pixel values \bar{P}_x and \bar{P}_y are considered as the relative density, the porosity p in Equation (17) can substituted with $(1 - \bar{P}_x)$ and $(1 - \bar{P}_y)$ to determine filament spacing L_x and L_y , respectively.

In order to determine the variational filament spacing $\{L_x\}$ along X direction, at the beginning when $x = 0$, $\hat{P}_{x=0}$ was predicted from the fitted Bézier curves $\{C(u)^x\}$. Then the

predicted pixel value $\hat{P}_{x=0}$ was fed into Equation (18) to determine the spacing ($L_{x=0}$) between first and second filaments. Next, the value of x was updated to $L_{x=0}$. \hat{P}_x was again predicted using $\{\mathbf{C}(u)^x\}$ and the spacing between second and third filaments were determined from Equation (17). This process was repeated until the entire layer was covered. Algorithm 2 shown in Figure 41 gives the pseudo-code for determining filament spacing along X direction. Similarly, the variational filament spacing $\{L_y\}$ along Y direction were also determined using $\{\mathbf{C}(u)^y\}$. Therefore, Equation (17) can be reduced to Equation (18) in order to determine the effective porosity of a unit cell when $\theta = 90^\circ$.

$$p = 1 - \frac{\pi D(L_x + L_y)}{8L_x L_y} \quad (18)$$

Algorithm 2: DetermineFilamentSpacingAlongX

Input : filament radius r , $\{\mathbf{C}(u)^x\}$, external contour bottom-left extreme point (X_{min}, Y_{min}) , external contour bottom-right extreme point (X_{max}, Y_{min}) .

Output: Set of filament spacings along X direction.

```

1  $L_x \leftarrow \emptyset$ ;
2  $x \leftarrow 0$ ;
3 while  $x < \|(X_{max}, Y_{min}) - (X_{min}, Y_{min})\|$  do
4    $\hat{P}_x \leftarrow \{\mathbf{C}(u)^x\}$ ;
5    $l_x \leftarrow \pi r / 2(\hat{P}_x)$ ; //filament spacing
6    $L_x \leftarrow L_x \cup \{l_x\}$ ;
7    $x \leftarrow x + l_x$ ;
8 end
9 return  $L_x$ 

```

Figure 41. Variational tool-path generation algorithm (Algorithm 2).

The outcome of the above algorithms will generate a set of sequential tool-path points for the corresponding image-layer. The chronological bottom-up or top-down visit to each layer of the object will result in sequential tool-path points for the targeted 3D scaffolds. Once all the sequential points are determined, the information is stored in a hierarchical order as a generic

digital file format [174] as shown in Figure 42. To construct the heterogeneous topology in the scaffold with any bio-additive manufacturing equipment, the digital structured data needs to be converted into the controller specific language. A common API (Application Program Interface) platform is also proposed, which can access and generate machine readable file for different existing bio-printers. The metadata section of the file will assure the readability by different existing bio-printing interpreters.

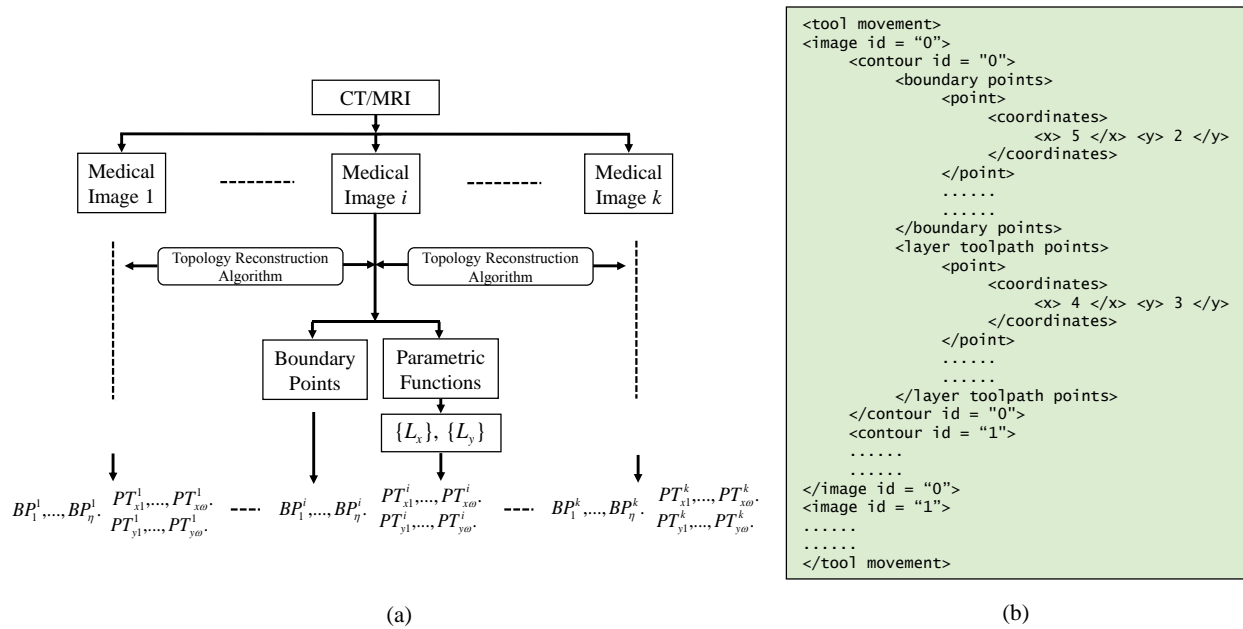


Figure 42. (a) Hierarchical data structure and (b) tool movement data storage file format (bio-Motion) for direct bio-printing.

5.3. Processing/Bio-printing

An extrusion-based, bio-compatible, layered fabrication system has been designed and developed in to deposit both engineering materials as well as delicate biomaterials with 5 μm spatial resolution. The in-house 3D micro-nozzle biomaterial deposition system (see Figure 43) has been used to fabricate 3D scaffold structure with sodium alginate and cellulose based hybrid hydrogel bio-ink and CaCl_2 solution as the “cross-linker”. Sodium alginate, a type of hydrogel

widely used in cell immobilization, cell transplantation, and tissue engineering, is preferred as biomaterial due to its biocompatibility and formability [141, 143, 167]. The bio-ink will be filled in a reservoir, and a pneumatic system will be deployed to flow the solution via the micronozzles (100-250 μm). The system will operate at room temperature under low pressure (0-8 psi). The calcium chloride solution will be dispensed onto printed sodium alginate structure through a second nozzle to provide cross-linking between the alginate anions and the calcium cations to form the hydrogel.



Figure 43. Micro-nozzle bio-additive material deposition system.

5.4. Implementation

In this study, de-identified CT scan stack of images of vertebra collected from the department of radiology, Sanford health clinic, Fargo, North Dakota was used as the first example. Because tissue/organ microstructural heterogeneity is modeled for bio-additive manufacturing, the CT scan sequential image slices were used to generate the layer geometries. The heterogeneity information in each layer is extracted from the CT scan through image analysis which is discussed in the following section. For the second example, an XtremeCT II image [175] of human distal femur shown in Figure 48(a) was used.

The heterogeneous porosity of each layer of vertebra was modeled from the CT scan sequential images slices as discussed in Sections 5.2. Figure 44 shows the quantized images of two vertebra slices and Figure 45 shows the parametric curve fitting to the image information of both vertebra slices.

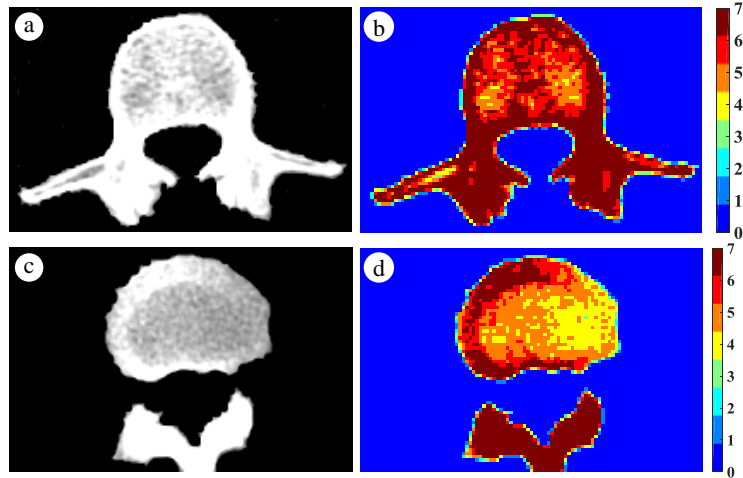


Figure 44. (a) First and (c) fourth images among the stack of four CT images of human vertebra and (b, d) corresponding quantized images, respectively, at $l = 8$.

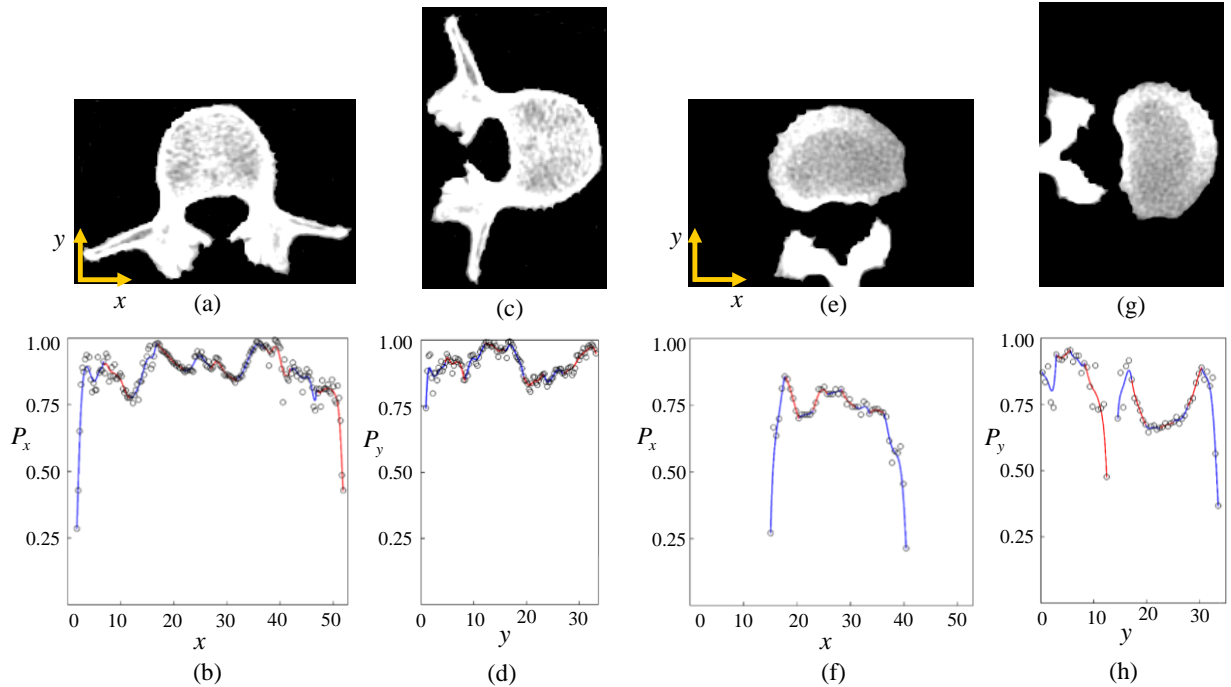


Figure 45. Two corresponding orthogonal parametric topology functions generated from first (a-d) and fourth (e-h) vertebra images (The image and functions are represented in the same scale).

Once the parametric Bézier curves were fitted to map the internal architectural property of vertebra, the unit cell based layer by layer filament deposition toolpath was generated to achieve the porous heterogeneous structure of the vertebra model. A heterogeneous/variational porosity toolpath for the first slice of the vertebra structure is shown in Figure 46(a). Although the variational porosity across the design shown in Figure 46(a) is not clearly visible, its variational porosity distribution can be observed by its porosity map shown in Figure 46(b). To examine the effectiveness of the proposed methodology, we compared the designed heterogeneous structures with a conventional uniform porous structure. The uniform porous structure design has the overall average porosity of the first vertebra slice. Five corresponding cells were randomly chosen from both heterogeneous and uniform designs and the porosity values were calculated. The calculated porosity values of both designs were compared with the real porosity obtained from the image data digitization. Table 11 gives the percentage error of porosity between the proposed design and real image as well as the uniform design with real image. The overall error will depend upon the layer image and porosity distribution. Larger porosity variation within the layer will differentiate the error significantly.

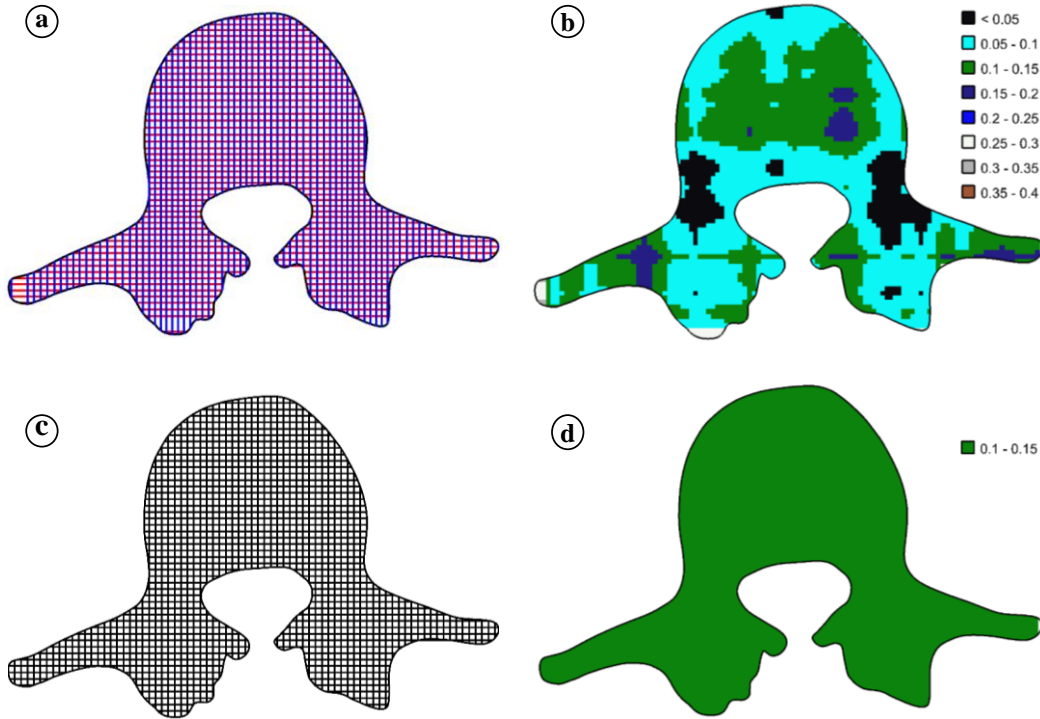


Figure 46. (a) Proposed variational porosity toolpath, (b) corresponding variational porosity distribution map, (c) uniform porosity toolpath, and (d) corresponding uniform porosity map for the first vertebra slice.

Table 11. Comparison between the proposed method and the uniform porosity design.

	Avg. Percentage Error in Porosity	
	Proposed variational design	Uniform porosity design
Vertebra	17.23%	23.41%
Femur	19.32%	22.52%

The generated filament deposition toolpaths are converted into sequential machine movement instructions and sent to the machine to direct print the scaffold. The variational porosity design of the first vertebra slice presented in Figure 46(a) was fabricated with the in-house bio-printer and shown in Figure 47(b-c). Due to the given resolution of the bio-printer as well as material extrusion 3D printer, the toolpath is reconstructed (Figure 47(a)) for larger diameter filament following the same heterogeneous design given in Figure 46(a). The fabricated

bilayer was compared with the design to determine the deviation of the printing process. Ten corresponding cells were randomly selected over both designed and fabricated two-layer scaffold structures at the same locations. The characterization of the fabricated layers was performed using ImageJ software. The cell porosities of the design are calculated using Equation (18). The unit cell comparison of the fabricated model with the designed model is shown in Table 12. The %error in the cell parameters given in Table 12 are the average %error of the ten randomly selected cells. Table 12 indicates that fabricated model is close to the designed one. The % error in the fabricated two layers can be attributed to several factors such as fabrication system, material property, imaging etc.

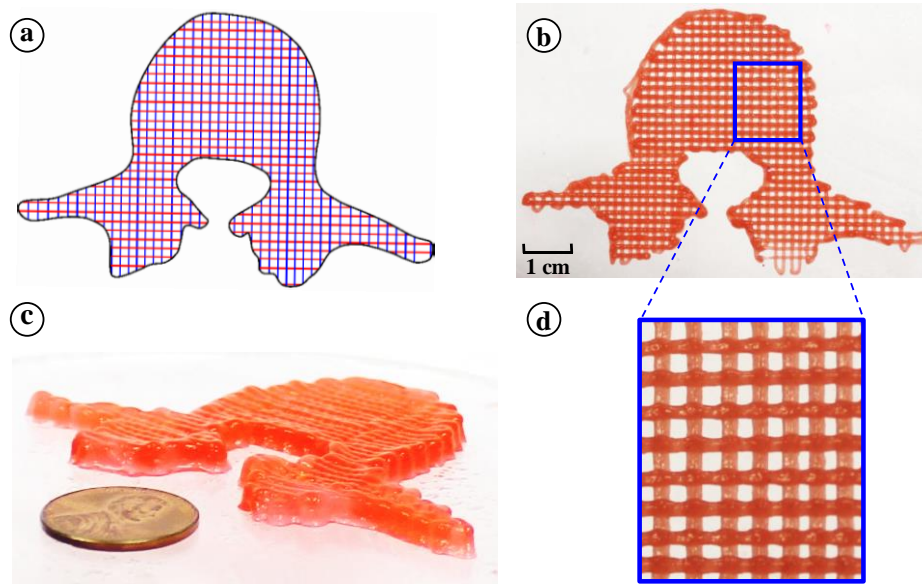


Figure 47. Heterogeneous porosity design from the proposed methodology for the first vertebra slice (a) generated zigzag toolpath, (b) bio-printed with hybrid hydrogel (alginate + cellulose) two layers, and (c) bio-printed 10 layers, (d) enlarged view of a section showing the variational porosity in scaffold topology.

Table 12. Parameter comparison between the fabricated and the designed pore.

	Percentage Error in Fabricated part	
	Vertebra	Femur
Filament Diameter (mm)	7.16%	10.84 %
Cell perimeter (mm)	3.91%	2.43 %
Porosity (%)	2.61%	3.30%

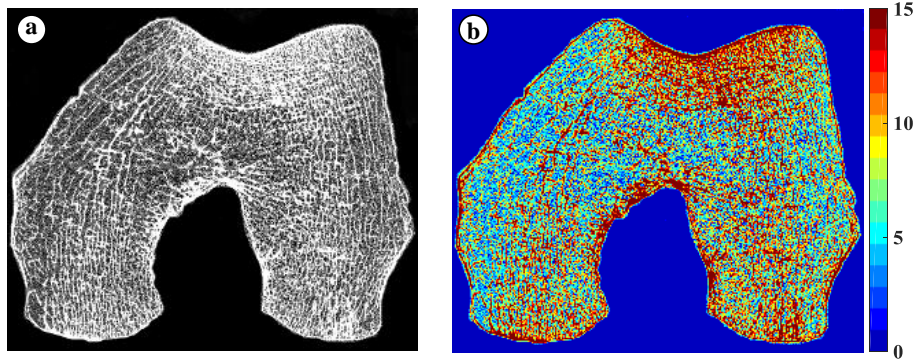


Figure 48. (a) CT image of human distal femur and (b) corresponding quantized image at $l = 16$.

The proposed methodology was also applied on a human distal femur CT image. The heterogeneity information was extracted from the CT image and then Bézier curves were fitted as shown in Figure 49. The unit cell based filament deposition toolpath is shown in Figure 50(a). The designed toolpath is printed with ABS plastic to demonstrate the designed heterogeneity in internal structure (see Figure 50(c)). Table 11 lists the percentage error of porosity between the proposed design and real image as well as the uniform porosity design (70% porosity) and real image of the femur. It can be also seen from Table 2 that the fabricated femur slice closely matches its design.

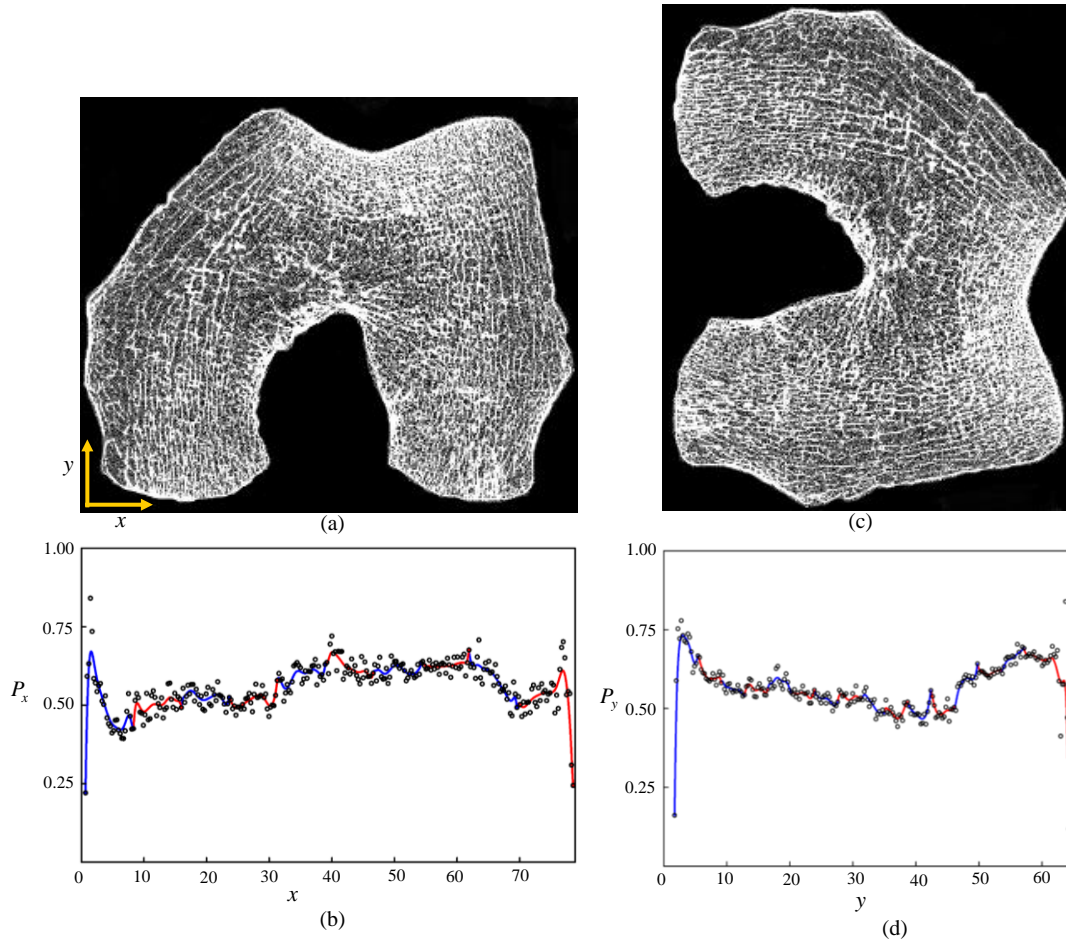


Figure 49. Two corresponding orthogonal parametric topology functions generated from femur CT image (The images and functions are represented in the same scale).

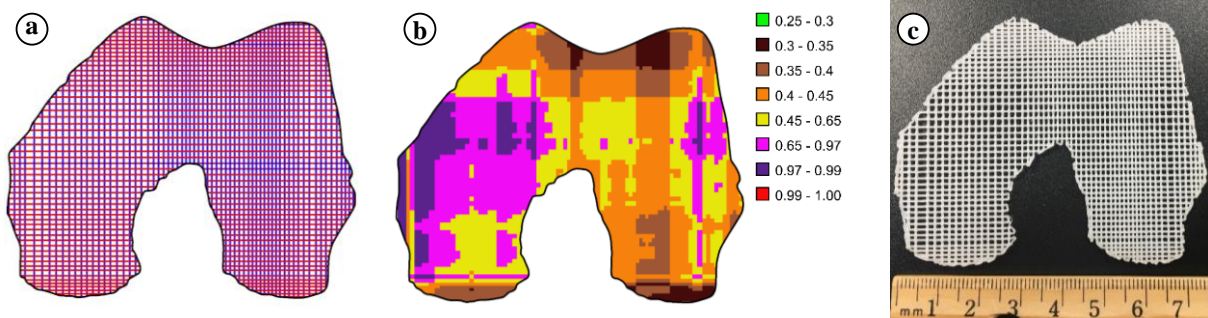


Figure 50. Heterogeneous porosity design from the proposed methodology for femur slice: (a) Zigzag toolpath for femur slice, (b) corresponding variational porosity distribution map, and (c) printed femur slice with ABS material.

The variational porosity design of the femur slice presented in Figure 50(a) was also fabricated with the in-house bio-printer with the hybrid hydrogel and shown in Figure 51(b). Again, due to the given resolution of the bio-printer as well as material extrusion 3D printer, the toolpath is reconstructed (see Figure 51(a)) for larger diameter filament following the actual heterogeneous design. It can be also seen from Table 12 that the fabricated femur slice closely matches its design.

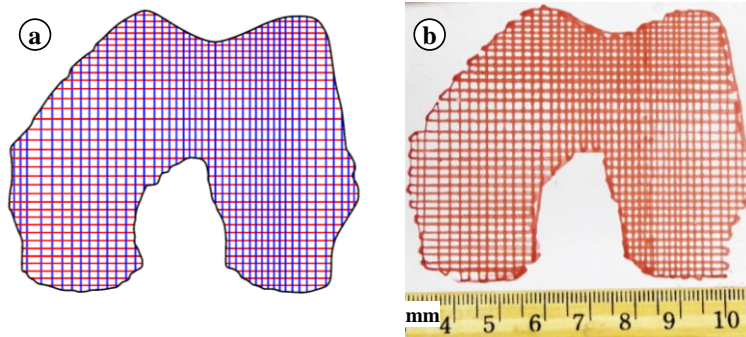


Figure 51. Heterogeneous porosity design and bio-printing for femur slice: (a) generated toolpath and (b) two layers bio-printed with hybrid hydrogel (alginate + cellulose).

Eliminating the disparity between the native tissue architecture and the designed heterogeneous scaffold structure in both design and manufacturing domain is a challenging issue. The designed vertebra and femur structures are showing 17.23% and 19.32% errors when compared with the respective images by randomly selected pores and measured spatial porosity. However, the heterogeneous design proposed here demonstrates a methodological framework to achieve variational porosity which is simple to manufacture. Finally, comparative results between design and manufactured architectures show significant reduction in the deviation error compared to that of the uniform designs.

5.5. Conclusion

In the process of bio-fabrication, the generated tissue scaffolds with boundary representation (B-rep) or surface tessellation (mesh) do not capture the internal architectural information. In biological systems, the internal heterogeneous porosity can vary with tissue type, location, and functionality. The proposed methodology generates a variational porosity distribution map from medical image and digitizes the topology information with the proposed weighted topology reconstruction algorithm. The natural heterogeneity is then captured with parametric functions are used to map the spatial material distribution following voxelization. As a result, manufacturable deposition pattern is constructed with generic platform API which was used for direct bio-printing of heterogeneous tissue/organ scaffolds. This methodology is not restricted to image type (grayscale/color), equipment type, and image intensity. However, testing the robustness of the proposed approach for grayscale and color images of the same target area can be a future work of this research. Moreover, measuring the effectiveness of this topology based scaffold design approach requires *in-vitro* cell culture and viability testing. Considering this fact, the 3D bio-printed heterogeneous structures could be an intriguing subject for future investigation as well.

6. 3D PRINTABLE GRAIN BASED MODEL SEGMENTATION

6.1. Introduction

There are several factors associated with the objects such as part and layer geometry, build height, support material etc. that may demand increased amount of resources in terms of build time and machine hour in 3D printing processes [23, 25]. The increased toolpath discontinuity and change in toolpath directions in the traditional toolpath patterns for porous structures usually require more resources (time, energy, support and model material). The continuity and connectivity based infill design schemes proposed in prior sections can alleviate this resource requirements. However, the existing 3D printing machines often suffer from their limited printing volume when larger thin shell hollowed objects do not fit into the printing envelop of a given printer. The build time for larger objects with higher build height significantly increases due to the increased number of layers. Layer geometries also play a prominent role in the manufacturability of an object. Contour plurality and non-uniform layer geometries [23, 25] resulting from curved free form shaped objects dramatically increase fabrication complexity in additive manufacturing processes. The curved free-form shaped objects sometimes demand sacrificial support material as well depending on the object geometry.

To enhance the functionality and characteristics of 3D printed parts, research on novel structure design methods and techniques has received significant attention over the last few years. For instance, one common approach to reduce the deposition volume and material usage in this bi-modal layers pattern is hollowing the object and creating a scaled-down version inside it [84]. Another hollowing approach to reduce material wastage along with structural stability enhancement is a skin-frame structure design [37] where frame structure is placed underneath the skin. With the same objectives, Lu et al. [33] demonstrated another hollowing technique where

the object interior was filled with voronoi honeycomb structure. However, the hollowing techniques will introduce uncured trapped material inside the object for processes like powder bed fusion, vat polymerization, binder jetting etc. Removing the uncured material from the internal space can be tedious and time consuming and may often time require minor design modification to avoid trapped volume.

Hollowing the curved free form shaped thin wall objects can be done by placing repetitive patterns on the object surface and removing the interior of the patterns. These repetitive cutout patterns on thin wall objects are used for decorative purpose, easy uncured material removal, light weighting, or other functionality such as ventilation/air pass.

The print volume of the existing 3D printing machines is another important factor affecting the printability of larger objects that do not fit into the printing envelop of a given printer. Splitting thin wall objects into discrete segments can solve the problem of limited print area. Also, a careful discretization of curved free-form shaped object into segments may result in uniform layer geometries of the object segments.

Thus, partitioning methodology for 3D printing of objects needs to consider the geometry of the object segments in order to simultaneously reduce the fabrication complexity, support material, and build time. Besides, in case of printing hollow thin wall objects with cutout patterns, support material can be trapped inside the object and hollow patterns and it is often difficult to remove. Therefore, segmentation of both curved and hollow objects and then creating lattice shell segments by cutout patterns would reduce support material and accommodate the intended functionality.

In this Section, a novel grain based mesh-model segmentation approach is proposed which is suitable for both solid and shell objects. Facets on the mesh surface are clustered into

homogeneous groups considering the attributes including facet normal, neighboring facet and locations. The boundary defined by clustered facets is called grain here which is constructed with modified K -mean facet clustering algorithm. The grain geometry is optimized for maximum uniformity in their surface curvature to reduce their fabrication complexity, support volume and fabrication time. A novel grain based mesh-model segmentation approach suitable for solid or shell objects is proposed. Facets on the mesh surface are clustered into homogeneous groups considering the attributes including facet normal, neighboring facet and locations. The boundary defined by clustered facets is called grain here which is constructed with modified K -mean facet clustering algorithm. The grain geometry is optimized for maximum uniformity in their surface curvature to reduce their fabrication complexity, support volume, and fabrication time. Once the grains are generated, they are optimally oriented on the base plane in order to project the hexagonal honeycomb cells on them. Since the grains are already generated based on the maximum uniformity in their surface curvature (flatness), this optimal orientation will ensure the least projection deviation of the honeycomb cells. Removing the interior of the projected honeycomb cells will result in thin shell lattice grains. The thin wall lattice grains are manufactured with the optimal orientations and assembled together with glue. The overall framework of the proposed approach is demonstrated in Figure 52.

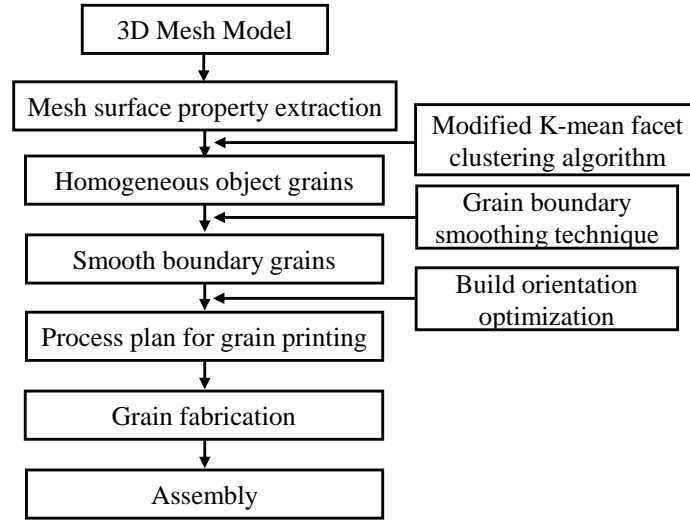


Figure 52. Framework of the proposed methodology.

6.2. Methodology

6.2.1. Surface Property Extraction

The input object model M is represented as a mesh surface consisting of a set of triangular facets $F = \{F_i\}_{i=1,2,\dots,I}$ covering M , where $I = |F|$ is the total number of facets. The triangular facets can be considered as the building unit or patch of the mesh representation of the 3D surface geometry of the model. Each facet F_i on M is uniquely identified with a unit normal vector \mathbf{n}_i and a set of three face vertices $V_i \subset V$ as shown in Figure 53, where V is the set of vertices of the mesh [176].

For the object segmented into a finite set of manifold grains,

$G = \{G_k \subset F \mid G_k \cap G_{k'} = \emptyset\}_{k,k' \in \{1,2,3,\dots,K\} \text{ and } k \neq k'}$, where both k and k' indicate the grain number and $k \neq k'$, each of the facets can be characterized with its location and normal vector. The facet centroid is used to identify the location of the facet and the normal vector is utilized to indicate the surface profile at that location. The centroid c_i of a facet F_i can be calculated from its

vertices such as $c_i = \frac{1}{3}(v_{i1} + v_{i2} + v_{i3})$, where v_{i1}, v_{i2} , and $v_{i3} \in V_i$. The centroids of all facet of the mesh constitute the object facet centroid set $C = \{C_i\}_{i=1,2,\dots,I}$.

Thus, facet characteristics (c_i, \mathbf{n}_i) carry the corresponding surface attributes and cumulatively contribute towards the nature of the object surface for instance, surface concavity, curvature, need of sacrificial supports etc. More precisely, the direction and angle of the facet normal with respect to the build vector determines the surface quality [23] as well as the need of support structure [177]. The dissimilarity in the characteristics of a set of neighboring facets may also lead to incoherent surface regions which could introduce fabrication complexity and increase the amount of support volume. In the following section, homogeneous grain construction technique is discussed, where the object facets are clustered into grains considering the homogeneity with respect to their characteristics.

6.2.2. Point Clustering and Homogeneous Grain Generation

A multi-criterion facet clustering algorithm is proposed to segment the object surface into homogeneous grains such that each surface grain reduces the fabrication complexity and requires the least possible amount of support. If the difference in angles among the normal vectors of the neighboring facets in a grain is smaller, the segmented grain will be flatter requiring lesser amount of support material when build individually. Thus, the goal is to identify the homogeneous flatter regions and discretize them into manifold grains. A modified K -means clustering algorithm was used in order to group the facets belonging to the coherent regions. Two different criteria, the angle between the normal vectors and the centroid-to-centroid distance between the facets are considered to determine the cost function for the K -means clustering algorithm.

In the proposed K -means facet clustering technique, initially a set of the K number of facets $S = \{S_k\}_{k=1,2,\dots,K} \subset F$ with corresponding centroids $SC = \{sc_k\}_{k=1,2,\dots,K} \subset C$ and normals $SN = \{\pi_k\}_{k=1,2,\dots,K}$ are randomly selected as the seeds, which are shown in Figure 53. Each of these K number of seeds will correspond to a cluster. In the facet clustering algorithm, the total number of clusters (also seeds) K is a user defined parameter which will be selected based on the print envelop size, total surface area and geometry of the object, and allowable range of segment size. A non-seed facet set $\{T_j\}_{j=1,2,\dots,I-K} = F \setminus S$ is constructed including the rest of the facets of the mesh. Then, the angle between the normal vector of the non-seed facets $\{T_j\}_{j=1,2,\dots,I-K}$ to the normal vector of each seed facet are determined using Equation (19) as shown in Figure 53 (b).

$$\delta_{j,k} = \cos^{-1}(\mathbf{n}_j \cdot \boldsymbol{\pi}_k); \quad j=1,2,\dots,I-K \text{ and } k=1,2,\dots,K \quad (19)$$

Where, $\delta_{j,k}$ is the angle between the normal vector of j^{th} non-seed facets (T_j) to the normal vector of k^{th} seed facet (S_k). \mathbf{n}_j is the normal vector of the j^{th} facet T_j and $\boldsymbol{\pi}_k$ is the normal vector of the k^{th} seed facet S_k .

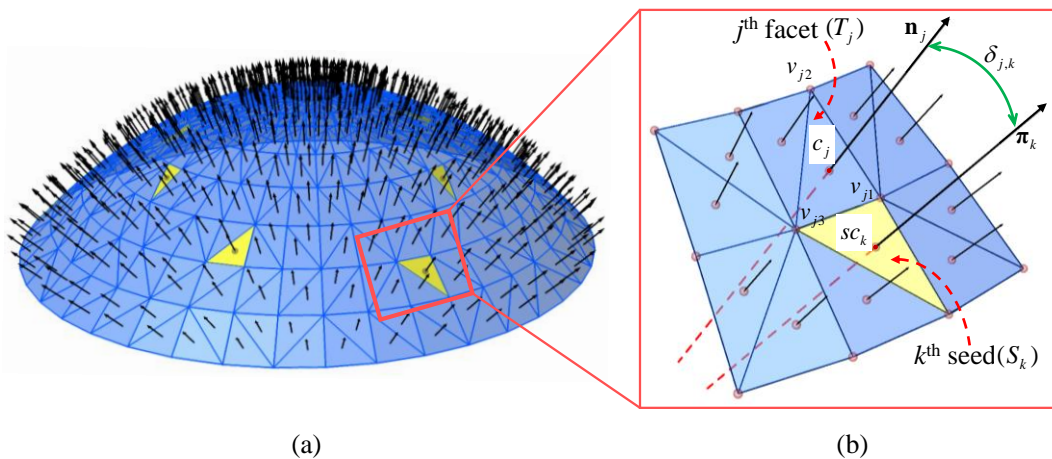


Figure 53. Facet characteristics and relation between seed and non-seed facets. The facets in yellow color are the initial random seeds.

The normalized angle $\delta_{j,k}$ and the distance $d_{j,k}$ between the centroid of the facet T_j and seed facets S_k are used to determine an aggregate cost function value $f_{j,k}$ for each facet j with respect to seed k using Equation (20). The facets are clustered using the weighted cost function value $f_{j,k} \in (0,1)$.

$$f_{j,k} = w_a \times \delta_{j,k}^{norm} + w_d \times d_{j,k}^{norm}; \quad \forall j, k \quad (20)$$

$$\text{where, } \delta_{j,k}^{norm} = \frac{\delta_{j,k} - \min_{k=1,\dots,K} \{\delta_{j,k}\}}{\max_{k=1,\dots,K} \{\delta_{j,k}\} - \min_{k=1,\dots,K} \{\delta_{j,k}\}},$$

$$d_{j,k}^{norm} = \frac{d_{j,k} - \min_{k=1,\dots,K} \{d_{j,k}\}}{\max_{k=1,\dots,K} \{d_{j,k}\} - \min_{k=1,\dots,K} \{d_{j,k}\}}.$$

Here, $f_{j,k}$ is the cost function value of facet T_j with respect to seed k . w_a and w_d are the associated weights for normal vector angle and distance, respectively, and $w_a + w_d = 1$. These two weights represents the relative importance between the two criteria of the cost function. $\delta_{j,k}^{norm}$ and $d_{j,k}^{norm}$ are the normalized with respect to their corresponding extreme values.

Once the cost function values of the facets $\{T_j\}$ are determined, they are clustered into K number of groups by assigning the j^{th} facet to k^{th} cluster when $f_{j,k} = \min_{k=1,\dots,K} \{f_{j,k}\}$. Thus, every facet cluster will eventually forms a grain on the mesh surface resulting in K number of grains $\{G_k\}_{k=1,2,\dots,K}$ as shown in Figure 54(b). However, the constructed grain may have wide range of irregular shapes and sizes as shown in Figure 54(b) and may require homogenization following iterative approach.

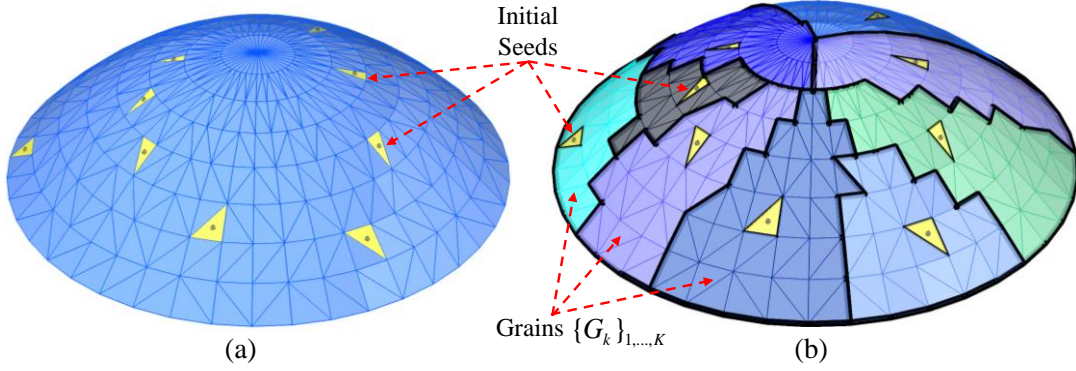


Figure 54. (a) Initial random seeds and (b) generated grains from the initial seeds.

In order to do so, the area centroids $\{g_k\}_{k=1,2,\dots,K}$ of the generated grains in the 1st iteration are determined and corresponding facets will be considered as the new seed facets for next iteration. . If a grain centroid g_k lies on the grain surface, the facet containing the grain centroid will be the updated seed. However, if the grain centroid falls outside of the grain surface as shown in Figure 55(a), a seed updating procedure is performed. In this updating procedure, for each grain, a set of imaginary vectors connecting the centroids of the facets of that particular grain to the centroid of the grain is created. For instance, if a grain G_k consists of a set of facets $\{GF_l^k\}_{l=1,2,\dots,L}$ with corresponding centroids $\{c_l^k\}_{l=1,2,\dots,L}$ and unit normals $\{\mathbf{n}_l^k\}_{l=1,2,\dots,L}$, the set of imaginary vectors $\{\overrightarrow{c_l^k g_k}\}_{l=1,2,\dots,L}$ connecting facet centroids to grain centroid g_k is created as shown in Figure 55(b). Then a set of angles $\{\lambda_l^k\}_{l=1,2,\dots,L}$ for the corresponding grain facets $\{GF_l^k\}_{l=1,2,\dots,L}$ are determined, where λ_l^k is the angle between the normal \mathbf{n}_l^k and imaginary vector

$\overrightarrow{c_l^k g_k}$ of facet GF_l^k (see Figure 55 (b)). λ_l^k can be calculated as $\lambda_l^k = \cos^{-1} \left(\frac{\mathbf{n}_l^k \cdot \overrightarrow{c_l^k g_k}}{\|\mathbf{n}_l^k\| \cdot \|\overrightarrow{c_l^k g_k}\|} \right)$. The

facet corresponding to the minimum angle $\min_{l=1,\dots,L} \{\lambda_l^k\}$ will be used as the new seed for the k^{th} grain

(G_k) as shown in Figure 55(c). Similarly, the seeds for the remaining grains are also updated.

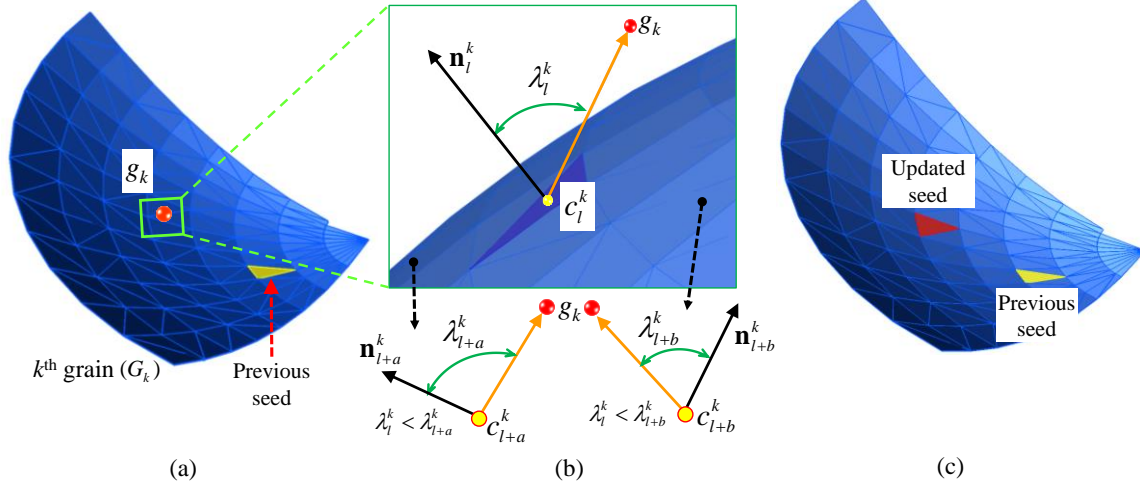


Figure 55. Seed update procedure: (a) k^{th} grain with its centroid g_k , (b) angle determination between the facet normal and imaginary vector connecting the facet centroid to grain centroid, and (c) updated seed.

Using the updated seeds, a set of new grains are formed at the end of the second iteration.

This entire process is repeated until no update happens for the existing seeds. Therefore, the

resulting clusters $\{G_{k=1,2,\dots,K} \subset F\}$ will consist of facets with similar characteristics making

homogeneous grains as shown in Figure 56(f). The clustering and grain formation process are

illustrated in Figure 56.

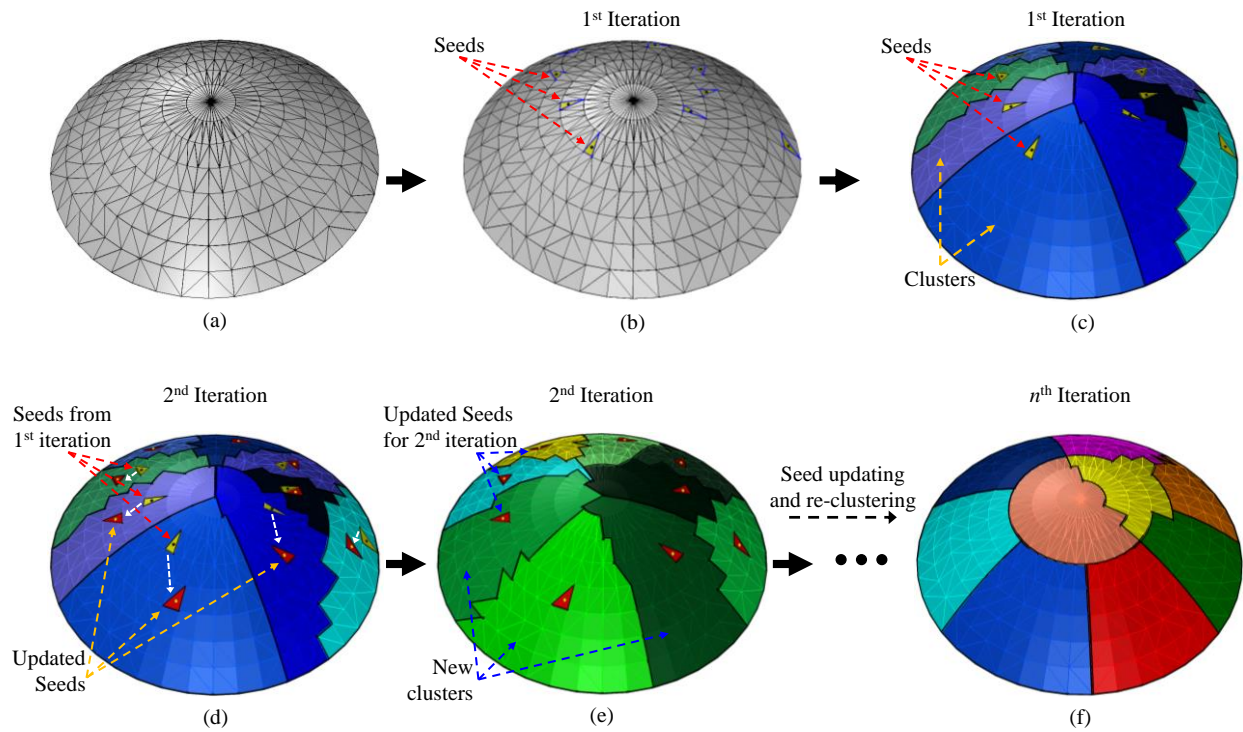


Figure 56. Facet clustering and object grain formation: (a) object mesh surface, (b) initial random seeds, (c) grain formation using the initial seeds, (d) seed updating, (e) grain formation using updated seeds, (f) final grains.

6.2.3. Grain Boundary Smoothing

Once the object surface is segmented into grain according to Section 6.2.2, the boundary curves generated become geometrically jagged because of the nature of the triangular mesh. These jagged edges can undermine the printability and assembly of the grains due to their resolution. It should be noted that this jagged line is an intrinsic property for triangular mesh. Increasing the resolution of the mesh element will make finer jagged line and will not disappear. To resolve this issue a weighted smoothing technique [178] shown in Figure 57 is implemented in this Chapter. The jagged edge has two sides i.e. internal (right hand side) and external (left hand side) with respect to the grain. At first two extreme profile curves need to be calculated by connecting the outer and inner facet edge shown as the blue dashed line. As a result, this will generate a jagged zone between two neighboring grain as shown in Figure 57. The jagged zone

consists of smaller segments which can be defined as internal and external to the grain. The ration of these segments in the jagged zone is considered and a weighted point is inserted on the common facet line segment FL_i . Mathematically the location of this weighted point p_g can be expressed as:

$$p_i = w_i |FL_i| \frac{\overrightarrow{FL_i}}{\|\overrightarrow{FL_i}\|} \quad (21)$$

The weight, w represents the ration $\frac{\text{Area}_{\text{Seg}_i}}{\text{Area}_{\text{Seg}_i} + \text{Area}_{\text{Seg}_{i+1}}}$ shown in Figure 57. By

connecting the weighted points will generate a piecewise linear curve with smooth edge grain boundary as shown in Figure 57. Drawing a smooth boundary with higher degree may create smooth grain boundary but will increases total number of contour points significantly due to approximation and decrease the printability of smooth grain. A large number of points may not be desirable for a continuous path plan. Thus, the proposed area weight based point insertion algorithm not only reduces the number of points, but also generates smooth enough printable grain boundary to ensure ease of manufacturing.

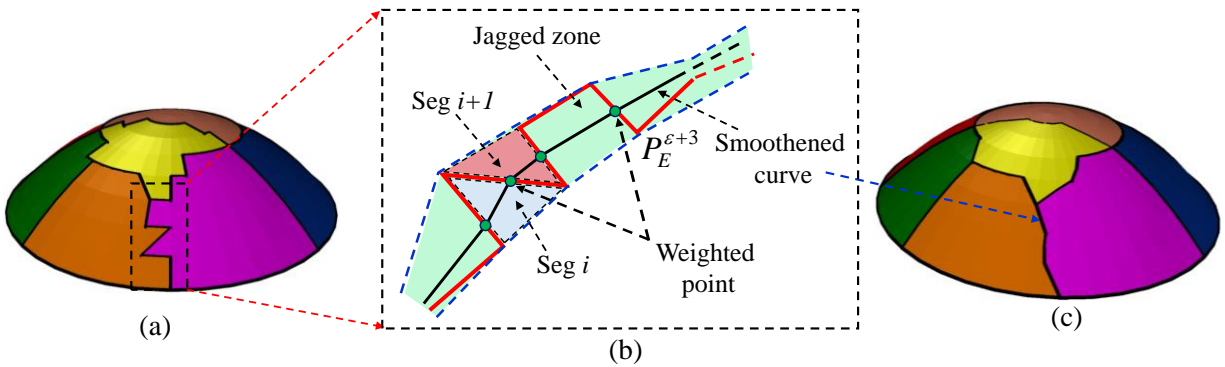


Figure 57. Grain Boundary smoothing process: (a) Grains with jagged boundary curve, (b) smoothing a jagged boundary curve, and (c) grains with smoothed boundary.

6.2.4. Process Plan for Grain Printing

Once the grains on the object surface are refined through boundary smoothing, they are taken away from the object surface and reorient on the build plate for printing. This reorientation of the grains with respect to the global coordinate system of the object is necessary for further minimizing the support volume and build time, and ensuring better surface quality of the printed grains. For instance, Figure 58(a) shows an object segmented into grains in the global coordinate system, where the grain boundaries are already smoothed. One of the grains from the object surface is reoriented on the build plate by rotating it through α and β angles about Z and Y axes, respectively, of the object global coordinate system (see Figure 58(c)). Similarly, all the grains are individually reoriented and then placed together on the build platform for printing. Therefore, the orientation angles α and β for each grain represent the build orientation of that grain. In order to determine the optimal values of α and β for each grain, support volume, surface quality, and build height of the grains are considered. A build orientation determination model is designed to determine the optimum build orientation of the grains.

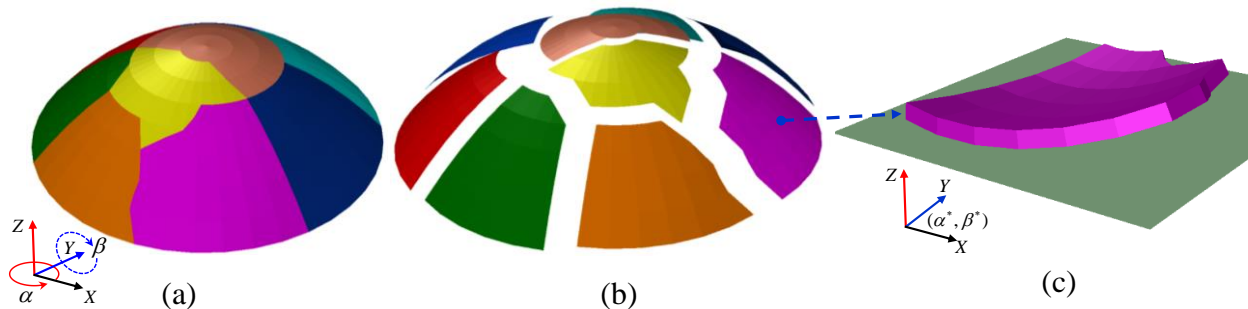


Figure 58. Build orientation for segmented object grains: (a) segmented object and (b) exploded view in the global coordinate system, (c) reorientation of a grain at optimal angles, and (d) all grains optimally oriented and placed on the build plate.

6.2.4.1. Support volume

The support volume (SV) of a 3D printed object is an additional sacrificial structure provided to support the overhang parts of the model. Support volume can be generated by aggregating all the volumes under the facets having normal in downward direction with respect to the build vector as shown in Figure 59. Thus, the angle σ between the unit build vector (\mathbf{b}) and the facet normal (\mathbf{n}) will determine whether the facet requires support or not. σ can be measured as $\sigma = \cos^{-1}(\mathbf{b} \cdot \mathbf{n})$, which is shown in Figure 59(c). A facet on the object mesh will require support if σ is greater than its critical value (σ_c). The critical value σ_c depends on the actual process and material specific requirement. Depending on the process type, it is not always necessary to provide bulk support covering the entire area of the support needed facets. However, bulk support is considered in order to compare results for different printers.

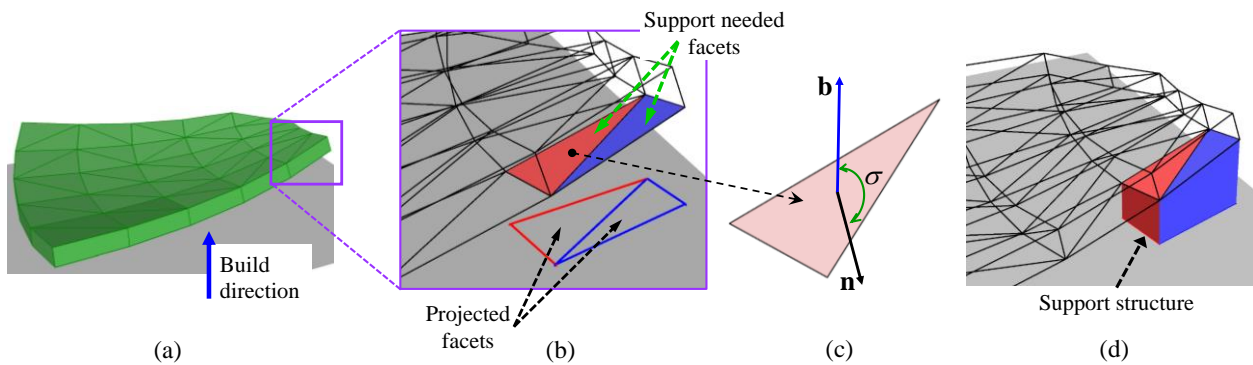


Figure 59. Support needed facets and support generation.

6.2.4.2. Surface quality

Surface quality of a 3D printed part largely depends on its build orientation. Inclined surfaces of the part experience staircase effect between the consecutive layers, which eventually impairs the surface quality. The staircase effect will be the lowest when the normal vectors of all the facets of an object will be parallel and/or perpendicular to the build vector. Thus, in order to

quantify the surface quality with respect to build vector, the angle σ between the build vector (b) and the facet normal (n) shown in Figure 59 is again used. The surface quality Factor SQ_i for i^{th} facet can be measured using Equation (22) [23].

$$SQ_i = \begin{cases} 0, & \text{when } \sigma_i = 0^\circ, 90^\circ, \text{ or } 180^\circ \\ |\tan\sigma_i|, & \text{when } 0^\circ < \sigma_i \leq 45^\circ, \text{ or } 135^\circ < \sigma_i < 180^\circ \\ \frac{1}{|\tan\sigma_i|}, & \text{when } 45^\circ < \sigma_i < 90^\circ, \text{ or } 90^\circ < \sigma_i \leq 135^\circ \end{cases} \quad (22)$$

Build height (BH) can directly affect the build time. Increased build height can inflate the build time due to increased number of layers and resulting tool start-stop. Build height can be reduced by carefully changing the build orientation and hence is taken into account to determine the build orientation. Build height of an object is considered as the height of the object's bounding box along that build direction.

The objective function χ for the build orientation problem given by Equation (23) is formulated as a weighted sum of normalized values of the support volume, surface quality, and build height.

$$\chi(\alpha, \beta) = w_v \cdot \left(\frac{SV}{BV - SV} \right) + w_q \cdot \left(\frac{\sum_{i=1}^I SQ_i \times FA_i}{\sum_{i=1}^I FA_i} \right) + w_h \cdot \left(\frac{BH - GT}{DB - GT} \right) \quad (23)$$

Where FA_i is the area of i^{th} facet. BV , DB , and GT are the grain bounding box volume, largest diagonal length of grain bounding box, and the grain thickness, respectively. w_v , w_q , and w_h represent the relative importance of support, surface quality, and build height; and $w_v + w_q + w_h = 1$. $\chi(\alpha, \beta)$ varies as the grain is rotated about Z and Y axes by angles α and β ,

respectively in a standard 3D coordinate system. Thus, the optimal build orientation for each grain can be determined solving the following minimization problem.

$$\begin{aligned}
 & \text{Min } \{\chi\} \\
 & \text{s.t.} \\
 & \alpha = [\pi/2, 3\pi/2] \\
 & \beta = [0, 2\pi]
 \end{aligned} \tag{24}$$

α and β can be incrementally varied by an interval δ and Equation (24) can be solved to determine the optimal or near optimal build orientation for the object grains.

6.2.5. Shape Conforming Honeycomb Lattice Wall Generation

In order to enhance the functional response as well as to reduce material usage while maintaining better structural stability, each grain of the object surface is tessellated with shape conforming hexagonal honeycomb cells. The segmentation process results in grains with homogeneous functional response. Also the functional response could vary from grain to grain. Therefore, based on the overall desired functional response, grain specific honeycomb cell parameters are chosen. The honeycomb cells are then hollowed by removing the cell interior through Boolean operation with corresponding offset cells. The cell size could, thus, vary from grain to grain yielding variational honeycomb lattice wall across the object.

6.2.5.1. Honeycomb tessellation

Once the optimal orientation of the grains are obtained, the 3D boundary contour BC_k of each orientated grain G'_k is projected on the base plane by setting the z -coordinates of the boundary contour vertices $\{bv = (x, y, z)\}_k$ constant, i.e., $\{bv' = (x, y, z = \text{constant})\}_k$ as shown in Figure 60(a). The planer space bounded by the projected boundary contour BC'_k is tessellated with 2D hexagonal honeycomb cell contours/polygons (see Figure 60(b)). The honeycomb lattice cell contours $\{HC\}_k$ as well as the projected boundary contour BC'_k are offset to inward

direction by an offset distance using the offsetting, and self-intersection and overlap elimination method demonstrated in [179]. The offset distance is selected as the half of the lattice cell side thickness. Finally, all the resulting honeycomb offset contours are mapped back and the 3D honeycomb contours $\{HC'_k\}$ are constructed on the grain surface as shown in Figure 60(c). The interiors of these 3D honeycomb contours are removed from the grain surface resulting in hollowed shape conforming honeycomb lattice grain surface (see Figure 60(d)).

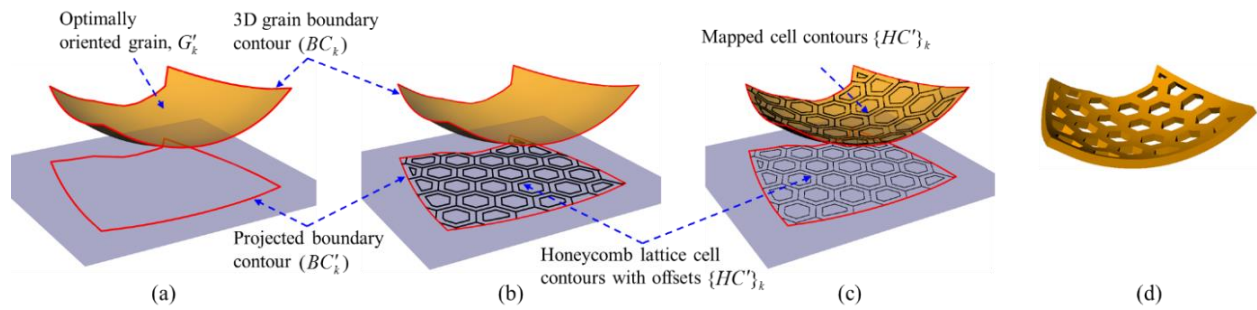


Figure 60. (a) Boundary contour projection of an optimally oriented grain, (b) Hexagonal honeycomb cell tessellation, (c) mapping back honeycomb cells and offsets and constructing 3D cell contours on grain surface, and (d) resulting hollowed shape conforming honeycomb lattice grain.

6.3. Implementation

The proposed methodology is implemented with visual basic based scripting language. The tests are performed on an Intel Core i7 @ 3.4 GHz CPU equipped with 12 GB RAM. The methodology is evaluated on different example objects including flower vase, bison, helmet and hand cast as shown in Figure 61(a), Figure 63(a), Figure 65(a), and Figure 67(a), respectively. The actual objects are scaled down to demonstrate the fabrication and related comparison. Bulk support is generated to estimate the amount of sacrificial support material volume for both full model and segmented model. The raster width used to fabricate the model and support is considered 0.5 mm and 0.75mm respectively for both proposed methodology and commercial support generator. Layer thickness and print speed are considered as 0.254 mm and 30 mm/s

respectively for both model and support. $\vartheta = 5^\circ$ is used to solve Equation (24) in order to determine the orientation angles α and β of the grains.

The resultant grains for flower vase model are generated using the methodology discussed in Section 6.2.2 and 6.2.3 and are shown in Figure 61(b). The represented optimum build orientation for each segment, in Table 13, is determined with the methodology described in Section 6.2.4. Using Dimension 1200es from Stratasys, all the segments are fabricated considering them on the same build plate as shown in Figure 62. This model is also showing significant improvement in term of total build time (BT) i.e. 33%, and support volume (SV) i.e. 38% respectively as shown in Table 15. The total build time and support volume of segmented model are also compared with other commercially available machine software (i.e. Replicator 2, Ultimaker³) which are shown in Table 15.

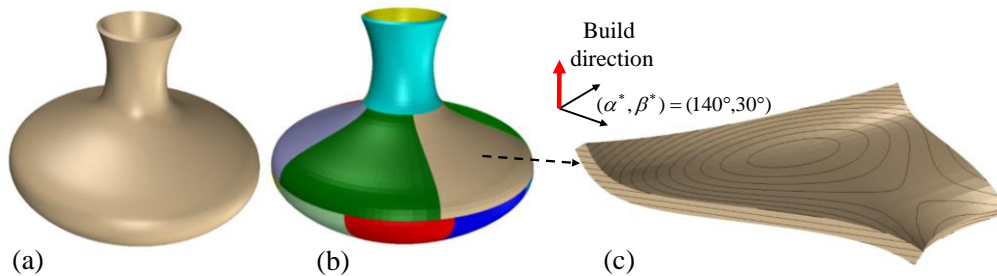


Figure 61. (a) Flower vase model, (b) Segmentation following proposed methodology, (c) Optimally oriented grain with slicing along build direction.

Table 13. Grain wise optimal build orientation for vase model.

Orientation																
α^* (deg.)	180	180	100	180	250	140	210	230	180	100	270	230	190	150	100	0
β^* (deg.)	90	270	150	150	150	30	210	220	40	150	320	320	320	320	320	0

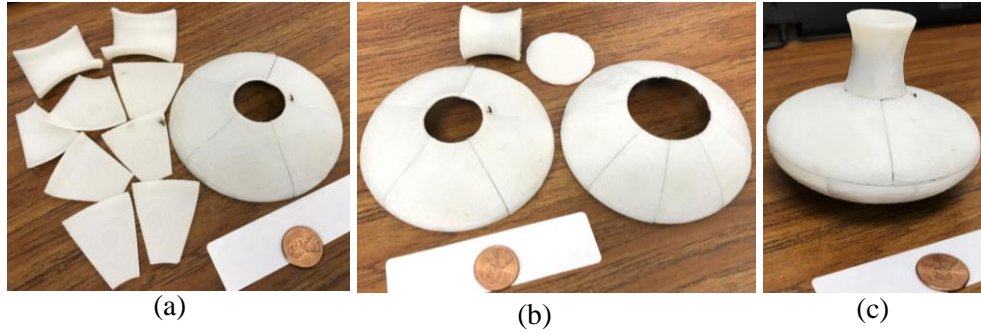


Figure 62. (a-b) Fabricated grains and assembling them together, and (c) final flower vase after assembly.

The grains for bison model are generated using the methodology discussed in Section 6.2.2 and 6.2.3 and are shown in Figure 63(b). The optimum build orientations represented in Table 14 for each grain is determined with the methodology described in Section 6.2.4. To investigate the improvement in term of the total build time and support volume of segmented model, it is again compared with other commercially available machine software (i.e. Dimension 1200es, Replicator 2, Ultimaker³) which are shown in Table 15. Comparative results for build time and support volume of flower vase and Bison models are depicted in Figure 64.

The full-sized (whole) models and the segmented models for two example models have been compared with respect to the total build time and support volume in actual scale with different commercial machines as shown in Table 16. The flower vase and Bison model did not fit in Replicator 2 and Ultimaker³ in actual scale. The objects that fit in different machines show better result for segmented model compared to full model as shown in Table 16.

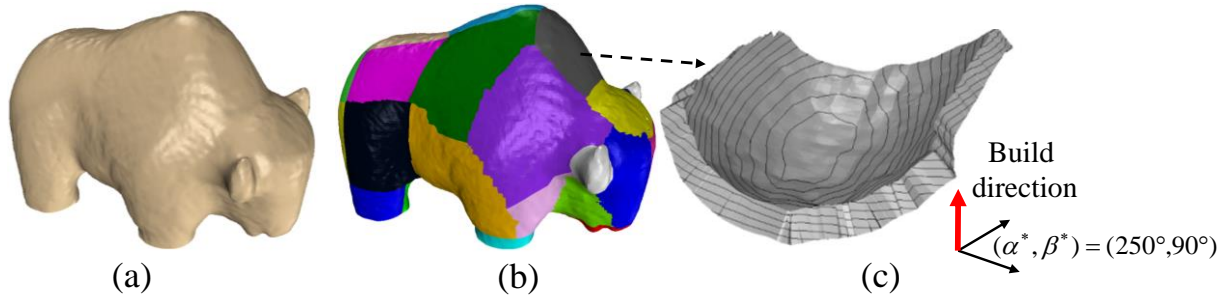


Figure 63. (a) Bison model, (b) Segmentation following proposed methodology, (c) Optimally oriented grain with slicing along build direction.

Table 14. Grain wise optimal build orientation for Bison model.

Orientation														
α^* (deg.)	185	100	240	110	160	100	100	250	110	250	140	180	100	250
β^* (deg.)	110	250	150	250	170	140	120	80	70	90	100	230	270	260
Orientation														
α^* (deg.)	110	140	220	270	0	210	260	120	180	140	230	210	205	255
β^* (deg.)	290	100	110	120	10	20	260	270	10	340	260	110	195	260

Table 15. Comparison between segmented and full models of flower vase and Bison (scaled down version) with respect to total build time and support volume on different commercial machines.

Object	Object volume (mm ³)	Status	Dimension 1200es				Replicator 2				Ultimaker3			
			Build time (min)	% Imp BT	Support volume (mm ³)	% Imp SV	Build time (min)	% Imp BT	Support volume (mm ³)	% Imp SV	Build time (min)	% Imp BT	Support volume (mm ³)	% Imp SV
Flower vase	30316	Full	1193		60468		633		53809		780		37142	
		Segmented	799	33	37379	38	515	19	37490	30	456	41	10203	73
Bison	16190	Full	1022		43097		595		49523		778		46667	
		Segmented	819	20	31299	27	492	17	39025	21	534	31	17142	63

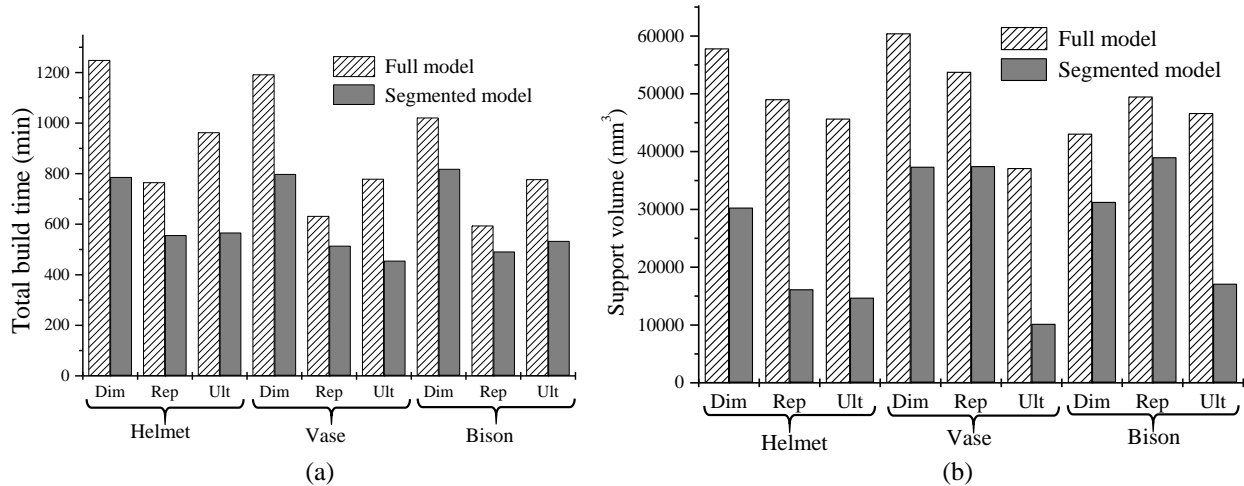


Figure 64. Build time and support volume comparison between full and segmented models on Dimension 1200es (Dim), Replicator 2 (Rep), and Ultimaker³ (Ult).

Table 16. Comparison between segmented and full models of flower vase and Bison (actual scale) with respect to total build time and support volume in different commercial machines.

Object	Object volume (mm ³)	Status	Dimension 1200es				Replicator 2				Ultimaker3			
			Build time (min)	% Imp BT	Support volume (mm ³)	% Imp SV	Build time (min)	% Imp BT	Support volume (mm ³)	% Imp SV	Build time (min)	% Imp BT	Support volume (mm ³)	% Imp SV
Flower vase	360515	Full	2696	34	134843	40	Did not fit	N/A	Did not fit	N/A	Did not fit	N/A	Did not fit	N/A
		Segmented	1786		81253		2059		230165		2160		200125	
Bison	68989	Full	1666	23	69817	29	Did not fit	N/A	Did not fit	N/A	Did not fit	N/A	Did not fit	N/A
		Segmented	1290		50003		1805		53001		1776		38095	

The methodology is also evaluated with two custom example objects: helmet and hand cast as shown in Figure 65(a) and Figure 67(a), respectively. The actual models are scaled down to demonstrate the fabrication and related comparisons with non-segmented (full) models as well. To realize the printability, both example objects segmented into grains with hollowed shape conforming honeycomb lattice wall were printed with ProJet® 660Pro printer using full RGB color.

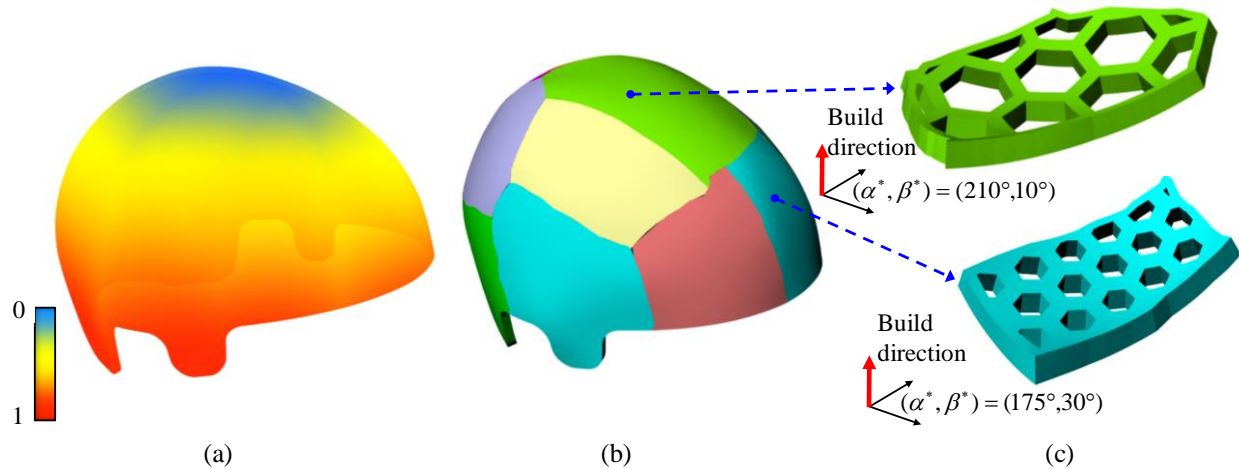


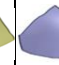
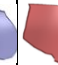
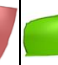

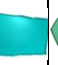
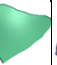
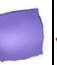



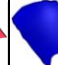




Figure 65. (a) Mesh surface with color map of helmet, (b) segmentation following proposed methodology, (c) two optimally oriented grains with varying honeycomb cutouts.

To generate the 3D geometry of an individually tailored and perfectly fitting helmet, a participant's head was scanned with Artec Eva 3D scanner. After post processing, the resulting mesh surface model can be used for analyzing the functional variation across the 3D model of the helmet. The ventilation requirement and potential impact on the helmet are considered as the functional response and the variation across the model are represented with color map as shown in Figure 65(a). It is assumed that the peripheral region including the front, sides, and back portions of the helmet are more prone to impacts indicating that these areas of the helmet need to be relatively stronger. Thus the top area of the helmet is utilized for more ventilation features. The grains of the helmet are generated using the methodology discussed in Section 6.2.2 and 6.2.3 and are shown in Figure 65 (b). The optimum build orientation of each grain for printability and honeycomb tessellation is determined with the methodology presented in Section 6.2.4 and is listed in Table 17. All the generated grains are tessellated with hexagonal honeycomb cells and the resulting thin wall lattice grains are manufactured with the optimal orientations. Variation from grain to grain is achieved by changing the honeycomb cell size (see Figure 65(c)).

Table 17. Grain wise optimal build orientation for Helmet model.

Orientation															
α^* (deg.)	260	260	140	230	210	175	130	110	220	130	100	250	240	190	170
β^* (deg.)	260	230	120	70	10	30	70	50	260	80	90	100	140	300	80

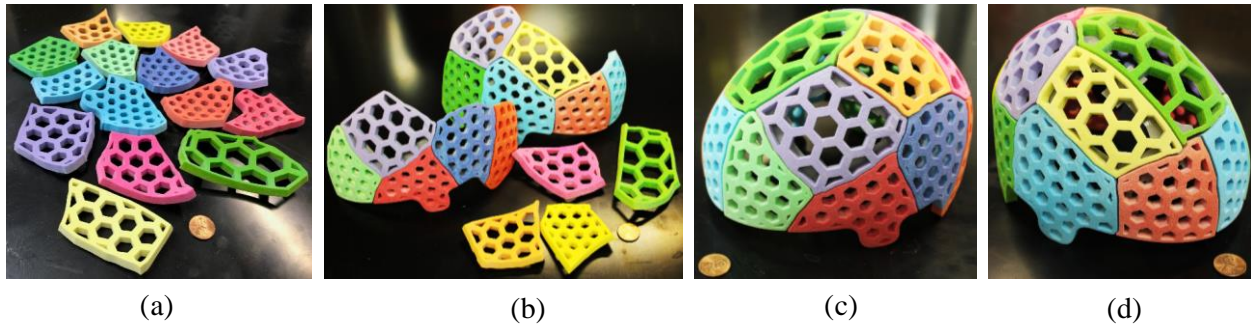


Figure 66. (a) Fabricated grains, (b) Assembling grains together, and (c–d) Final thin lattice wall helmet object after assembly.

All segments are printed on the same build plane and then assembled them together with glue to get the final product as shown in Figure 66. The improvements in total build time (BT), and support volume (SV) are 37% and 66% respectively with respect to full model calculated for Dimension 1200es printer by Stratasys as shown in Table 19. The total build time and support volume of segmented model are compared with Makerbot Replicator 2 and shown in Table 19.

The 3D geometry of a custom 3D hand cast model is also generated by scanning a participant's hand with Artec Eva 3D scanner. Traditional hand casts made from plaster have poor breathability and can easily get wet thereby causing irritation and infection. Additionally, the thermal sensitivity of skin varies from region to region of the body and this demands better ventilation/breathability in the cast for comfort. Therefore, a 3D hand cast model have been recreated with thermal sensitivity distribution map (see Figure 67(a)) given in [180]. The grains of the hand cast shown in Figure 67(b) are generated considering cast geometry and thermal

sensitivity variation The optimum build orientation of each grain for printability and honeycomb tessellation is determined with the methodology presented in Section 6.2.4 and is listed in Table 18. The honeycomb cell size varies among the grains as shown in Figure 67(c) to ensure sufficient ventilation for variational thermal sensitivity.

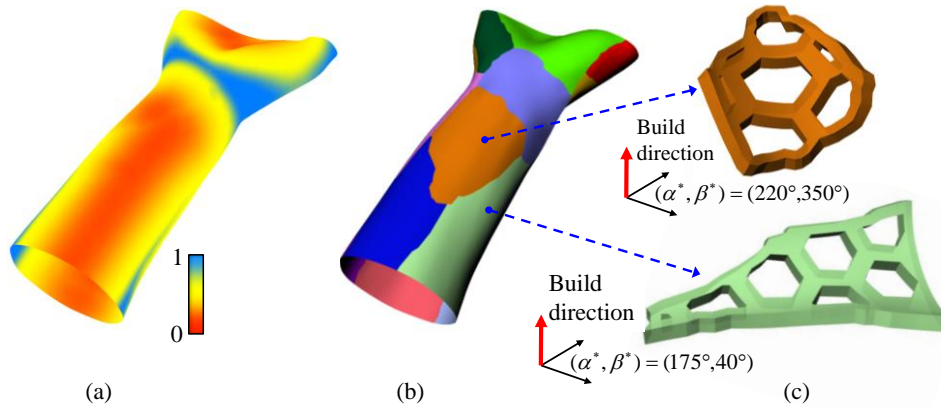


Figure 67. (a) Mesh surface with color map of hand cast, (b) segmentation following proposed methodology, (c) two optimally oriented grains with honeycomb cutouts.

Table 18. Grain wise optimal build orientation for Helmet model.

Orientation																
α^* (deg.)	220	200	185	190	260	180	190	0	210	195	210	110	230	150	190	175
β^* (deg.)	350	325	260	75	190	105	15	0	230	275	125	20	170	55	140	40

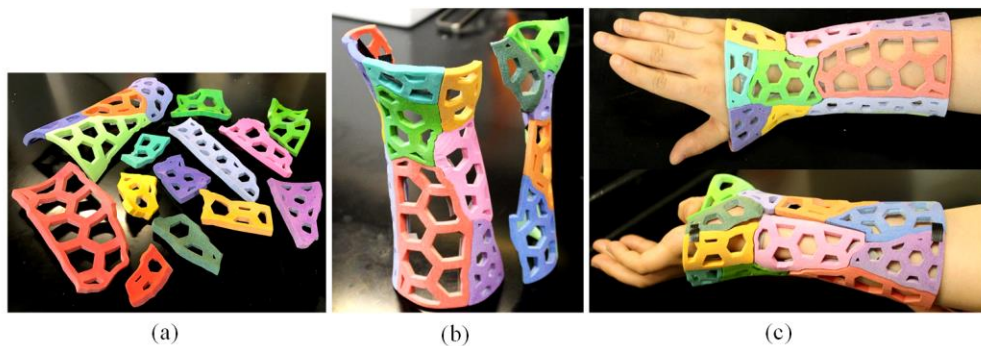


Figure 68. (a) Fabricated grains with some assembled, (b) assembling grains together, and (c) final thin lattice wall hand cast in use for demonstration.

All segments are printed on the same build plane and then assembled them together with glue to get the final product as shown in Figure 68. The improvements in total build time (BT), and support volume (SV) are 39% and 55% respectively with respect to full model calculated for Dimension 1200es printer by Stratasys as shown in Table 19. The total build time and support volume of segmented model are also compared with Makerbot Replicator 2 and shown in Table 19.

Since the minimum/maximum allowable grain size was not considered in the algorithm, the grain size may not necessarily be uniform if the object has areas of high curvature or functional gradient. Relatively smaller grains could be generated in that scenario due to the similarity index defined in Equation (20). This scenario is evident for segmentation of both helmet and hand cast. Also, finer meshing of the object will result in smoother and consistent grains but require more computation resources compared to coarse meshing.

Table 19. Comparison between segmented and full models of helmet and hand cast with respect to total build time (BT) and support volume (SV) on different commercial machines.

Object	Methodology	Object volume (mm ³)	Dimension 1200es				Replicator 2			
			Build time (min)	% Imp BT	Support volume (mm ³)	% Imp SV	Build time (min)	% Imp BT	Support volume (mm ³)	% Imp SV
Helmet	Full solid model	360513	6618		293492		3965		319296	
	Proposed design	229419	4158	37	98650	66	1562	61	79944	75
Hand Cast	Full solid model	170263	3996		171900		1052		56592	
	Proposed design	114709	2420	39	77346	55	793	25	44312	22

6.4. Conclusion

A grain based object segmentation approach for thin wall objects is proposed in this section. The methodology will be particularly suitable for object with larger volume and/or surface area. A similarity index is developed and used for segmenting the part surface. Each segment/grain minimizes the overall fabrication complexity, building time while implicitly

maintaining the functional variation. Implementation of the proposed segmentation process shows that the overall support material and total build time can be significantly reduced. The total build time estimation does not include assembly time and post-processing time such as support removal, finishing etc. Assembly time is largely dependent on the number of grains. During assembly the joining of each segment takes approximately one minute and is considered negligible compared to the total build time. With better assembly and structural stability i.e. systematic grain to grain slot and connector can be used to expedite the assembly process. In this proposed work, the density of lattice architecture stays constant within each grain and varies between grains. Study of graded lattice density will more precisely capture the functional variation which can be a future work. The proposed modular design and manufacturing method will also be suitable for distributed manufacturing or community based manufacturing collaboration for larger parts which will be studied in future.

The variation of the porosity among the grains based on the functional variation requirement may shift the original center of gravity of the object. If the original center of gravity of the object substantially shifts to a different location, it may result in unitability of the object during use. For example, the hand cast with variational ventilation may imbalance its weight distribution around the hand, which may cause additional stress while moving the hand. However, the proposed forms of structures are highly porous and thus light weight. Hence, the variational structural pattern of such structures will not have significant contribution to shifting the center of gravity of the object. Furthermore, for certain applications, such as helmet, the designed porous structures are not the only component of the object, rather such structures are can be used as reinforcement or internal structure. Thus, the overall stability or balancing of object can also be manipulated with other structural/functional components of the object.

7. CONCLUSION AND FUTURE WORK

7.1. Conclusion

This thesis has integrated forms of infill structures and shells in AM parts with the desired part functionality to enhance the usability of additive based manufacturing processes. A design framework is proposed for functionality based manufacturable porous infill structures for additively manufactured parts. The designed honeycomb structures have demonstrated up to 69% more energy absorbing capability along one of the two in-plane directions compared to traditional equivalent honeycomb structure. In addition to that, the proposed porous infill design accommodates smaller cells compared to the traditional regular hexagonal honeycomb infills for the same relative density. Another form of porous honeycomb infill with adaptive density gradient is proposed, where the design approach intends to provide enhanced shell-infill contact interface resulting in improved part surface quality. Compared to a traditional porous infill, the proposed infill has demonstrated 38% material saving to achieve an equivalent surface quality. This approach can be utilized to design and manufacture light weight molds with additive manufacturing technologies where mold surface quality is deemed as a critical functional aspect. In case of biomedical applications of porous structures, one of the important functions of the porous architecture in tissue scaffolds is to facilitate tissue regeneration. This thesis also proposes a medical image based porous scaffold topology design methodology to accurately represent the heterogeneous internal architecture of target tissue/organ. It can be observed that there was only around 3% error between the designed and manufactured structures. Additionally, the design approach introduces a generic hierarchical data storage and transfer platform that seamlessly connects design and manufacturing without the use of a *de facto* STL CAD file.

For thin wall hollowed objects with functional internal cavity, a grain based object segmentation technique is developed to partition the shell of hollowed objects requiring substantially increased resources in terms of large scale machine and build time. Furthermore a shell perforation approach for such objects is introduced to enhance part functionality and avoid material entrapment. Results indicate that the segmentation process itself saved up to 41% build time and 73% support material. The test parts in actual scale even did not fit into few of the 3D printers considered in this study due to their limited print volume. However, the proposed segmentation process made it possible to manufacture the parts with all the 3D printers considered.

Overall, the outcomes of this thesis have signified the effective combination of form and function introduced in additively manufactured part.

7.2. Novelty and Contributions

The Computer-Aided Design and computational design approaches focusing on form of internal architectures of parts have been mostly ignored, or sometimes these approaches are limited to external form of objects only. Hence, these thesis introduces an inversion to the existing situation and focuses on the study of computational design and its application into the forms of functional internal structure as well as external geometry.

The idea of porous structures are not anything newly invented. On the other hand, there are numerous examples of the form of porous structures. However, their adoption to serve the demand for functionality is limited to existing design and manufacturing capabilities. Therefore, this thesis departs from the well-known existing porous structures and their design approaches and demonstrates how the form of porous structures can be adapted to mingle with functionality requirements of the application as well as fabrication constraints.

The three major problems— modelling/design complexity, poor interoperability, and manufacturing limitations result in complex interrelations among form, performance and other functionalities, and manufacturing of parts in additive manufacturing. Such complex interrelations demand a seamless integration among form, functionality, and manufacturing within a single digital platform. However, the off-the-shelf software packages and approaches are not sufficient to establish such platform. In response, the present thesis has overcome the three major problems through the development of custom algorithms, computational methods, and data transfer protocol.

Through implementation and application, this thesis has demonstrated design and direct additive manufacturing of lightweight functional porous and shell objects with minimum amount of support structure. The overall framework integrates design data with manufacturing system enabling a real time digital design and fabrication system.

7.3. Future Works

The design framework proposed in this thesis considers one significant functionality based on the application of a part. Therefore, the design techniques can be further extended in future taking into account multiple functions such as mechanical properties (strength, stiffness/compliance, and energy absorption), physical properties (density variation, light weighting, and pore size) and aesthetics. For biomedical applications, the combination of multiple could be both form (pore morphology/cell geometry) and functionality (porosity variation, strength, and stiffness) to achieve multifunctional scaffolds/implants supporting tissue regeneration, tissue ingrowth and integration, and structural stability. Additionally, structural and biological functionality could be further enhanced with developing and using new materials such composites and nano-fiber reinforcement. This multifunctional design framework coupled with

enhanced materials will result in porous metamaterials which will be an intriguing future research direction of this work.

REFERENCES

1. Ahsan, A.N. and b. Khoda. *Feature Based Continuous Honeycomb Toolpath for Variational Infill in 3D Printing*. in *Proceedings of the 2019 IISE Annual Conference*. 2019. Orlando, FL.
2. Ahsan, A.M.M.N. and B. Khoda, *Honeycomb pattern on thin wall object with grain based 3d printing*. *Procedia Manufacturing*, 2018. **26**: p. 900-911.
3. Ahsan, A.M.M., R.N. Xie, and B. Khoda, *Heterogeneous topology design and voxel-based bio-printing*. *Rapid Prototyping Journal*, 2018. **24**(7): p. 1142-1154.
4. Lee, D.J., et al., *Effect of pore size in bone regeneration using polydopamine-laced hydroxyapatite collagen calcium silicate scaffolds fabricated by 3D mould printing technology*. *Orthodontics & Craniofacial Research*, 2019. **22**: p. 127-133.
5. Li, J.P., et al., *Bone ingrowth in porous titanium implants produced by 3D fiber deposition*. *Biomaterials*, 2007. **28**(18): p. 2810-2820.
6. Davami, K., et al., *Dynamic energy absorption characteristics of additively-manufactured shape-recovering lattice structures*. *Materials Research Express*, 2019. **6**(4).
7. Pelanconi, M., et al., *Thermal design, optimization and additive manufacturing of ceramic regular structures to maximize the radiative heat transfer*. *Materials & Design*, 2019. **163**.
8. Deshmukh, S., H. Ronge, and S. Ramamoorthy, *Design of periodic foam structures for acoustic applications: Concept, parametric study and experimental validation*. *Materials & Design*, 2019. **175**.

9. Chen, W., et al., *Synthesis of filigrees for digital fabrication*. ACM Trans. Graph., 2016. **35**(4): p. 1-13.
10. Schaedler, T.A. and W.B. Carter, *Architected Cellular Materials*. Annual Review of Materials Research, 2016. **46**: p. 187-210.
11. Yi, F., et al., *Strain rate effects on the compressive property and the energy-absorbing capacity of aluminum alloy foams*. Materials Characterization, 2001. **47**(5): p. 417-422.
12. Hague, J.B.-C.a.D.B.a.R.W.a.R., *The design of impact absorbing structures for additive manufacture*. Journal of Physics: Conference Series, 2012. **382**(1): p. 012042.
13. Zhao, C.Y., *Review on thermal transport in high porosity cellular metal foams with open cells*. International Journal of Heat and Mass Transfer, 2012. **55**(13–14): p. 3618-3632.
14. Liebold-Ribeiro, Y. and C. Körner, *Phononic Band Gaps in Periodic Cellular Materials*. Advanced Engineering Materials, 2014. **16**(3): p. 328-334.
15. Egan, P.F., S.J. Ferguson, and K. Shea, *Design of Hierarchical Three-Dimensional Printed Scaffolds Considering Mechanical and Biological Factors for Bone Tissue Engineering*. Journal of Mechanical Design, 2017. **139**(6): p. 061401-061401-9.
16. Wang, X., et al., *Topological design and additive manufacturing of porous metals for bone scaffolds and orthopaedic implants: A review*. Biomaterials, 2016. **83**: p. 127-141.
17. Danilevicius, P., et al., *The effect of porosity on cell ingrowth into accurately defined, laser-made, polylactide-based 3D scaffolds*. Applied Surface Science, 2015. **336**: p. 2-10.
18. Trifale, N.T., E.A. Nauman, and K. Yazawa, *Systematic Generation, Analysis, and Characterization of 3D Micro-architected Metamaterials*. ACS Applied Materials & Interfaces, 2016. **8**(51): p. 35534-35544.

19. Levine, B., *A New Era in Porous Metals: Applications in Orthopaedics*. Advanced Engineering Materials, 2008. **10**(9): p. 788-792.
20. Levine, B.R. and D.W. Fabi, *Porous metals in orthopedic applications - A review*. Materialwissenschaft Und Werkstofftechnik, 2010. **41**(12): p. 1002-1010.
21. Moiduddin, K., et al., *Customized porous implants by additive manufacturing for zygomatic reconstruction*. Biocybernetics and Biomedical Engineering, 2016. **36**(4): p. 719-730.
22. Hollister, S.J., et al., *Engineering craniofacial scaffolds*. Orthodontics & Craniofacial Research, 2005. **8**(3): p. 162-173.
23. Ahsan, A.M.M.N., M.A. Habib, and B. Khoda, *Resource based process planning for additive manufacturing*. Computer-Aided Design, 2015. **69**: p. 112-125.
24. Habib, A., N. Ahsan, and B. Khoda, *Optimizing Material Deposition Direction for Functional Internal Architecture in Additive Manufacturing Processes*. Procedia Manufacturing, 2015. **1**: p. 378-392.
25. Ahsan, N. and B. Khoda, *AM optimization framework for part and process attributes through geometric analysis*. Additive Manufacturing, 2016. **11**: p. 85-96.
26. Domínguez-Rodríguez, G., J.J. Ku-Herrera, and A. Hernández-Pérez, *An assessment of the effect of printing orientation, density, and filler pattern on the compressive performance of 3D printed ABS structures by fuse deposition*. The International Journal of Advanced Manufacturing Technology, 2018. **95**(5): p. 1685-1695.
27. Bartolai, J., et al., *Full Field Strain Measurement of Material Extrusion Additive Manufacturing Parts with Solid and Sparse Infill Geometries*. JOM, 2019. **71**(3): p. 871-879.

28. Ramkumar, P.L., *Investigation on the Effect of Process Parameters on Impact Strength of Fused Deposition Modelling Specimens*. IOP Conference Series: Materials Science and Engineering, 2019. **491**: p. 012026.
29. Moradi, M., S. Meiabadi, and A. Kaplan, *3D Printed Parts with Honeycomb Internal Pattern by Fused Deposition Modelling; Experimental Characterization and Production Optimization*. Metals and Materials International, 2019.
30. Siber, B. *3D Printing Infill – The Basics*. Date accessed: June 03, 2019].
31. Iovenitti, P., S.H. Masood, and M. Nikzad, *In-plane energy absorption evaluation of 3D printed polymeric honeycombs*. Virtual and Physical Prototyping, 2017. **12**(2): p. 117-131.
32. Bates, S.R.G., I.R. Farrow, and R.S. Trask, *Compressive behaviour of 3D printed thermoplastic polyurethane honeycombs with graded densities*. Materials & Design, 2019. **162**: p. 130-142.
33. Lu, L., et al., *Build-to-last: strength to weight 3D printed objects*. ACM Trans. Graph., 2014. **33**(4): p. 1-10.
34. Wu, J., et al., *Self-supporting rhombic infill structures for additive manufacturing*. Computer-Aided Design, 2016. **80**: p. 32-42.
35. Vogiatzis, P., et al., *Computational design and additive manufacturing of periodic conformal metasurfaces by synthesizing topology optimization with conformal mapping*. Computer Methods in Applied Mechanics and Engineering, 2018. **328**: p. 477-497.
36. Prevost, R., et al., *Make it stand: balancing shapes for 3D fabrication*. ACM Trans. Graph., 2013. **32**(4): p. 1-10.

37. Wang, W., et al., *Cost-effective printing of 3D objects with skin-frame structures*. ACM Trans. Graph., 2013. **32**(6): p. 1-10.
38. Wang, D., et al., *Study on the designing rules and processability of porous structure based on selective laser melting (SLM)*. Journal of Materials Processing Technology, 2013. **213**(10): p. 1734-1742.
39. Gibson, L.J. and M.F. Ashby, *Cellular solids: structure and properties*. 1999: Cambridge university press.
40. Bauer, J., et al., *High-strength cellular ceramic composites with 3D microarchitecture*. Proceedings of the National Academy of Sciences, 2014. **111**(7): p. 2453-2458.
41. Valdevit, L., et al., *Optimal active cooling performance of metallic sandwich panels with prismatic cores*. International Journal of Heat and Mass Transfer, 2006. **49**(21): p. 3819-3830.
42. Ajdari, A., H. Nayeb-Hashemi, and A. Vaziri, *Dynamic crushing and energy absorption of regular, irregular and functionally graded cellular structures*. International Journal of Solids and Structures, 2011. **48**(3): p. 506-516.
43. Ahsan, A.N., R. Xie, and B. Khoda, *Direct Bio-printing with Heterogeneous Topology Design*. Procedia Manufacturing, 2017. **10**: p. 945-956.
44. Nakajima, H., *Fabrication, properties and application of porous metals with directional pores*. Progress in Materials Science, 2007. **52**(7): p. 1091-1173.
45. Wadley, H.N.G., *Multifunctional periodic cellular metals*. Philosophical Transactions of the Royal Society a-Mathematical Physical and Engineering Sciences, 2006. **364**(1838): p. 31-68.

46. Cui, L., S. Kiernan, and M.D. Gilchrist, *Designing the energy absorption capacity of functionally graded foam materials*. Materials Science and Engineering a-Structural Materials Properties Microstructure and Processing, 2009. **507**(1-2): p. 215-225.
47. Wadley, H.N., *Multifunctional periodic cellular metals*. Philosophical Transactions of the Royal Society of London A: Mathematical, Physical and Engineering Sciences, 2006. **364**(1838): p. 31-68.
48. Wang, A.-J. and D. McDowell, *In-plane stiffness and yield strength of periodic metal honeycombs*. Journal of engineering materials and technology, 2004. **126**(2): p. 137-156.
49. Bitzer, T.N., *Honeycomb technology: materials, design, manufacturing, applications and testing*. 1997: Springer Science & Business Media.
50. Deshpande, V.S., N.A. Fleck, and M.F. Ashby, *Effective properties of the octet-truss lattice material*. Journal of the Mechanics and Physics of Solids, 2001. **49**(8): p. 1747-1769.
51. Song, J., et al., *Octet-truss cellular materials for improved mechanical properties and specific energy absorption*. Materials & Design, 2019. **173**.
52. Ling, C., et al., *Mechanical behaviour of additively-manufactured polymeric octet-truss lattice structures under quasi-static and dynamic compressive loading*. Materials & Design, 2019. **162**: p. 106-118.
53. Maskery, I., et al., *An investigation into reinforced and functionally graded lattice structures*. Journal of Cellular Plastics, 2017. **53**(2): p. 151-165.
54. Gumruk, R. and R.A.W. Mines, *Compressive behaviour of stainless steel micro-lattice structures*. International Journal of Mechanical Sciences, 2013. **68**: p. 125-139.

55. Smith, M., Z. Guan, and W.J. Cantwell, *Finite element modelling of the compressive response of lattice structures manufactured using the selective laser melting technique*. International Journal of Mechanical Sciences, 2013. **67**: p. 28-41.
56. Li, S.J., et al., *Influence of cell shape on mechanical properties of Ti-6Al-4V meshes fabricated by electron beam melting method*. Acta Biomaterialia, 2014. **10**(10): p. 4537-4547.
57. Campoli, G., et al., *Mechanical properties of open-cell metallic biomaterials manufactured using additive manufacturing*. Materials & Design, 2013. **49**: p. 957-965.
58. Ahmadi, S.M., et al., *Additively Manufactured Open-Cell Porous Biomaterials Made from Six Different Space-Filling Unit Cells: The Mechanical and Morphological Properties*. Materials, 2015. **8**(4): p. 1871-1896.
59. Hammett, C.I. and F.W. Zok, *Compressive Response of Pyramidal Lattices Embedded in Foams*. Journal of Applied Mechanics-Transactions of the Asme, 2014. **81**(1).
60. Panesar, A., et al., *Strategies for functionally graded lattice structures derived using topology optimisation for Additive Manufacturing*. Additive Manufacturing, 2018. **19**: p. 81-94.
61. Bobbert, F.S.L., et al., *Additively manufactured metallic porous biomaterials based on minimal surfaces: A unique combination of topological, mechanical, and mass transport properties*. Acta Biomaterialia, 2017. **53**: p. 572-584.
62. Deshpande, V.S. and N.A. Fleck, *Collapse of truss core sandwich beams in 3-point bending*. International Journal of Solids and Structures, 2001. **38**(36-37): p. 6275-6305.
63. Wallach, J.C. and L.J. Gibson, *Mechanical behavior of a three-dimensional truss material*. International Journal of Solids and Structures, 2001. **38**(40-41): p. 7181-7196.

64. Chiras, S., et al., *The structural performance of near-optimized truss core panels*. International Journal of Solids and Structures, 2002. **39**(15): p. 4093-4115.
65. Wang, J., et al., *On the performance of truss panels with Kagome cores*. International Journal of Solids and Structures, 2003. **40**(25): p. 6981-6988.
66. Sypeck, D.J. and H.N.G. Wadley, *Cellular metals and metal foaming technology*. 2001, MIT-Verlag Bremen.
67. Wadley, H.N.G., N.A. Fleck, and A.G. Evans, *Fabrication and structural performance of periodic cellular metal sandwich structures*. Composites Science and Technology, 2003. **63**(16): p. 2331-2343.
68. Kooistra, G.W. and H.N.G. Wadley, *Lattice truss structures from expanded metal sheet*. Materials & Design, 2007. **28**(2): p. 507-514.
69. Kooistra, G.W., V.S. Deshpande, and H.N.G. Wadley, *Compressive behavior of age hardenable tetrahedral lattice truss structures made from aluminium*. Acta Materialia, 2004. **52**(14): p. 4229-4237.
70. Moongkhamklang, P., V.S. Deshpande, and H.N.G. Wadley, *The compressive and shear response of titanium matrix composite lattice structures*. Acta Materialia, 2010. **58**(8): p. 2822-2835.
71. Queheillalt, D.T. and H.N.G. Wadley, *Cellular metal lattices with hollow trusses*. Acta Materialia, 2005. **53**(2): p. 303-313.
72. Sypeck, D.J. and H.N.G. Wadley, *Multifunctional microtruss laminates: Textile synthesis and properties*. Journal of Materials Research, 2001. **16**(3): p. 890-897.

73. Parthasarathy, J., et al., *Mechanical evaluation of porous titanium (Ti6Al4V) structures with electron beam melting (EBM)*. Journal of the Mechanical Behavior of Biomedical Materials, 2010. **3**(3): p. 249-259.
74. Xiao, L.J., et al., *Mechanical behavior of open-cell rhombic dodecahedron Ti-6Al-4V lattice structure*. Materials Science and Engineering a-Structural Materials Properties Microstructure and Processing, 2015. **640**: p. 375-384.
75. Yan, C.Z., et al., *Evaluations of cellular lattice structures manufactured using selective laser melting*. International Journal of Machine Tools & Manufacture, 2012. **62**: p. 32-38.
76. Leary, M., et al., *Selective laser melting (SLM) of AlSi12Mg lattice structures*. Materials & Design, 2016. **98**: p. 344-357.
77. Wadley, H., et al., *Compressive response of multilayered pyramidal lattices during underwater shock loading*. International Journal of Impact Engineering, 2008. **35**(9): p. 1102-1114.
78. MacDonald, W.D. and T.W. Eagar, *Transient Liquid Phase Bonding*. Annual Review of Materials Science, 1992. **22**(1): p. 23-46.
79. Cook, G.O. and C.D. Sorensen, *Overview of transient liquid phase and partial transient liquid phase bonding*. Journal of Materials Science, 2011. **46**(16): p. 5305-5323.
80. Spears, T.G. and S.A. Gold, *In-process sensing in selective laser melting (SLM) additive manufacturing*. Integrating Materials and Manufacturing Innovation, 2016. **5**.
81. Malekipour, E. and H. El-Mounayri. *Defects, Process Parameters and Signatures for Online Monitoring and Control in Powder-Based Additive Manufacturing*. in *SEM Annual Conference and Exposition on Experimental and Applied Mechanics*. 2017. Indianapolis, IN.

82. Amini, M., S.I. Chang, and P. Rao. *A Cybermanufacturing Framework for Addressing Quality Issues in Laser Powder Bed Fusion (LPBF) Additive Manufacturing Process*. in *Proceedings of the ASME 2019 14th International Manufacturing Science and Engineering Conference (MSEC2019)*. 2019. Erie, PA.
83. Hansen, C.J., et al., *Inkjet Printing: High-Throughput Printing via Microvascular Multinozzle Arrays (Adv. Mater. 1/2013)*. *Advanced Materials*, 2013. **25**(1): p. 2-2.
84. Shapeways. 2017; Available from: <https://www.shapeways.com/tutorials/creating-hollow-objects>.
85. Luo, L., et al., *Chopper: partitioning models into 3D-printable parts*. *ACM Trans. Graph.*, 2012. **31**(6): p. 1-9.
86. Vanek, J., et al., *PackMerger: A 3D Print Volume Optimizer*. *Computer Graphics Forum*, 2014. **33**(6): p. 322-332.
87. Jiang, X.T., et al., *Models partition for 3D printing objects using skeleton*. *Rapid Prototyping Journal*, 2017. **23**(1): p. 54-64.
88. Attene, M., et al. *Mesh Segmentation - A Comparative Study*. in *IEEE International Conference on Shape Modeling and Applications 2006 (SMI'06)*. 2006.
89. Shamir, A., *A survey on Mesh Segmentation Techniques*. *Computer Graphics Forum*, 2008. **27**(6): p. 1539-1556.
90. Chen, X., A. Golovinskiy, and T. Funkhouser, *A benchmark for 3D mesh segmentation*. *ACM Trans. Graph.*, 2009. **28**(3): p. 1-12.
91. Katz, S., G. Leifman, and A. Tal, *Mesh segmentation using feature point and core extraction*. *The Visual Computer*, 2005. **21**(8): p. 649-658.

92. Yao, M., et al., *Level-set-based partitioning and packing optimization of a printable model*. ACM Transactions on Graphics (TOG), 2015. **34**(6): p. 214.
93. Chen, X., et al., *Dapper: decompose-and-pack for 3D printing*. ACM Trans. Graph., 2015. **34**(6): p. 213-1.
94. Hu, R., et al., *Approximate pyramidal shape decomposition*. ACM Trans. Graph., 2014. **33**(6): p. 213-1.
95. Wu, C., et al. *RoboFDM: A robotic system for support-free fabrication using FDM*. in *2017 IEEE International Conference on Robotics and Automation (ICRA)*. 2017.
96. Gao, W., et al., *RevoMaker: Enabling Multi-directional and Functionally-embedded 3D printing using a Rotational Cuboidal Platform*, in *Proceedings of the 28th Annual ACM Symposium on User Interface Software & Technology*. 2015, ACM: Charlotte, NC, USA. p. 437-446.
97. Song, P., et al., *CofiFab: coarse-to-fine fabrication of large 3D objects*. ACM Transactions on Graphics (TOG), 2016. **35**(4): p. 45.
98. Dumas, M., et al., *By-example synthesis of structurally sound patterns*. ACM Trans. Graph., 2015. **34**(4): p. 1-12.
99. Zehnder, J., S. Coros, and B. Thomaszewski, *Designing structurally-sound ornamental curve networks*. ACM Trans. Graph., 2016. **35**(4): p. 1-10.
100. Schumacher, C., B. Thomaszewski, and M. Gross, *Stenciling: Designing Structurally-Sound Surfaces with Decorative Patterns*. Computer Graphics Forum, 2016. **35**(5): p. 101-110.
101. West, A.P., S.P. Sambu, and D.W. Rosen, *A process planning method for improving build performance in stereolithography*. Computer-Aided Design, 2001. **33**(1): p. 65-79.

102. Zhang, Y., et al., *Build orientation optimization for multi-part production in additive manufacturing*. Journal of Intelligent Manufacturing, 2015: p. 1-15.
103. Paul, R. and S. Anand, *Optimization of layered manufacturing process for reducing form errors with minimal support structures*. Journal of Manufacturing Systems, 2015. **36**: p. 231-243.
104. Ancău, M. and C. Caizar, *The computation of Pareto-optimal set in multicriterial optimization of rapid prototyping processes*. Computers & Industrial Engineering, 2010. **58**(4): p. 696-708.
105. Thrimurthulu, K., P.M. Pandey, and N. Venkata Reddy, *Optimum part deposition orientation in fused deposition modeling*. International Journal of Machine Tools and Manufacture, 2004. **44**(6): p. 585-594.
106. Canellidis, V., J. Giannatsis, and V. Dedoussis, *Genetic-algorithm-based multi-objective optimization of the build orientation in stereolithography*. The International Journal of Advanced Manufacturing Technology, 2009. **45**(7-8): p. 714-730.
107. Phatak, A.M. and S.S. Pande, *Optimum part orientation in Rapid Prototyping using genetic algorithm*. Journal of Manufacturing Systems, 2012. **31**(4): p. 395-402.
108. Nikhil, P. and D. Kalyanmoy, *Multi-objective optimisation and multi-criteria decision making in SLS using evolutionary approaches*. Rapid Prototyping Journal, 2011. **17**(6): p. 458-478.
109. Tyagi, S.K., et al., *Optimal part orientation in layered manufacturing using evolutionary stickers-based DNA algorithm*. Virtual and Physical Prototyping, 2007. **2**(1): p. 3-19.
110. Jin, Y.-a., et al., *Optimization of tool-path generation for material extrusion-based additive manufacturing technology*. Additive Manufacturing, 2014. **1-4**: p. 32-47.

111. Ding, D., et al., *A tool-path generation strategy for wire and arc additive manufacturing*. International Journal of Advanced Manufacturing Technology, 2014. **73**(1-4): p. 173-183.
112. Parthasarathy, J., B. Starly, and S. Raman, *A design for the additive manufacture of functionally graded porous structures with tailored mechanical properties for biomedical applications*. Journal of Manufacturing Processes, 2011. **13**(2): p. 160-170.
113. Jin, Y.A., et al., *Additive Manufacturing of Custom Orthoses and Prostheses - A Review*. Cirp 25th Design Conference Innovative Product Creation, 2015. **36**: p. 199-204.
114. Heintl, P., et al., *Cellular Ti-6Al-4V structures with interconnected macro porosity for bone implants fabricated by selective electron beam melting*. Acta Biomaterialia, 2008. **4**(5): p. 1536-1544.
115. Tian, Y., et al., *Osteoblast growth behavior on porous-structure titanium surface*. Applied Surface Science, 2012. **261**: p. 25-30.
116. Bahraminasab, M., et al., *Aseptic loosening of femoral components - Materials engineering and design considerations*. Materials & Design, 2013. **44**: p. 155-163.
117. Bahraminasab, M., et al., *Material tailoring of the femoral component in a total knee replacement to reduce the problem of aseptic loosening*. Materials & Design, 2013. **52**: p. 441-451.
118. Hedia, H.S. and N. Fouda, *Improved Stress Shielding on a Cementless Tibia Tray using Functionally Graded Material*. Materials Testing, 2013. **55**(11-12): p. 845-851.
119. Eldesouky, I., et al., *Femoral Hip Stem with Additively Manufactured Cellular Structures*. 2014 Ieee Conference on Biomedical Engineering and Sciences (Iecbes), 2014: p. 181-186.

120. Izadifar, Z., X. Chen, and W. Kulyk, *Strategic Design and Fabrication of Engineered Scaffolds for Articular Cartilage Repair*. Journal of Functional Biomaterials, 2012. **3**(4): p. 799-838.
121. Tang, D., et al., *Biofabrication of bone tissue: approaches, challenges and translation for bone regeneration*. Biomaterials, 2016. **83**: p. 363-382.
122. Ahsan, A.N., R. Xie, and B. Khoda. *Direct Bio-printing with Heterogeneous Topology Design*. in *45th North American Manufacturing Research Conference (SME NAMRC 45)*. 2017. Los Angeles, CA: to appear in Procedia Manufacturing.
123. Hollister, S.J., R.D. Maddox, and J.M. Taboas, *Optimal design and fabrication of scaffolds to mimic tissue properties and satisfy biological constraints*. Biomaterials, 2002. **23**(20): p. 4095-4103.
124. Murr, L.E., et al., *Microstructure and mechanical properties of open-cellular biomaterials prototypes for total knee replacement implants fabricated by electron beam melting*. Journal of the Mechanical Behavior of Biomedical Materials, 2011. **4**(7): p. 1396-1411.
125. Bartolo, P., et al., *Biomedical production of implants by additive electro-chemical and physical processes*. CIRP Annals - Manufacturing Technology, 2012. **61**(2): p. 635-655.
126. Charles-Harris, M., et al., *A PLA/calcium phosphate degradable composite material for bone tissue engineering: an in vitro study*. Journal of Materials Science: Materials in Medicine, 2008. **19**(4): p. 1503-1513.
127. Mandal, B.B. and S.C. Kundu, *Cell proliferation and migration in silk fibroin 3D scaffolds*. Biomaterials, 2009. **30**(15): p. 2956-2965.

128. Lien, S.-M., L.-Y. Ko, and T.-J. Huang, *Effect of pore size on ECM secretion and cell growth in gelatin scaffold for articular cartilage tissue engineering*. *Acta Biomaterialia*, 2009. **5**(2): p. 670-679.
129. Lam, C.X.F., et al., *Evaluation of polycaprolactone scaffold degradation for 6 months in vitro and in vivo*. *Journal of Biomedical Materials Research Part A*, 2009. **90A**(3): p. 906-919.
130. Ji, C., A. Khademhosseini, and F. Dehghani, *Enhancing cell penetration and proliferation in chitosan hydrogels for tissue engineering applications*. *Biomaterials*, 2011. **32**(36): p. 9719-9729.
131. Sun, Y., et al., *Degradable amorphous scaffolds with enhanced mechanical properties and homogeneous cell distribution produced by a three-dimensional fiber deposition method*. *Journal of Biomedical Materials Research Part A*, 2012. **100A**(10): p. 2739-2749.
132. Zhu, M., et al., *Fabrication of highly interconnected porous silk fibroin scaffolds for potential use as vascular grafts*. *Acta Biomaterialia*, 2014. **10**(5): p. 2014-2023.
133. Borden, M., et al., *Structural and human cellular assessment of a novel microsphere-based tissue engineered scaffold for bone repair*. *Biomaterials*, 2003. **24**(4): p. 597-609.
134. Lin, C.Y., N. Kikuchi, and S.J. Hollister, *A novel method for biomaterial scaffold internal architecture design to match bone elastic properties with desired porosity*. *Journal of Biomechanics*, 2004. **37**(5): p. 623-636.
135. Rainer, A., et al., *Load-Adaptive Scaffold Architecturing: A Bioinspired Approach to the Design of Porous Additively Manufactured Scaffolds with Optimized Mechanical Properties*. *Annals of Biomedical Engineering*, 2012. **40**(4): p. 966-975.

136. Rose, F.R., et al., *In vitro assessment of cell penetration into porous hydroxyapatite scaffolds with a central aligned channel*. *Biomaterials*, 2004. **25**(24): p. 5507-5514.
137. Karageorgiou, V. and D. Kaplan, *Porosity of 3D biomaterial scaffolds and osteogenesis*. *Biomaterials*, 2005. **26**(27): p. 5474-5491.
138. Murphy, C.M., M.G. Haugh, and F.J. O'Brien, *The effect of mean pore size on cell attachment, proliferation and migration in collagen–glycosaminoglycan scaffolds for bone tissue engineering*. *Biomaterials*, 2010. **31**(3): p. 461-466.
139. Klenke, F.M., et al., *Impact of pore size on the vascularization and osseointegration of ceramic bone substitutes in vivo*. *Journal of Biomedical Materials Research Part A*, 2008. **85A**(3): p. 777-786.
140. Gomes, M.E., et al., *Influence of the porosity of starch-based fiber mesh scaffolds on the proliferation and osteogenic differentiation of bone marrow stromal cells cultured in a flow perfusion bioreactor*. *Tissue Engineering*, 2006. **12**(4): p. 801-809.
141. Khoda, A.B. and B. Koc, *Designing Controllable Porosity for Multifunctional Deformable Tissue Scaffolds*. *Journal of Medical Devices*, 2012. **6**(3): p. 031003.
142. Sobral, J.M., et al., *Three-dimensional plotted scaffolds with controlled pore size gradients: Effect of scaffold geometry on mechanical performance and cell seeding efficiency*. *Acta Biomaterialia*, 2011. **7**(3): p. 1009-1018.
143. Khoda, A.K.M.B., I.T. Ozbolat, and B. Koc, *Engineered Tissue Scaffolds With Variational Porous Architecture*. *Journal of Biomechanical Engineering*, 2011. **133**(1): p. 011001.
144. Lopa, S. and H. Madry, *Bioinspired Scaffolds for Osteochondral Regeneration*. *Tissue Engineering Part A*, 2014. **20**(15-16): p. 2052-2076.

145. Bettinger, C.J., et al., *Three-Dimensional Microfluidic Tissue-Engineering Scaffolds Using a Flexible Biodegradable Polymer*. *Advanced Materials*, 2006. **18**(2): p. 165-169.
146. Khoda, A., I.T. Ozbolat, and B. Koc, *A functionally gradient variational porosity architecture for hollowed scaffolds fabrication*. *Biofabrication*, 2011. **3**(3): p. 1-15.
147. Maria, C.D., et al., *Development of a novel micro-ablation system to realise micrometric and well-defined hydrogel structures for tissue engineering applications*. *Rapid Prototyping Journal*, 2014. **20**(6): p. 490-498.
148. Chua, C.K., et al., *Development of a tissue engineering scaffold structure library for rapid prototyping. Part 1: Investigation and classification*. *International Journal of Advanced Manufacturing Technology*, 2003. **21**(4): p. 291-301.
149. Chua, C.K., et al., *Development of a tissue engineering scaffold structure library for rapid prototyping. Part 2: Parametric library and assembly program*. *International Journal of Advanced Manufacturing Technology*, 2003. **21**(4): p. 302-312.
150. Naing, M.W., et al., *Fabrication of customised scaffolds using computer-aided design and rapid prototyping techniques*. *Rapid Prototyping Journal*, 2005. **11**(4): p. 249-259.
151. Bucklen, B.S., et al., *Bone-derived CAD library for assembly of scaffolds in computer-aided tissue engineering*. *Virtual and Physical Prototyping*, 2008. **3**(1): p. 13-23.
152. Salmi, M., et al., *Patient-specific reconstruction with 3D modeling and DMLS additive manufacturing*. *Rapid Prototyping Journal*, 2012. **18**(3): p. 209-214.
153. Fantini, M., et al., *Additive manufacturing to assist prosthetically guided bone regeneration of atrophic maxillary arches*. *Rapid Prototyping Journal*, 2015. **21**(6): p. 705-715.

154. Giannitelli, S.M., et al., *Current trends in the design of scaffolds for computer-aided tissue engineering*. Acta Biomaterialia, 2014. **10**(2): p. 580-594.
155. Challis, V.J., et al., *Prototypes for Bone Implant Scaffolds Designed via Topology Optimization and Manufactured by Solid Freeform Fabrication*. Advanced Engineering Materials, 2010. **12**(11): p. 1106-1110.
156. Dias, M.R., et al., *Optimization of scaffold design for bone tissue engineering: A computational and experimental study*. Medical Engineering & Physics, 2014. **36**(4): p. 448-457.
157. Yoo, D.-J., *Computer-aided porous scaffold design for tissue engineering using triply periodic minimal surfaces*. International Journal of Precision Engineering and Manufacturing, 2011. **12**(1): p. 61-71.
158. Yoo, D.-J., *New paradigms in cellular material design and fabrication*. International Journal of Precision Engineering and Manufacturing, 2015. **16**(12): p. 2577-2589.
159. Xu, Z., Q. Wang, and J. Li, *Modeling porous structures with fractal rough topography based on triply periodic minimal surface for additive manufacturing*. Rapid Prototyping Journal, 2017. **23**(2): p. 257-272.
160. Es-Said, O.S., et al., *Effect of Layer Orientation on Mechanical Properties of Rapid Prototyped Samples*. Materials and Manufacturing Processes, 2000. **15**(1): p. 107-122.
161. Domingos, M., et al., *Evaluation of in vitro degradation of PCL scaffolds fabricated via BioExtrusion – Part 2: Influence of pore size and geometry*. Virtual and Physical Prototyping, 2011. **6**(3): p. 157-165.
162. Khoda, A.K.M.B. and B. Koc, *Functionally heterogeneous porous scaffold design for tissue engineering*. Computer-Aided Design, 2013. **45**(11): p. 1276-1293.

163. Ranellucci, A. *Slic3R*. 11/17/2018]; Available from: <https://slic3r.org/>.
164. *Repetier-Host*. Available from: <https://www.repetier.com/>.
165. Papka, S.D. and S. Kyriakides, *In-plane compressive response and crushing of honeycomb*. Journal of the Mechanics and Physics of Solids, 1994. **42**(10): p. 1499-1532.
166. Khetan, S. and J.A. Burdick, *Patterning hydrogels in three dimensions towards controlling cellular interactions*. Soft Matter, 2011. **7**(3): p. 830-838.
167. Khoda, A.K.M., I.T. Ozbolat, and B. Koc, *Designing heterogeneous porous tissue scaffolds for additive manufacturing processes*. Computer-Aided Design, 2013. **45**(12): p. 1507-1523.
168. Hazrati Marangalou, J., K. Ito, and B. van Rietbergen, *A new approach to determine the accuracy of morphology–elasticity relationships in continuum FE analyses of human proximal femur*. Journal of Biomechanics, 2012. **45**(16): p. 2884-2892.
169. Hazrati Marangalou, J., et al., *A novel approach to estimate trabecular bone anisotropy using a database approach*. Journal of Biomechanics, 2013. **46**(14): p. 2356-2362.
170. Hazrati Marangalou, J., et al., *Locally measured microstructural parameters are better associated with vertebral strength than whole bone density*. Osteoporosis International, 2014. **25**(4): p. 1285-1296.
171. Hazrati Marangalou, J., et al., *Inter-individual variability of bone density and morphology distribution in the proximal femur and T12 vertebra*. Bone, 2014. **60**: p. 213-220.
172. Krug, R., et al., *High-Resolution Imaging Techniques for the Assessment of Osteoporosis*. Radiologic Clinics of North America, 2010. **48**(3): p. 601-621.
173. Piegl, L. and W. Tiller, *THE NURBS BOOK*. 2nd ed. 1997: Springer-Verlag Berlin Heidelberg. 646.

174. Habib, M.A. and B. Khoda, *Attribute driven process architecture for additive manufacturing*. Robotics and Computer-Integrated Manufacturing, 2017. **44**: p. 253-265.
175. Laboratory, M.-C. *XtremeCT II of human distal femur*. 04/30/2017]; Available from: <https://www.ucalgary.ca/microct/equipment>.
176. Khoda, B., *Computer-Aided Design of Additive Manufacturing Components*. Laser-Based Additive Manufacturing of Metal Parts: Modeling, Optimization, and Control of Mechanical Properties, 2017.
177. Habib, M.A. and B. Khoda, *Support grain architecture design for additive manufacturing*. Journal of Manufacturing Processes, 2017. **29**: p. 332-342.
178. Khoda, A.K.M., T.O. Ibrahim, and K. Bahattin, *A functionally gradient variational porosity architecture for hollowed scaffolds fabrication*. Biofabrication, 2011. **3**(3): p. 034106.
179. Khoda, A.K.M.B., I.T. Ozbolat, and B. Koc, *Engineered Tissue Scaffolds With Variational Porous Architecture*. Journal of Biomechanical Engineering, 2010. **133**(1): p. 011001-011001-12.
180. Zhang, X., et al., *Thermal-Comfort Design of Personalized Casts*, in *Proceedings of the 30th Annual ACM Symposium on User Interface Software and Technology*. 2017, ACM: Québec City, QC, Canada. p. 243-254.